Pore changes in an illitic clay during one-dimensional compression

Yanhao Zheng, Béatrice Baudet, Pierre Delage, Jean-Michel Pereira, Peter Sammonds

Pore changes in an illitic clay during one-dimensional compression

Zheng, Y., Baudet, B.A., Delage, P., Pereira, J-M., Sammonds, P.

Abstract

The pore size, shape and orientation of an illite-dominant clay were mapped during one-dimensional compression, using mercury intrusion porosimetry, scanning electron microscopy and gas adsorption. The total porosity was found to spread over the three IUPAC classes of pores sizes: micropores (below 2 nm), mesopores (2-50 nm) and macropores (above 50 nm), and all three pore classes were observed during the compression. The clay structure is aggregated, with visible inter-aggregate pores (about 80% of the total porosity), the remaining intra-aggregate pores of size approximately equal to the thickness of illite platelets (50-100 layers). During compression the largest pores first collapsed, followed by a progressive collapse, in an orderly manner, of smaller and smaller pores. MIP data suggest that the macroscopic deformation mainly translates at the pore scale into changes of inter-aggregate porosity, while intra-aggregate pores spread over the micro- to mesopore size range. Gas adsorption tests show that the volume of intra-aggregate pores decreases with loading, probably due to rearrangement of particles composing the aggregates, while the specific surface area reduces. Examination of the pores' orientation on both vertical and horizontal planes confirms a preferential orientation of pores normal to the loading direction, with a gradual flattening of the pores.

Keywords: clays, fabric/structure of soils, microscopy, compressibility

1. Introduction

The distribution of pore sizes and the microfabric in clay have been studied since the early 1970s, providing insights into the mechanisms underlying clay behaviour such as the soil-water retention curve or one-dimensional consolidation. Clays of various origins and mineralogy were tested, including Gulf of Guinea clay (Hattab et al., 2013; Delage and Tessier, 2020), sensitive clays (Diamond 1970; Delage and Lefebvre, 1984; Delage, 2010), kaolin (Diamond, 1970; Penumadu and Dean, 2000; Hattab and Fleureau, 2010; Yu et al., 2016; Chow et al., 2019; Gao et al., 2020), montmorillonite or bentonite (Diamond 1970, Griffiths and Joshi, 1989, Tessier, 1991, Hicher et al., 2000; Lubelli et al., 2013; Delage and Tessier, 2020), Fithian illite (Diamond, 1970), mixtures of kaolinite and montmorillonite (Griffiths and Joshi, 1989; Hattab et al., 2015), and reconstituted natural clays of mixed mineralogy (e.g. Pusan by Ninjgarav et al., 2007, London clay by Monroy et al., 2010; Lucera clay by Cotecchia et al., 2014, or Maryland clay by Burton et al., 2015).

For many clays, scanning electron micrographs show an aggregated microstructure, and early mercury intrusion porosimetry tests performed on compacted clays highlighted a double structural level, after which Barden and Sides (1970) introduced the concept of inter-aggregate pores and intra-aggregate pores. This bimodal pore size distribution (PSD) usually found in unsaturated compacted clays becomes unimodal if the samples are saturated (e.g. Li and Zhang, 2009). On the other hand, the PSDs of remoulded or reconstituted clays are typically unimodal (Hattab et al., 2015; Yu et al., 2016; Chow et al., 2019; Gao et al., 2020).

Delage and Lefebvre (1984) described the compression of sensitive clays from Canada at the pore scale, which are mainly composed of illite and have a rigid porous matrix made up of large pores, as predominantly due to the large inter-aggregate pores collapsing in an orderly manner under load. The porous matrix of montmorillonite on the other hand is much more deformable, with various microstructure levels involved during compression (Griffiths and

Joshi, 1989; Tessier, 1991). Monroy et al. (2010) more recently classified the microstructure of compacted London clay as composed of inter-aggregate pores, corresponding to the large voids between soil aggregates, and intra-aggregate pores, corresponding to the small voids between the individual particles within the aggregates. As the two types of pores are not easily observed or quantified, this definition retains a degree of subjectivity and is subject to interpretation. An assumption often made is that the range of small pore sizes over which the MIP curves for different stress levels of 1D compression may coincide represents the intra-aggregate pores, which may deform when subjected to large stresses. This assumption implies that macroscopic volume changes observed during loading are only due to the collapse of inter-aggregate pores while intra-aggregate pores are not affected (Delage and Lefebvre, 1984; Ninjgarav et al., 2007; Wang and Xu, 2007; Yu et al., 2016; Chow et al., 2019; Delage and Tessier, 2020). Small pore sizes require higher mercury pressures to be intruded, but generally the mercury pressure used for MIP has an upper limit of 210 MPa, therefore some intra-aggregate pores, below 5 nm, cannot be detected. Higher pressures might also disturb the soil microstructure. Non-invasive techniques such as gas adsorption would allow additional information on these very small pore sizes.

The MIP technique has been combined with SEM imaging to complement data on porosity and pore size with the soil microfabric (Delage and Lefebvre, 1984, Delage et al., 2006; Wang and Xu, 2007; Zeng et al., 2017). Often, the evolution of the clay microfabric with loading tends to be tracked through the shape and orientation of clay particles, which have been observed to change during one-dimensional compression (e.g. Cotecchia and Chandler, 1998), constant stress path tests (e.g. Cotecchia et al., 2014) and triaxial compression (e.g. Hattab and Fleureau, 2010), with findings such as particles aligning perpendicular to the loading direction when subjected to 1D compression (e.g. Hattab and Fleureau, 2010; Cotecchia et al., 2014). The morphology and orientation of pores on the other hand have been investigated much less,

using image analysis methods based on SEM photos, impregnated samples or, more rarely, micro-CT scans. This was initially carried out in the field of soil science, where mapping the evolution of the pores with loading is not so much a concern (e.g. Pires et al., 2008) but with also some recent examples in soil mechanics (e.g. Cetin and Söylemez, 2004; Gao et al., 2020). The low resolution of SEM images however is often a limit to quantify small pore sizes reliably. The two techniques of MIP and SEM, when applied to porosity, are also not directly comparable as their mechanisms and the assumptions made to interpret their data are different. The study by Gao et al. (2020), one of the few to have combined MIP and SEM data to examine changes in porosity during loading, shows the evolution of the micropore structure of kaolinite during triaxial compression using MIP and SEM data, however because only SEM images from a vertical plane were taken the 3D pore shape and orientation had to be inferred from stereology. It would be possible to draw a more complete picture of the pore size, shape and orientation by taking sub-samples from a tested specimen for SEM images on both vertical and horizontal planes, for 3D representations of the pore distribution and shape, complemented by MIP measurements for pore entry sizes.

In spite of the limitations of reliability in the small pore size range or of data combining MIP and SEM data, the list of studies so far available, some listed above, gives preliminary insights into the micropore structure of clays. Data are either for kaolinite, montmorillonite, or kaolinite/montmorillonite mixture, minerals easily available commercially, or natural clays of mixed mineralogy. Illite is less researched because of the difficulty in sourcing it, although it is present in many natural clays. Because of its 2:1 cationic layered silicate structure similar to that of montmorillonite, but with potassium cations ensuring the stability of particles, the micro-scale behaviour of illite is likely to be different and data on its microporosity would contribute to establishing a microscale behavioural framework. In this paper, the evolution of pore size, shape and orientation of an illite-dominant clay is presented, using MIP

measurements and SEM imaging on vertical and horizontal planes, complemented by gas adsorption data for the smaller pores, taken at selected stages of a one-dimensional compression test. As well as making available data for a mineralogy less widely investigated, the main aim of the study was to provide a complete and rigorous set of data on the evolution of the clay pores while addressing a) the accuracy of the initial void ratio, as different samples were tested to simulate different states on the normal compression line, by controlling rigorously the reconstituted sample preparation and the void ratio; b) the subjectivity of the terms "inter-" and "intra-aggregate porosity" by superposing an objective scale based on pore size; c) the lack of porosimetry data at the nanoscale, by providing data from gas adsorption tests; d) the lack of information about the shape of the pores, particularly in previous work on illitic clays, by mapping the evolution of pore shapes in the vertical and horizontal planes on samples taken from the same freeze-dried specimens used for the MIP tests.

2. Testing materials

The clay investigated was prepared from a clayey loess from Jingyang, South Loess Plateau of China, found at 50 m below ground level. Detailed geotechnical properties of the parent clayey loess were presented by Xu and Coop (2016), while a mineralogy analysis showed that it contains about 35% clay minerals, with a majority of illite (Zuo, 2019). The tested clay was obtained by separating the fines fraction of the illite-rich parent clayey loess from the coarser particles by sedimentation, so the soil has lost its initial structure and is no longer collapsible. The mineralogy and chemical compositions of the retrieved fines fraction were determined by X-ray diffraction (XRD) and X-ray fluorescence (XRF), showing that 66.7% are clay minerals, with 48.2% illite, 8.6% independent montmorillonite, 5.5% kaolinite, 4.4% chlorite and no detected illite-montmorillonite mixed layers. About half of the remaining 34.3% non-clay minerals are calcite (16.5%), others being quartz (10.4%), albite (5.2%) and biotite (1.1%). The

tested illite-dominant soil will therefore hereafter be referred to as illitic clay. The chemical composition of the illitic clay obtained from the XRF measurements shows a majority of silicon dioxide and aluminium oxide, followed by sodium and magnesium oxides (**Table 1**). **Table 2** shows the basic physical properties of the illitic clay. The liquid limit was measured using the cone penetrometer method and the plastic limit was determined by the standardized thread-rolling method in accordance with BS1377: Part 2: 1990. The 55.4% liquid limit and 35.4% plasticity index indicate a clay of high plasticity according to the British Soil Classification System (BSCS), also suggesting high compressibility. The grain size distribution (**Fig.1**), characterized using a mass-based BT-9300LD laser diffraction particle size analyser (dry method), shows that about 50% of the particles are silt size, with a median diameter D_{50} of about 2 μm. This high silt content, which contrasts from the previous results of 66.7% clay minerals may be due to aggregation of the clay particles. There was no visible silt particle in the SEM either, while the high plasticity index reveals a large proportion of plastic particles, most probably clay too.

3. Testing programme and methods

3.1 One-dimensional compression tests

The tests were carried out in standard oedometer tests (50 mm diameter by 20 mm height, saturated porous stones and filter paper at the top and base) following BS 1377: Part 5:1990. The specimens were prepared in slurry state by mixing the clay thoroughly with deionized water at a water content of 1.25 times the liquid limit (Burland, 1990), before being poured carefully into the ring to avoid trapping air bubbles. The loading stages were 5, 10, 25, 50, 100, 200, 400, 1000, and 2000 kPa, depending on the targeted stress level. Each loading stage lasted for at least 24 hours until the tested samples had reached the end of primary consolidation, estimated from the deformation-square root time curve.

Examining the microstructure at the vertical effective stresses of 100, 400, 1000 and 2000 kPa required conducting four oedometer tests separately, taking special care to ensure that the four specimens started from the same void ratio and followed an identical compression curve. In practice, the tests were repeated until an acceptable accuracy was reached in the initial void ratios. After reaching equilibrium at the desired loading stage, as much water as possible in the oedometer cell i.e. water bath, porous disks and ducts was removed, then the specimen was unloaded as quickly as possible. This method, also followed by Rocchi & Coop (2014), ensured undrained unloading conditions, restraining swelling thanks to the build-up of an internal suction (Skempton and Sowa, 1963). The soil specimen was then removed from the cell quickly, to avoid absorption of the water from the porous discs, and the excess water attached to the soil sample was wiped off before measurement. The consolidated samples were wrapped in cling film and wax, then stored in a highly humid environmental chamber for the micro-analysis tests (**Table 3**).

Calculation of the initial specific volume

The precise control of the initial specific volume (v_i) and the accuracy of calculating the initial specific volume are critical to ensure that the specimens loaded to different maximum consolidation pressures followed the same compression path, from the same void ratio in the $e - \log\ \sigma_v'$ plot. This will determine whether the results from the micro-analyses on the different samples can be used to represent the evolution of the porosity during one-dimensional compression. Three methods proposed by Rocchi and Coop (2014) to determine an initial specific volume as accurate as possible were used (Eq. (1)-(3)):

(1) $v_i = \frac{\gamma_w(1+w_i)G_s}{\gamma_i}$

(2) $v_i = \frac{\gamma_w(1+w_f)G_s}{\gamma_f(1-\varepsilon_{vol})}$

(3) $v_i = \frac{\gamma_w G_s}{\gamma_{di}}$

where G_s is the specific gravity of the soil; γ_w is the unit weight of the water; γ_{di} is the initial dry unit weight of the soil; γ_i and γ_f are the initial and final bulk unit weights; w_i and w_f are the initial and final water contents; and ε_{vol} is the overall volumetric strain for the test.

Although the specimens were vacuumed after mixing, the calculated initial degrees of saturation of the slurries were typically around 97%. Equations (1) and (2) can be used regardless of the soil sample's saturation (Rocchi and Coop, 2014), while equation (3) is based on the assumption of full saturation at the end of the test, which, with the immersion of the specimens in the water bath, was found sufficient to give good final saturation during the tests. Each of the three methods is based on different, independent measurements and is very sensitive to these measurements, so extra caution was taken with the measurements. For each oedometer test, the value of v_i was calculated by the three methods and the average of the three values was taken for analysis. The maximum discrepancy between any individual value and the chosen values was ± 0.02, which is a reasonable mean error for the reconstituted clay (Shipton and Coop, 2012).

3.2 Dehydration of the specimens

To minimize the disturbance of the microstructure during dehydration, the investigations were carried out on freeze-dried specimens (Gillott 1969, Diamond, 1970; Tovey and Wong 1973), a technique now largely adopted (e.g. Delage and Lefebvre, 1984; Monroy et al. 2010; Yu et al. 2016). To do so, small soil sticks (around 10 mm × 3 mm × 3 mm) were carefully trimmed by means of a thin steel wire prior to being frozen ultra-quickly in liquid nitrogen that was

previously cooled down to its freezing point (- 210 °C) by applying vacuum (Delage et al. 2006). The advantage of this approach is that it helps get rid of the boiling bubbles that would appear when directly plunging specimens in liquid nitrogen at boiling temperature (- 195 °C), which would also reduce the freezing speed. Under ultra-quick freezing conditions, crypto-crystalline ice, with no expansion upon freezing, is obtained (Delage and Pellerin, 1984). Once frozen, the specimens were immediately put into the vacuum chamber of a freeze-dryer, operating more than 24 hours for complete sublimation of the water.

3.3 Pore structure characterization

Results from the MIP tests are represented by pore size distribution (PSD, cumulative and density function) curves in a semi-logarithmic plot, shown in terms of void ratio (intruded mercury void ratio, e_m). The void ratio is obtained by directly multiplying the intruded pore volume (in cm^3/g of soil) by the particle density of the illitic clay (2.73 g/cm^3) determined by small pycnometer method using 50 mL density bottles with stopper following BS1377: Part 2: 1990. SEM observations are used to characterize the pore morphology. It was decided to follow the International Union of Pure and Applied Chemistry (IUPAC) recommendations for the classification of pores (Sing, 1985), which allow for an objective description based on size: micropores are pores of size below 2 nm; mesopores have sizes between 2-50 nm, and macropores have sizes greater than 50 nm. The theories underlying the MIP and SEM analyses are briefly explained below.

MIP tests

The MIP measurements were carried out using a Micromeritics AutoPore IV 9500 Automated Mercury Porosimeter. The freeze-dried samples were first injected with mercury at low pressures (3.6-200 kPa), then transferred to a high-pressure system with a working pressure

from 0.2 to 227.5 MPa. The common interpretation of MIP data to link mercury pressure to pore size is via Washburn's equation (1921) (Eq. (4)). This is an assumption which works for the range of sizes accessible by MIP technique. Washburn's equation, from which the radius of entry of the pores can be calculated from the applied pressure, was derived based on the assumption that pores have a right cylinder geometry with a constant radius. Such an assumption is necessary as most porous media contain pores of irregular and widely-varying shape, and has been widely adopted for a range of soils (e.g. Delage & Lefevre, 1984; Griffiths & Joshi, 1989). The mercury intrusion pressure P_{Hg} is related to the entrance pore diameter D according to the Laplace-Young capillary law:

(4) $P_{Hg} = -\frac{4\sigma \cos\theta}{D}$

where σ is the interfacial mercury–solid tension; θ is the contact mercury-solid angle. Following Diamond (1970), who measured the contact angle of clays of different mineralogy, values for the tested illitic clay were chosen as $\sigma = 0.484$ N/m at 25 °C and $\theta = 147°$. The pore diameters that can be measured in the MIP tests range from 0.005 to 350 μm.

SEM tests and image processing

The photographs of the microstructure were obtained using a JEOL JSM- 6480LV scanning electron microscope with a high resolution of 3.0 nm. Prior to SEM imaging, the freeze-dried soil specimens were coated with gold to improve the conductivity of their surface. For each tested specimen, two frozen-cut cross-sections that served as horizontal (perpendicular to the loading direction) and vertical (parallel to the loading direction) observation planes were created by fracturing the freeze-dried cubic sticks from the centre of the soil cylinder (Delage et al., 1982; Delage and Lefebvre, 1984). Micrographs of the slurry were also made. The SEM micrographs of fractured freeze-dried specimens present the advantage of allowing to observe a well-defined fracture controlled by the breaking of ice, that goes through all microstructure

levels, as if ice acted as an impregnation resin. This is not the case in fractures made in wet clay samples observed in Environmental SEM (ESEM), which may be influenced by some weaker areas in the clay specimen and also result in some displacement of clay particles.

The SEM pictures were processed and analysed using the Image-Pro Plus software (Media Cybernetics, Silver Spring, Maryland). The threshold grey value of pore segmentation, ranging from 0 to 255 for 8-bits images, is a key parameter when the porosity is estimated based on the fractional 2D area of the image (Moyano et al., 2012). In this work, the cumulative histogram of the intensity of the grey-scale image computed by the software was used for selecting the most appropriate threshold value of pore segmentation based on the overflow criterion method (Wong et al., 2006). **Figure 2** gives a specific example of determining the threshold value (of 69) for a photomicrograph of the vertical plane of the clay at 100 kPa. In order to validate the threshold value used for the segmentation of the SEM images, the size of visible pores on the micrographs was also measured manually by ruler and the pore size distributions obtained by segmentation and by manual measurement compared. From SEM images (**Fig.3a**), the pores were segmented using this threshold value with the clay minerals showing as grey parts and the red parts representing the pores(**Fig.3b**), then the geometries of all the pores were outlined (**Fig.3c**), and ellipses were selected to fit the clear boundaries of the pores by keeping the same area and orientation (same moments of inertia of order 1 and 2) (**Fig.3d**). The elliptical shape is a widely adopted choice in the literature (e.g. Moyano et al., 2012; Gao et al., 2020), which also fits with the idea of cylindrical pores assumed in the MIP calculations. The pore orientation was computed from the angle (θ) between the major axis of the pore and the vertical axis (**Fig.4a**) ranging from 0° (vertical upward) to 180° (vertical downward) clockwise. The aspect ratio of the pore was taken as the ratio between the major axis and minor axis of the ellipse representative of this pore (**Fig.4b**), where the minimum value of 1 represents a perfectly regular geometry, e.g. a circle. The orientation and aspect ratio of pores from different

observation locations on a given plane of the same sample, i.e. either the vertical plane or the horizontal plane, were found to be consistent, which indicates the homogeneity of the specimen and the reliability of the software, and also validates the choice of the representative observed locations.

In addition to the MIP and SEM tests, nitrogen adsorption tests were carried out using a Micromeritics Automatic Micropore Physisorption Analyzer 2020 HD88, to quantify the specific surface of the clay as well as the volume of pores below 5 nm. The specific surface area was determined by inverting the experimental N_2 adsorption-desorption isotherm at different relative pressures (P/P_0) based on the Brunauer, Emmett and Teller (BET) theory (Brunauer et al. 1938; Kuila, 2013), where P is the absolute equilibrium pressure and P_0 is the condensation pressure of nitrogen in laboratory conditions.

4. Results and discussions

The oedometer compression and swelling curves obtained from the four tests with the best void ratio accuracy are shown in **figure 5**, where the red points indicate the states selected for pore structure analysis. The compression index, C_c, was calculated as equal to 0.394 and the swelling index, C_s, to 0.067. The unloading curve is typical of a non-swelling soil, with a C_s/C_c ratio of 0.17.

4.1 Pore structure of the slurry clay

The specific surface area of the clay was found to be 57.66 m²/g, a value comparable with literature data (Mitchell and Soga, 2005). The nitrogen gas adsorption-desorption isotherm of the slurry clay shown in **figure 6** is characterised by a hysteresis loop, associated with condensation occurring in the mesopores, and the limiting uptake over a range of high relative pressures P/P_0, indicative of micropores (Sing, 1985). The sudden drop in adsorbed amount

observed on the desorption branch around a relative pressure of 0.5 may be due to cavitation of the nitrogen (Maruyama et al., 2018). The shape of the hysteresis loop, which does not show any limiting adsorption at high relative pressure, is usually found in plate-like particles, giving rise to slit pores (Sing, 1985). The high adsorption at low relative pressure confirms the presence of macropores. Pores are thus present in the three ranges of pore sizes defined by the IUPAC i.e. micropores (below 2 nm), mesopores (between 2 and 50 nm) and macropores (above 50 nm).

The microstructure of the slurry clay is shown in **figure 7**. Thanks to the freeze-dry breaking technique, one can observe a nice typical loose open microstructure characterized by large pores with sizes around 1-2 μm, together with clearly visible well crystallized platelets. The structural units observed are either rather small aggregated platelets (with an average size between 0.1 and 0.7 μm, two of them are highlighted in red), or much larger ones, as wide as 2 μm (also highlighted in red) or even more, with 100 nm thickness (highlighted), and on which small platelets are stuck. This thickness corresponds to a number of around 100 layers per platelet, given that the inter-basal spacing of illite minerals is 0.96 nm. Small platelets are around 50 nm thick, corresponding to around 50 layers. Overall, the microstructure can be considered as an aggregated microstructure, in which some aggregates are made up of small platelets, and others composed of large and thick platelets on which very small ones are stuck. There is no particular orientation observed in the large platelets, resulting in an isotropic aspect, compatible with the nature of the observed slurry.

The initial global void ratio, e_0, of the oedometer specimen obtained by mass-volume relations (Eq. (1)-(3)) is 1.97 while the intruded mercury void ratio, e_m = 1.92 (with a corresponding cumulative intrusion pore volume of 0.703 cm^3/g), is slightly lower. Whereas the intruded void ratios were found to match the global void ratios in all of the illite-rich Champlain clays investigated by Delage (2010), values of intruded void ratios significantly

smaller than global void ratios have been observed in montmorillonite-dominant bentonite specimens (Delage et al., 2006). Here it is thus hypothesized that the 8.6% montmorillonite content contributes to this difference.

The PSDs of the slurry clay obtained by MIP are shown in **figure 8**. While the cumulative curve (**Fig.8a**) is composed of mercury intrusion and extrusion curves, only the cumulative mercury intrusion curves were used for analysing the pore volume and size distribution of the clay. The cumulative PSD can be divided into three stages: a first stage, for entrance pore diameters ranging from 345 µm down to about 5.5 µm, represents approximately 10% of the total pore volume. As suggested by Delage and Lefebvre (1984) and Penumadu and Dean (2000), this section of the curve corresponds to a slight isotropic compression of the dehydrated specimen prior to any mercury intrusion and is linked to the deformability of the microstructure of the dehydrated slurry, although the good final appearance of the sample after the end of the test, with no collapse, indicates that the structure resisted to this first compression stage. It must also be noted that higher mercury pressures no longer apply along the external surface of the sample, since they are compensated by the mercury already intruded. This is particularly true here, with a large amount of mercury intruded through a reasonably small mercury pressure increase, as shown by the slope of the curve. The second stage, for entrance pore diameters smaller than 5.5 µm, is characterized by a nearly straight line that defines a well sorted pore population typical of a well sorted inter-aggregate porosity comparable to that obtained by Delage and Lefebvre (1984). Observing the shape of the density function (**Fig. 8b**) suggests that the lower boundary of this inter-aggregate porosity is around 0.6 µm, corresponding to approximately 80% of the total intruded pore volume. The last stage, for entrance pore diameters from 0.6 µm down to about 0.005 µm, represents approximately 20% of the total intruded pore volume, with a moderately sorted pore population corresponding to intra-aggregate pores, presenting a bump with a top at 0.14 µm.

The pore size density function curve in **figure 8b** is characterized by an overwhelmingly dominant pore domain with a single peak around 2-3 μm in diameter, that nicely corresponds with the large inter-aggregate pores observed in the SEM. Note that this correspondence has seldom been observed in both natural and remoulded clays, in which bottle neck effects are most often detected, with access pore diameters smaller than the real ones (see for instance Delage and Lefebvre, 1984). This trend is to be linked to the high void ratio (1.97) and the very open microstructure of the slurry.

The intra-aggregate porosity may be related to the average platelet thickness, about 0.1 μm from SEM observation (**Fig.7**), a value comparable to that detected by Delage and Lefebvre (1984) on Champlain sensitive illitic clays, which retained dual porosity during remoulding. Based on the brick model, in which the average intra-aggregate entrance diameter provides an estimation of the average thickness of the platelets (see for instance Menaceur et al., 2016), the 0.14 μm entrance pore diameter at the top of the bump in **figure 8b** is compatible with the SEM estimation of the platelet thickness. Some intra-aggregate pores below the minimum diameter of 5 nm, too small to be intruded by mercury, may also exist, mainly due to the inter-layer spaces of the hydrated montmorillonite minerals, that correspond to around 10% of the material. Due to the saturated state of the slurry, the montmorillonite layers would probably be either in a 4W hydration state at zero suction, i.e. with 4 layers of water adsorbed on their surface, and an inter-basal spacing of 2.16 nm (Saiyouri et al., 2004) of, perhaps only in a 3W state (Tessier, 1990). The total pore volume of intra-aggregate pores of size below 5 nm was determined from the N_2 adsorption test data (e.g. Rouquerol et al., 1998; Kuila, 2013). A value of 0.0176 cm^3/g was found, corresponding to a void ratio of 0.048 (**Table 4**).

4.2 Evolution of the pore size distribution during one-dimensional compression

The nitrogen gas adsorption-desorption isotherms of the clay carried out at the various consolidation pressures were found to have exactly the same shape as the isotherm at the initial state of the slurry (**Fig. 6**) and they almost matched, indicating that three populations of pores (micropores, mesopores and macropores) remain even as the effective pressure increases, at least up to 2,000 kPa. The only difference is that with the increase of consolidation pressures, the adsorption-desorption isotherms of the consolidated sample gradually dropped slightly at higher relative pressure ($P/P_0 = 1$), corresponding to a slight, gradual reduction in the specific surface area of the material with increasing vertical pressure (from 57.66 m^2/g in slurry state to 51.38 m^2/g under 2 MPa vertical stress).This cannot be explained by the elongation of the pores during one-dimensional loading, seen later in the SEM photographs, as this would have for effect to increase the specific surface area. This could be an indication on the other hand that, unlike what has been observed in other remoulded and natural clays, the compression affects other pores than those detected by MIP, in the micro- to mesopore size range.

The evolution of the MIP curves with loading is shown in **figure 9**. The assumption is that although the four curves were obtained from different specimens, the good accuracy of the initial void ratio at the start of oedometer testing allows interpreting them as representing the evolution of a single curve. Unlike what was found for Champlain sensitive clays (e.g. Delage and Lefebvre, 1984) or Speswhite kaolin (e.g. Griffiths and Joshi 1990, Yu et al., 2016), where the largest pores were first collapsed, and that an increased stress was progressively collapsing, in an orderly manner, smaller and smaller pores, here there is no complete superimposition of the sections of the PSD curves of smaller pores under the different consolidation pressures (**Fig.9a**). Instead, here, a stress increment simultaneously affects a large range of pores: compression from slurry state to 100 kPa results in a significant decrease in void ratio from 1.97 down to 1.05, with a collapse of most of the pores with entrance diameter larger than 2 μm. This suggests that the significant decrease in void ratio is mainly due to the collapse of the

larger inter-aggregate pores observed in the SEM photo of **figure 7**. But the compression under 100 kPa also affects all pores with entrance diameter down to 0.2 µm, as clearly evidenced in the density function curves (**Fig.9b**) in which there is a global leftwards shift of their peak towards small diameters: 0.95 µm at 100 kPa, 0.47 µm at 400 kPa, 0.26 µm at 1,000 kPa and 0.14 µm at 2,000 kPa. The shape of the density function curves becomes sharper and sharper, indicating better and better sorted pore size distribution under increased stress.

A similar evolution can also be observed in the SEM photographs (**Fig.10** and **12**) where the average distance between two aggregates in both vertical and horizontal planes, measured with a ruler, decreases from approximately 1 µm at 100 kPa, to 0.5 µm at 400 kPa, then 0.3 µm at 1,000 kPa, and finally to 0.2 µm at 2,000 kPa, suggesting that vertical loading mainly translates at the pore scale into changes of inter-aggregate porosity. Using the SEM images for a better, quantitative comparison with the MIP measurements was not possible because of limitations of the technique such as the insufficient magnification, which does not allow pores smaller than 1 µm to be identified accurately, because of possible confusion between pores and other particle shadows when segmenting, or the randomness in looking at selected planes.

It is interesting to note that in **figure 9**, although no exact superposition is observed in the smaller pore size ranges, the PSD curves at all vertical stresses nearly coincide for entrance pore diameters smaller than about 0.05 µm, which belongs to the intra-aggregate porosity defined above and is the upper boundary of the mesopores. The range of pores with entrance diameters smaller than around 0.05 µm can thus be interpreted as representing the intra-aggregate porosity, at least up to 2,000 MPa, spreading over the IUPAC micro- and meso-pore sizes. While it is usually interpreted that intra-aggregate pores, although in the less reliable range of pores detected by MIP, are not affected by compression, data from the gas adsorption tests provide additional information on the porosity at the very small scale. It is not easily possible to compare data obtained by MIP and N_2GA tests directly, as they are derived

according to different physical phenomena and distinct theories and assumptions, but they can provide complementary insight into the intra-aggregate porosity. For example, in our case, it is observed from **figure 9a** that there is a noticeable difference between the global void ratio, e, and the mercury intruded void ratio, e_m, at low pressures, which gradually narrows down as the pressure increases, to become almost negligible at the highest consolidation stress level (2,000 kPa). Data in **Table 4** show indeed that at the higher consolidation pressure, the difference between e and e_m is less than 0.01 and mainly attributed to the non-intruded micro- to meso-porosity, while at the lower pressures, this difference is affected by the three types of porosities together. It is also found that the pores unavailable by the MIP technique used all became smaller, similarly to the micro-porosity, as the consolidation pressure increased. This reduction of the non-intruded porosity, likely made up of pores between montmorillonite platelets, is an indication that the compression also affects pores smaller than the smallest mercury penetrated ones and is probably due to the rearrangement of the particles composing the aggregates. This would be compatible with nW hydration observations, since the transition between 4W and 3W occurs around 0.1 MPa, according to Sayiouri et al. (2004). The change in specific surface area also points out to changes in the clay structure at much smaller scales (Sayiouri et al., 2004). Further evidence and studies such as designing specialized gas adsorption and small angle X-ray scattering tests are needed to confirm it.

4.3 Evolution of pore morphology and orientation during compression

The characterization of the evolution of pore morphology during consolidation is based on the image processing of SEM pictures taken for the specimens under the four applied vertical stresses. The geometries of the pores were extracted according to different threshold values of pore segmentation as indicated in **figures 11** (vertical plane) and **13** (horizontal plane). While

the gas adsorption data presented earlier suggested deformation of the aggregates, the resolution of the SEM images mainly allowed the inter-aggregate pores to be mapped.

At lower consolidation pressures (**Fig.11a** and **13a**), many pores of good circularity can be observed between the assemblies of aggregates. The number of pores reduces significantly at higher consolidation pressures (**Fig.11d** and **13d**), and almost all the remaining pores have become horizontal and elongated, aligning parallel to the compacted particle layer. Analyses of the pore aspect ratios on the vertical and horizontal planes during compression show that the distributions follow a log-normal distribution (**Fig.14** and **15** respectively). The log-normal fitting curves of the pore aspect ratio on the vertical and horizontal planes at the different stages of consolidation are replotted in **figure 16**. The distributions on the horizontal plane tend to be narrower than on the vertical plane, and to plot to the left of the curves for the vertical plane. This suggests a greater uniformity of pore shapes on the horizontal plane while the pores on the vertical plane are more elongated, with values of aspect ratio extending to 6 or above. The increase in stress level causes the distributions on the vertical plane, i.e. the plane of vertical deformations, to shift slightly to the right as the pores gradually become flatter. The variation in pore shape on that plane occurs in the range of aspect ratios 1-6, while pores with initially elongated shapes (aspect ratio larger than 6) do not seem to be affected by the compression. In the horizontal plane, i.e. the plane of horizontal deformations (zero for one-dimensional compression), the shapes remain essentially the same, in the range 1-4 aspect ratio, indicating that the consolidation pressure has a limited effect on these pores**.** Values of the mean and standard deviation of the aspect ratio, computed by the damped least-squares method (**Table 5**) similarly show that the mean values for both planes gradually become larger during the consolidation, with bigger changes on the vertical plane, suggesting that an anisotropy of the pore shape developed progressively with the loading, the values on the vertical plane remaining higher than on the horizontal plane. The compression seems to create a more uniform

distribution of pore shapes, with decreasing standard deviation for both planes. This may be due to the fact that the distributions tend to get a more developed left branch as the loading increases (i.e. almost round pores disappear or at least are much less frequent, and some more elongated pores are compressed to what seems complete closure).

Global rose diagrams are used to present the pore orientation at different stress levels based on the angular distribution diagram of the pore orientation with respect to the vertical (**Fig.17** and **18**). The whole range of pore orientation (0-180°) is divided into 12 groups, each group equal to 15° following Hattab and Fleureau (2010). The number of pores counted for each group, divided by the total number to get the percentage in each group, is shown in the rose diagram as a function of their orientation. For the vertical plane (**Fig.17**), a gradual change is observed towards a preferential horizontal pore orientation. As the pressure increases, the degree of pore parallelism also increases. In **figure 17d**, although some pores are oriented in the 0-15°, 15-30°, 30-45° and 45-60° ranges, they are relatively few compared to the pores oriented between 60-90°, and especially 75-90°. These pore reorientation and parallelism do not occur in the global rose diagram of the horizontal plane (**Fig.18**), with no obvious preferential pore orientations on that plane. This indicates that a strong anisotropy with a preferential orientation of pores normal to the loading direction is induced during one-dimensional compression. This has been implied in other studies based on observations on the vertical plane, but here the data for the horizontal plane confirm the fabric anisotropy resulting from to the reorientation and rearrangement of clay particles in the horizontal direction.

5. Conclusions

This work highlights the pore structure of a reconstituted illite-dominant clay and the evolution of pore sizes and shapes during one-dimensional compression. Pore sizes in the range of 5 nm to 350 μm were examined using a combination of mercury intrusion porosimetry and scanning electron microscopy techniques, with complementary information from nitrogen adsorption

tests. Although a certain subjectivity and randomness might exist when analysing the pore structure of clay, it is believed that the particular care taken during the experimental operation minimized them, and that the results presented are representative of the illitic clay behaviour. By performing gas adsorption tests in addition to the MIP and SEM tests it has been possible to obtain information on the very small pores, for which there is an indication that in this clay the micropores, smaller than 5 nm, may be affected by the loading, although further tests using the gas sorption and small angle X-ray scattering techniques are necessary to confirm it. Four main conclusions are therefore derived from this work:

1. The total porosity of reconstituted illitic clay covers three ranges of pores, adopting the IUPAC terminology: micropores (< 2 nm), mesopores (2-50 nm) and macropores (>50 nm).

2. Mapping of the porosity during 1D compression shows that the clay pores exist over the three size ranges during all stages of consolidation, at least up to 2,000 kPa.

3. From the MIP data, the consolidation seems to affect principally pores larger than 50 nm, which corresponds to the upper bound of the mesopores range, and account for about 80% of the total porosity. This indicates that the structure of the clay, visibly aggregated from SEM images, can be characterized by intra-aggregate pores (smaller than about 50 nm) and inter-aggregate pores (larger than about 50 nm). Relating the average diameter of the intra-aggregate pores to the thickness of the illite platelets following the brick model, platelets comprise about 50-100 layers.

4. During one-dimensional compression, the largest inter-aggregate pores are first collapsed, followed by the progressive compression of smaller and smaller pores as the stress increases. The macroscopic deformation observed therefore mainly translates at the pore scale into changes of inter-aggregate porosity. A lack of complete superposition of MIP curves in the

small pore range, and data from gas adsorption results, suggest that the intra-aggregate porosity also decreases with load level, probably due to the rearrangement of the particles composing the aggregates, and that this is accompanied by a reduction in specific surface area.

5. Examination of the pores' shape and orientation on both vertical and horizontal planes during the one-dimensional compression points out to some induced anisotropy with a preferential orientation of pores normal to the loading direction. This is consistent with previous observations of anisotropy induced by 1D compression, usually observed from micrographs vertical planes, but now confirmed by data from the horizontal plane. Combining vertical and horizontal distributions of pore shapes shows that the overall morphology of the pores also becomes anisotropic, becoming flatter in the direction of the main deformation.

6. Acknowledgements

M. Yanhao Zheng is grateful to the China Grants Council for the award of a full scholarship (CSC No. 201808060470) allowing him to carry out his research at UCL. The authors would like to thank Dr Zuo at Xi'an Jiatong University in China for providing the loess. The assistance of the technical team at Navier/CERMES laboratory to run the freeze-drying and MIP tests (MM. X. Boulay and E. De Laure) is greatly acknowledged. The authors are finally grateful to Mrs ZHOU Xiuqing, from the School of Chemistry at Jilin University, for her help conducting the N_2GA tests, and to the College of Construction Engineering, Jilin University, where the mass-based BT-9300LD laser diffraction particle size analysis was carried out.

7. Data accessibility

Data are available from the corresponding author on request.

8. References

Barden, L. and Sides, G.R. (1970). Engineering behavior and structure of compacted clay. *Journal of the Soil Mechanics and Foundations Division* **96**(4): 1171-1200.

Brunauer, S., Emmett, P.H. & Teller, E. (1938). Adsorption of gases in multimolecular layers. *Journal of the American chemical society* **60**(2): 309-319.

Burland, J.B. (1990) On the compressibility and shear strength of natural clays. *Géotechnique* **40**(3): 329-378.

Burton, G.J., Pineda, J.A., Sheng, D. and Airey, D. (2015). Microstructural changes of an undisturbed, reconstituted and compacted high plasticity clay subjected to wetting and drying. *Engineering Geology* **193**: 363-373.

Cetin, H. & Söylemez, M. (2004). Soil-particle and pore orientations during drained and undrained shear of a cohesive sandy silt clay soil. *Can. Geotech. J.* **41**(6): 1127-1138.

Chow, J.K., Li, Z. and Wang, Y.H. (2019). Comprehensive microstructural characterizations of 1-D consolidated kaolinite samples with fabric tensors and pore elongation factors. *Engineering Geology* **248**: 22-33.

Conner, W.C., Cevallos-Candau, J.F., Weist, E.L., Pajares, J., Mendioroz, S. & Cortes, A. (1986). Characterization of pore structure: porosimetry and sorption. *Langmuir* **2**(2): 151-154.

Cotecchia, F. & Chandler, R.J. (1998). One-dimensional compression of natural clay: Structural changes and mechanical effects. In A. Evangelista & L. Picarelli (eds), *The Geotechnics of Hard Soils-Soft Rocks*; Proc. second intern. symp., Napoli, 12-14 October 1998. Rotterdam: Balkema, 103-114.

Cotecchia, F., Amorosi, A. & Mitaritonna, G. (2014). Experimental investigation of the evolution of elastic stiffness anisotropy in a clayey soil. *Géotechnique* **64**(6): 463-475.

Diamond, S. (1970) Pore size distributions in clays. *Clays and Clay Miner*. **18**(1) : 7-23.

Delage, P. & Pellerin, F.M. (1984). Influence de la lyophilisation sur la structure d'une argile sensible du Québec. *Clay Miner*. **19**(2): 151-160.

Delage, P., Tessier, D. & Marcel-Audiguier, M. (1982). Use of the Cryoscan apparatus for observation of freeze-fractured planes of a sensitive Quebec clay in scanning electron microscopy. *Can. Geotech. J.* **19**(1): 111-114.

Delage, P., Marcial, D., Cui, Y.J. & Ruiz, X. (2006). Ageing effects in a compacted bentonite: a microstructure approach. *Géotechnique* **56**(5): 291-304.

Delage, P. & Lefebvre, G. (1984). Study of the structure of a sensitive Champlain clay and of its evolution during consolidation. *Can. Geotech. J*. **21**(1): 21-35.

Delage, P. (2010). A microstructure approach to the sensitivity and compressibility of some Eastern Canada sensitive clays. *Géotechnique* **60**(5): 353-368.

Delage, P. & Tessier, D. (2020). Macroscopic effects of nano and microscopic phenomena in clayey soils and clay rocks. *Geomechanics for Energy and the Environment* p. 100177.

Gao, Q.F., Jrad, M., F Hattab, M., Fleureau, J.M. & Ameur, L.I. (2020). Pore Morphology, Porosity, and Pore Size Distribution in Kaolinitic Remolded Clays under Triaxial Loading. *Int. J. Geomech.* **20**(6):04020057.

Gillott J.E. (1969). Study of the fabric of fine-grained sediments with the scanning electron microscope. *Journal of Sedimentary Petrology* 39: 90-105.

Griffiths, F.J. & Joshi, R.C. (1989). Change in pore size distribution due to consolidation of clays. *Géotechnique* **39**(1): 159-167.

Gregg S.J. and Sing K.S.W. (1983). Adsorption, Surface Area, and Porosity (2nd ed.). New York: Academic press.

Hattab, M. & Fleureau, J.M. (2010). Experimental study of kaolin particle orientation mechanism. *Géotechnique* **60**(5): 323-331.

Hattab, M., Hammad, T., Fleureau, J.M. and Hicher, P.Y. (2013). Behaviour of a sensitive marine sediment: microstructural investigation. *Géotechnique* **63**(1): 71-84.

Hattab, M., Hammad, T. and Fleureau, J.M. (2015). Internal friction angle variation in a kaolin/montmorillonite clay mix and microstructural identification. *Géotechnique* **65**(1): 1-11.

Hicher, P.Y., Wahyudi, H. and Tessier, D. (2000). Microstructural analysis of inherent and induced anisotropy in clay. *Mechanics of Cohesive - frictional Materials: An International Journal on Experiments, Modelling and Computation of Materials and Structures* **5**(5): 341-371.

Kuila, U. (2013). *Measurement and interpretation of porosity and pore-size distribution in mudrocks: The hole story of shales*. PhD thesis, Colorado School of Mines.

Li, X. and Zhang, L.M. (2009). Characterization of dual-structure pore-size distribution of soil. *Canadian geotechnical journal* **46**(2): 129-141.

Lubelli, B., De Winter, D.A.M., Post, J.A., Van Hees, R.P.J. and Drury, M.R. (2013). Cryo-FIB–SEM and MIP study of porosity and pore size distribution of bentonite and kaolin at different moisture contents. *Applied clay science* **80**: 358-365.

Maruyama, I., Rymeš, J., Vandamme, M. & Coasne, B. (2018). Cavitation of water in hardened cement paste under short-term desorption measurements. *Materials and Structures* **51**(6): 1-13.

Media Cybernetics. Image-Pro Plus - application notes. Silver Spring: Media Cybernetics; 2002. Available from: URL: *http://www.mediacy.com/action.htm*.

Menaceur, H., Delage, P. , Tang A.M. & Talandier J. (2016). The Status of Water in Swelling Shales: An Insight from the Water Retention Properties of the Callovo-Oxfordian Claystone." *Rock Mechanics and Rock Engineering* 49 (12).

Monroy, R., Zdravkovic, L. & Ridley, A. (2010). Evolution of microstructure in compacted London Clay during wetting and loading. *Géotechnique* **60**(2): 105-119.

Moyano, B., Spikes, K.T., Johansen, T.A. & Mondol, N.H. (2012). Modeling compaction effects on the elastic properties of clay-water composites. *Geophysics* **77**(5): D171-D183.

Mitchell, J.K. and Soga, K. (2005). *Fundamentals of soil behavior* (Vol. 3). New York: John Wiley & Sons.

Ninjgarav, E., Chung, S.G., Jang, W.Y. & Ryu, C.K. (2007). Pore size distribution of Pusan clay measured by mercury intrusion porosimetry. *KSCE Journal of Civil Engineering* **11**(3): 133-139.

Penumadu, D. & Dean, J. (2000). Compressibility effect in evaluating the pore-size distribution of kaolin clay using mercury intrusion porosimetry. *Can. Geotech. J.* **37**(2): 393-405.

Pires, L.F., Cooper, M., Cássaro, F.A.M., Reichardt, K., Bacchi, O.O.S. and Dias, N.M.P. (2008) Micromorphological analysis to characterize modifications in the internal structure of soil samples submitted to wetting and drying cycles. *Catena* **72**(2): 297-304.

Rocchi, I. & Coop, M.R. (2014). Experimental accuracy of the initial specific volume. *Geotech. Testing J.* **37**(1): 169-175.

Rouquerol J., Rouquerol F. and Sing K.S.W. (1998). *Absorption by Powders and Porous Solids*. Academic press, ISBN 0080526012.

Saiyouri, N., Tessier, D. & Hicher, P.Y. (2004). Experimental study of swelling in unsaturated compacted clays. *Clay Miner.* **39**(4): 469-479.

Shipton, B. & Coop, M.R. (2012). On the compression behaviour of reconstituted soils. *Soils Found*. **52**(4): 668-681.

Sing, K.S.W., Everett, D.H., Haul, R.A.W., Moscou, L., Pieroti, R.A., Rouquerol, J. & Siemieniewska, T. (1985). Reporting physisorption data for gas/solid systems with special reference to the determination of surface area and porosity (Recommendations 1984). *Pure and applied chemistry* **57**(4): 603-619.

Skempton, A.W. & Sowa, V.A. (1963). The behaviour of saturated clays during sampling and testing. *Géotechnique* **13**(4): 269-290.

Tessier D. (1991). Behaviour and microstructure of clay minerals. Chapter 14 in *Soil Colloids and their Association in Aggregates*. De Boodt, Hayes, Herbillon eds, Plenum publishing corporation.

Tovey N.K. & Wong K.Y. (1973). The preparation of soils and other geological materials for the scanning electron microscope. *Proceedings of the International Symposium on Soil Structure*. Gothenburg, Sweden, 59 – 67.

Wang, Y.H. & Xu, D. (2007). Dual porosity and secondary consolidation. *J. Geotech. Geoenviron. Engng, ASCE* **133**(7): 793-801.

Washburn, E.W., 1921. The dynamics of capillary flow. *Physical review* **17**(3), p.273.

Wong, H.S., Head, M.K. & Buenfeld, N.R. (2006). Pore segmentation of cement-based materials from backscattered electron images. *Cement and Concrete Research* **36**(6): 1083-1090.

Xu, L. & Coop, M.R. (2016). Influence of structure on the behavior of a saturated clayey loess. *Can. Geotech. J.* **53**(6): 1026-1037.

Yu, C.Y., Chow, J.K. & Wang, Y.H. (2016). Pore-size changes and responses of kaolinite with different structures subject to consolidation and shearing. *Engineering Geology* **202**: 122-131.

Zeng, L.L., Cui, Y.J., Conil, N., Zghondi, J., Armand, G. & Talandier, J., 2017. Experimental study on swelling behaviour and microstructure changes of natural stiff Teguline clays upon wetting. *Can. Geotech. J*. **54**(5): 700-709.

Zuo, L., 2019. Personal communication.

Tables

Table 1. Results from XRF analysis of the clay.

	Na_2O	MgO	Al_2O_3	SiO_2	P_2O_5	SO_3	K_2O	CaO	TiO_2	Fe_2O_3
Content (%)	12.91	12.05	18.05	27.29	0.16	1.44	3.66	14.78	1.28	7.14

Table 2. Geotechnical index properties of the clay.

Property	Value
Specific gravity	2.73
Specific surface area (m^2/g)	57.66
Liquid limit (%)	55.5
Plastic limit (%)	20.1
Plasticity index	35.4
Grain size distribution	
Sand > 0.06 mm (%)	0
Silt 0.002-0.06 mm (%)	50.2
Clay < 0.002 mm (%)	49.8

Table 3. Details of specimens subjected to one-dimensional compression and micro-analysis

Specimen No.	Maximum consolidation pressure	Water content* w (%)	Saturation S_r (%)	Void ratio*
C0 (Slurry)	0 kPa	66.25	97.25	1.97
C100	100 kPa	38.43	100	1.05
C400	400 kPa	31.21	100	0.81
C1000	1000 kPa	27.52	100	0.65
C2000	2000 kPa	21.05	100	0.54

*at the end of one-dimensional compression test

Table 4. Evolution of void ratio during 1D compression, calculated from equations (1) to (3) and volumetric strains, and from N_2 gas adsorption and MIP tests.

	C100	C400	C1000	C2000
Global void ratio, e	1.05	0.81	0.65	0.54
Mercury intruded void ratio, e_m	0.96	0.73	0.61	0.51
Difference between e and e_m	0.09	0.06	0.04	0.03
Void ratio occupied by pores < 5 nm (from N_2GA tests)	0.048	0.039	0.031	0.022

Table 5. Statistical parameters of the normal distribution curves for the aspect ratio of pores.

	Vertical Plane				Horizontal Plane			
	C100	C400	C1000	C2000	C100	C400	C1000	C2000
Mean μ	2.02	2.42	2.66	2.95	1.91	2.16	2.29	2.40
Standard deviation σ	0.57	0.51	0.49	0.43	0.48	0.42	0.41	0.34
Total count	1186	937	704	398	1353	996	768	449

Figures

Figure 1. Grain size distribution.

Figure 2. Cumulative grey scale histogram from the vertical plane of C100, shown as example of how to determine the threshold of pore segmentation based on the overflow method-here the threshold is 69.

Figure 3. Stages of processing for the SEM pictures: (a) SEM image of the reconstituted clay at 100 kPa; (b) Segmentation into pores and clay matrix; (c) Extraction of the pore outlines; (d) Final image showing ellipses equivalent to the pore outlines.

Figure 4. Schematic view of (a) pore orientation and (b) pore aspect ratio for an elliptical pore.

Figure 5. Oedometer compression and swelling curves for the reconstituted clay.

Figure 6. Adsorption-desorption isotherm of the slurry clay at standard temperature and pressure (STP) where the standard temperature is 273 K (0° Celsius or 32° Fahrenheit) and the standard pressure is 1 atm pressure.

Figure 7. Micrographs of the clay in slurry state.

Figure 8. Pore size distribution curves in slurry state in the range of 0.005 to 350 μm: (a) cumulative curve and (*b*) density function curve.

Figure 9. Pore size distribution curves of the reconstituted clay at different vertical consolidation pressures in the range of 0.005 to 350 μm: (a) cumulative curve and (*b*) density function curve.

Figure 10. SEM pictures of the vertical plane of reconstituted clay under the consolidation pressures of: (a) 100 kPa; (b) 400 kPa; (c) 1000 kPa; and (d) 2000 kPa.

Figure 11. Extracted pore shapes on the vertical plane of the reconstituted clay under increasing consolidation pressure. Threshold values are in []. (a) 100 kPa [69]; (b) 400 kPa [58]; (c) 1000 kPa [70]; (d) 2000 kPa [75].

Figure 12. SEM pictures of the horizontal plane of the reconstituted clay under the consolidation pressures of: (a) 100 kPa; (b) 400 kPa; (c) 1000 kPa; and (d) 2000 kPa.

Figure 13. Extracted pore shapes on the horizontal plane of the reconstituted clay under increasing consolidation pressure. Threshold values are in []. (a) 100 kPa [71]; (b) 400 kPa [64]; (c) 1000 kPa [77]; (d) 2000 kPa [62].

Figure 14. Evolution of the aspect ratio of pores on the vertical plane during consolidation.

Figure 15. Evolution of the aspect ratio of pores on the horizontal plane during consolidation.

Figure 16. Fitting curves of aspect ratio of pores on the vertical and horizontal planes during consolidation.

Figure 17. Evolution of the distribution of pore orientations on the vertical plane during consolidation: for a maximum consolidation stress of (a) 100 kPa; (b) 400 kPa; (c) 1000 kPa; and (d) 2000 kPa.

Figure 18. Evolution of the distribution of pore orientations on the horizontal plane during consolidation: for a maximum consolidation stress of (a) 100 kPa; (b) 400 kPa; (c) 1000 kPa; and (d) 2000 kPa

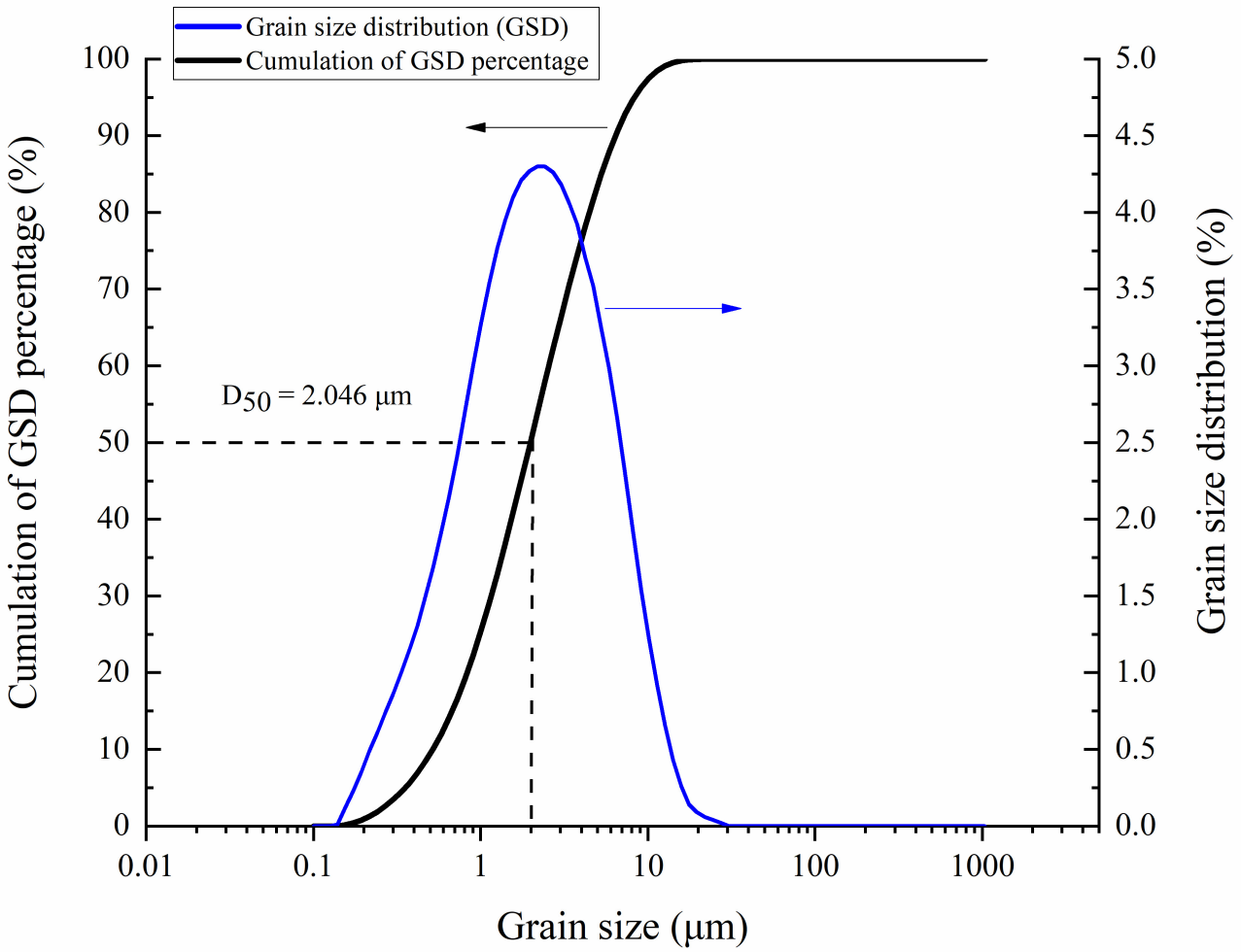
Grain size distribution (GSD)
Cumulation of GSD percentage
D50 = 2.046 μm
Cumulation of GSD percentage (%)
Grain size distribution (%)
Grain size (μm)
0
10
20
30
40
50
60
70
80
90
100
0.0
0.5
1.0
1.5
2.0
2.5
3.0
3.5
4.0
4.5
5.0
0.01
0.1
1
10
100
1000

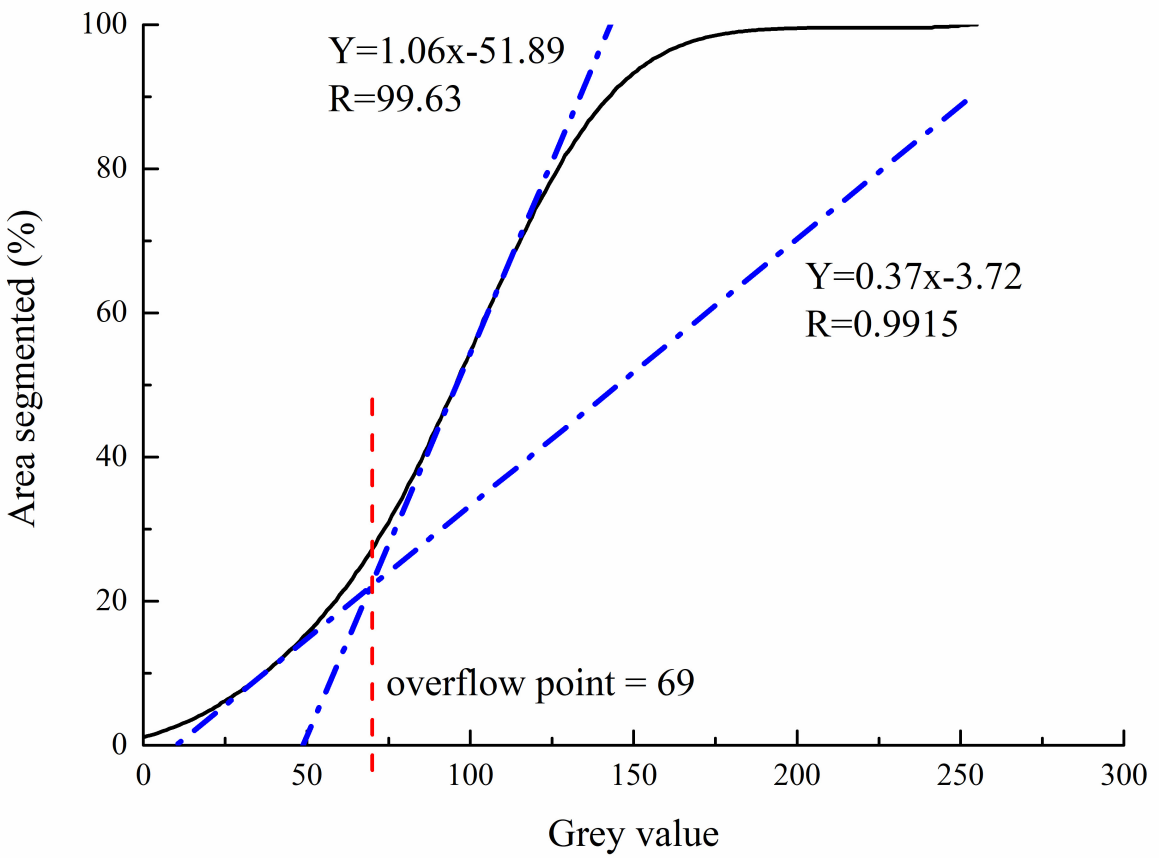
Y=1.06x-51.89
R=99.63
Y=0.37x-3.72
R=0.9915
overflow point = 69
Area segmented (%)
Grey value
0
20
40
60
80
100
0
50
100
150
200
250
300

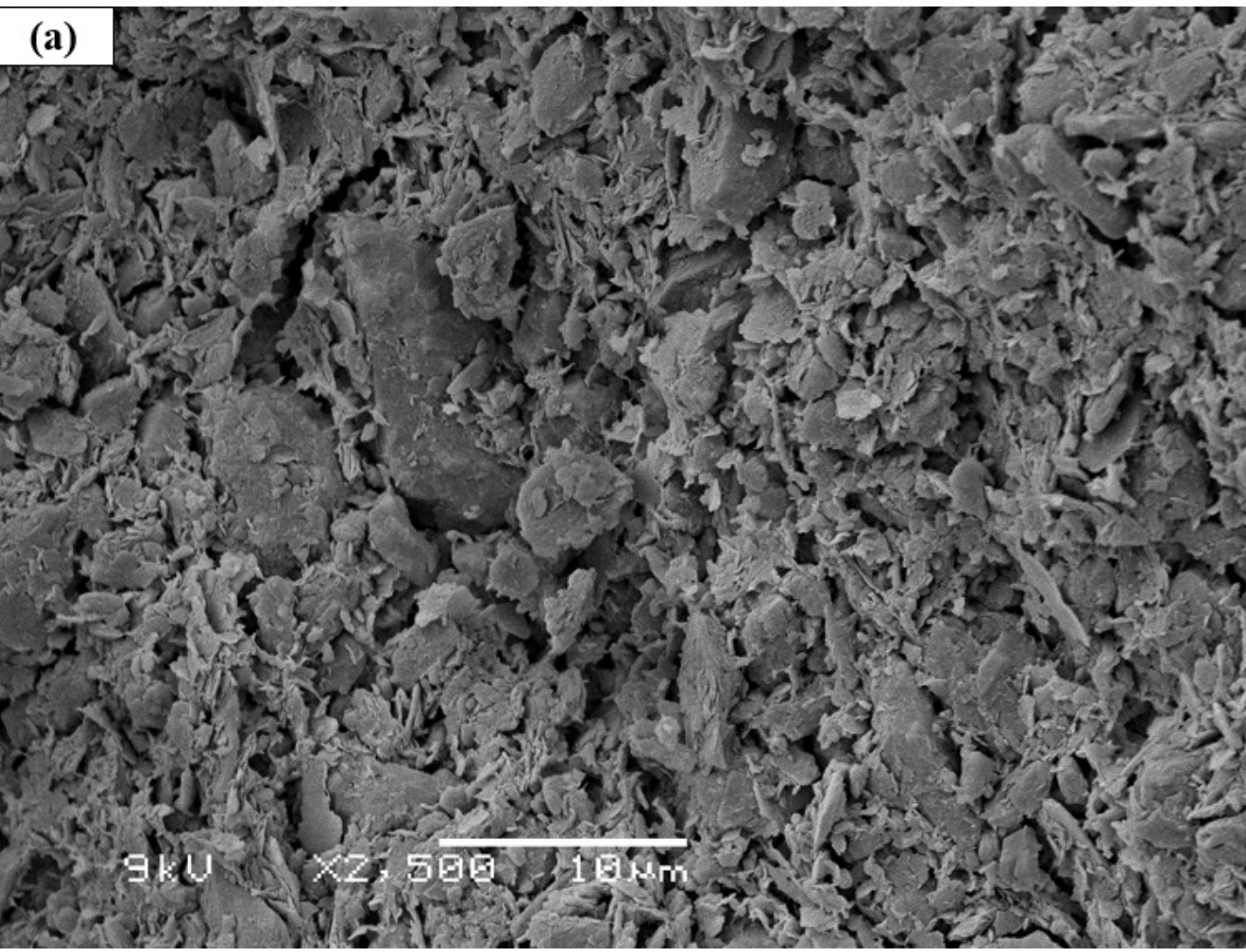
(a)
9kV X2,500 10μm

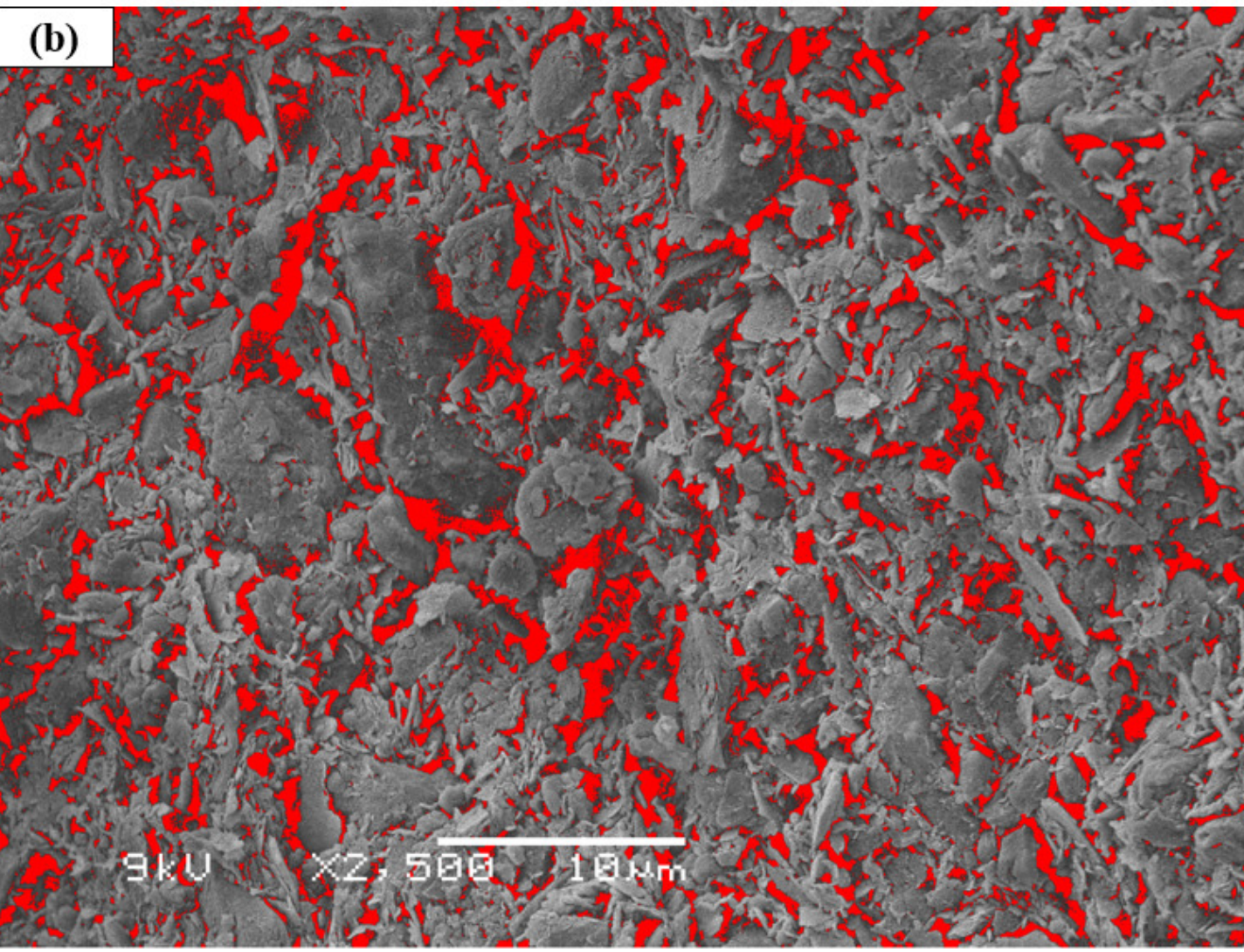
(b)
9kU X2,500 10μm

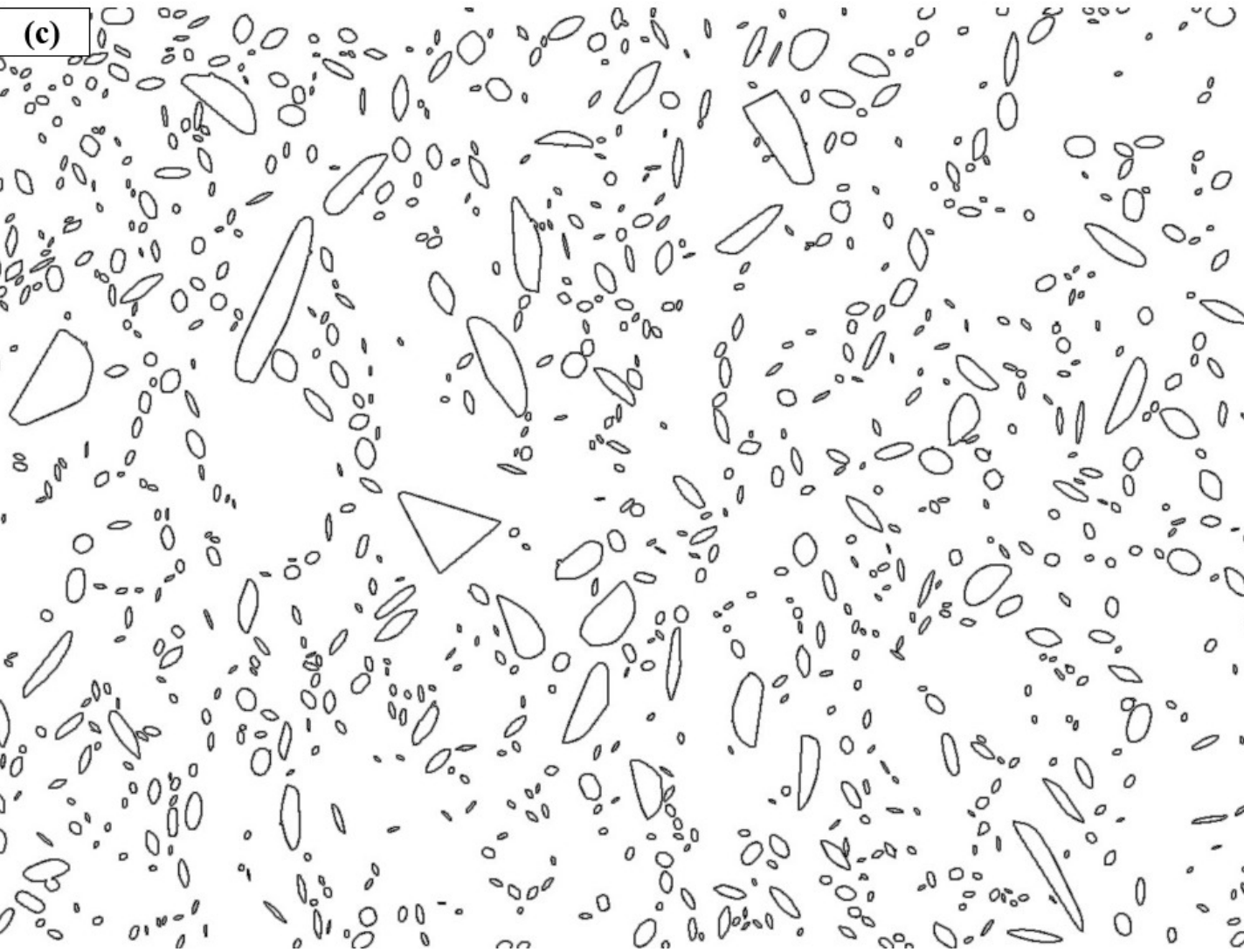
(c)

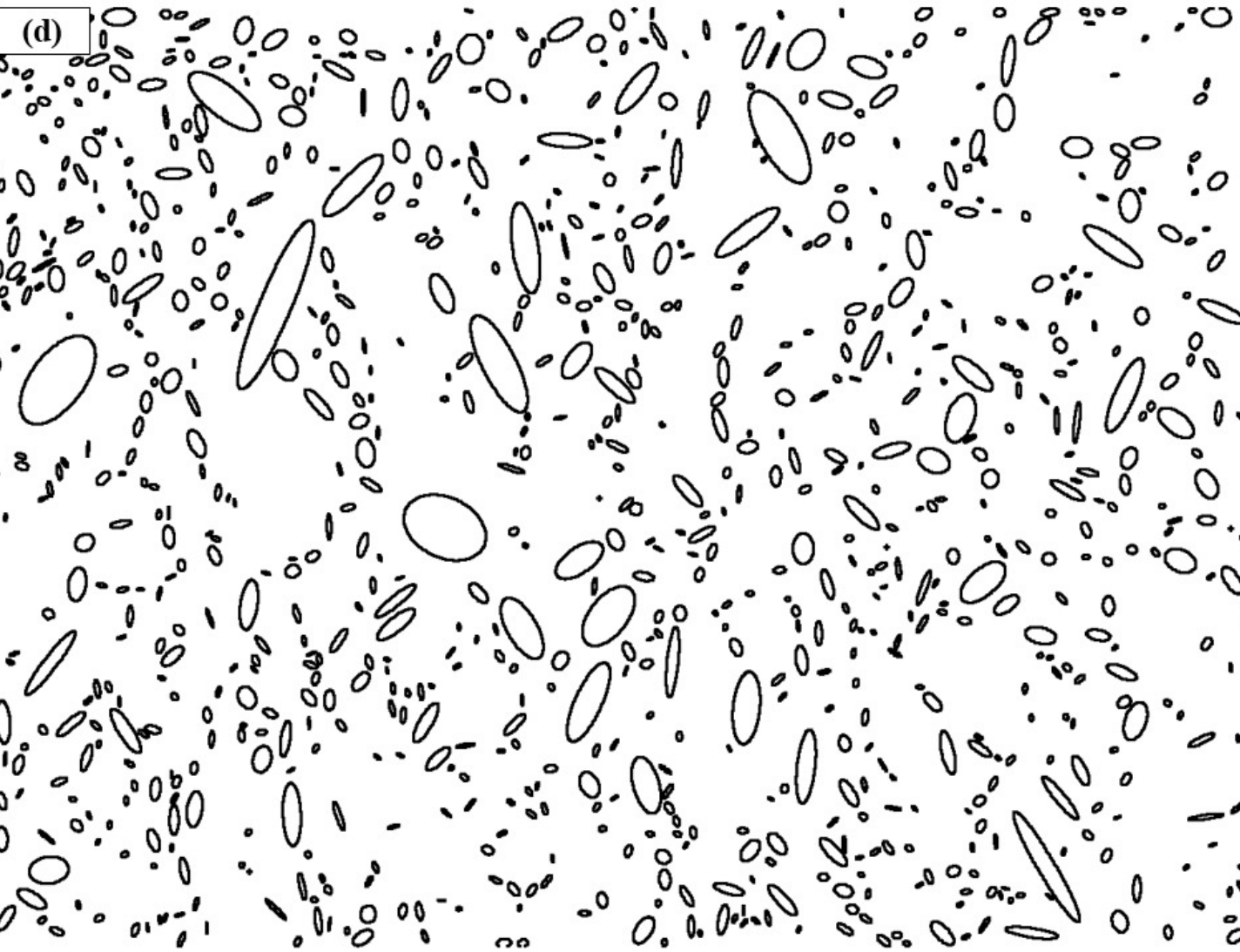
(d)

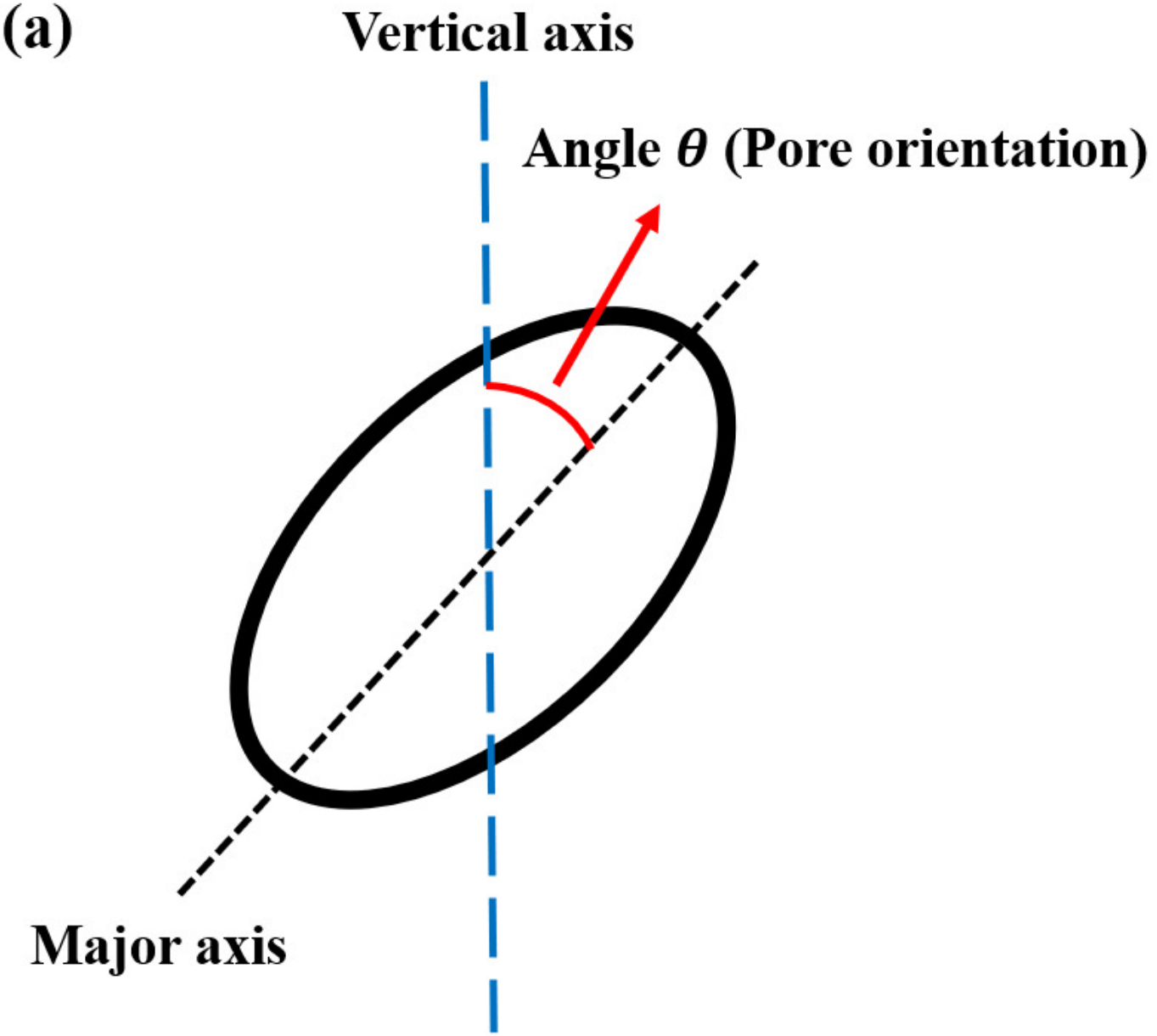
(a)
Vertical axis
Angle θ (Pore orientation)
Major axis

(b)

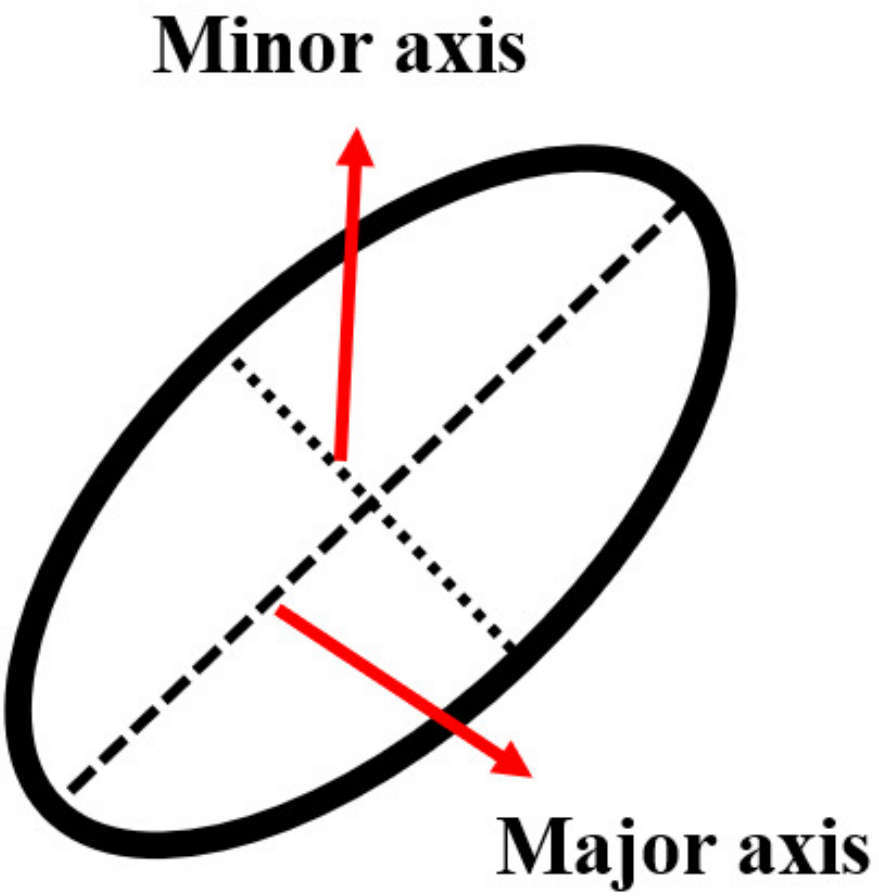

Aspect ratio = Major axis / Minor axis

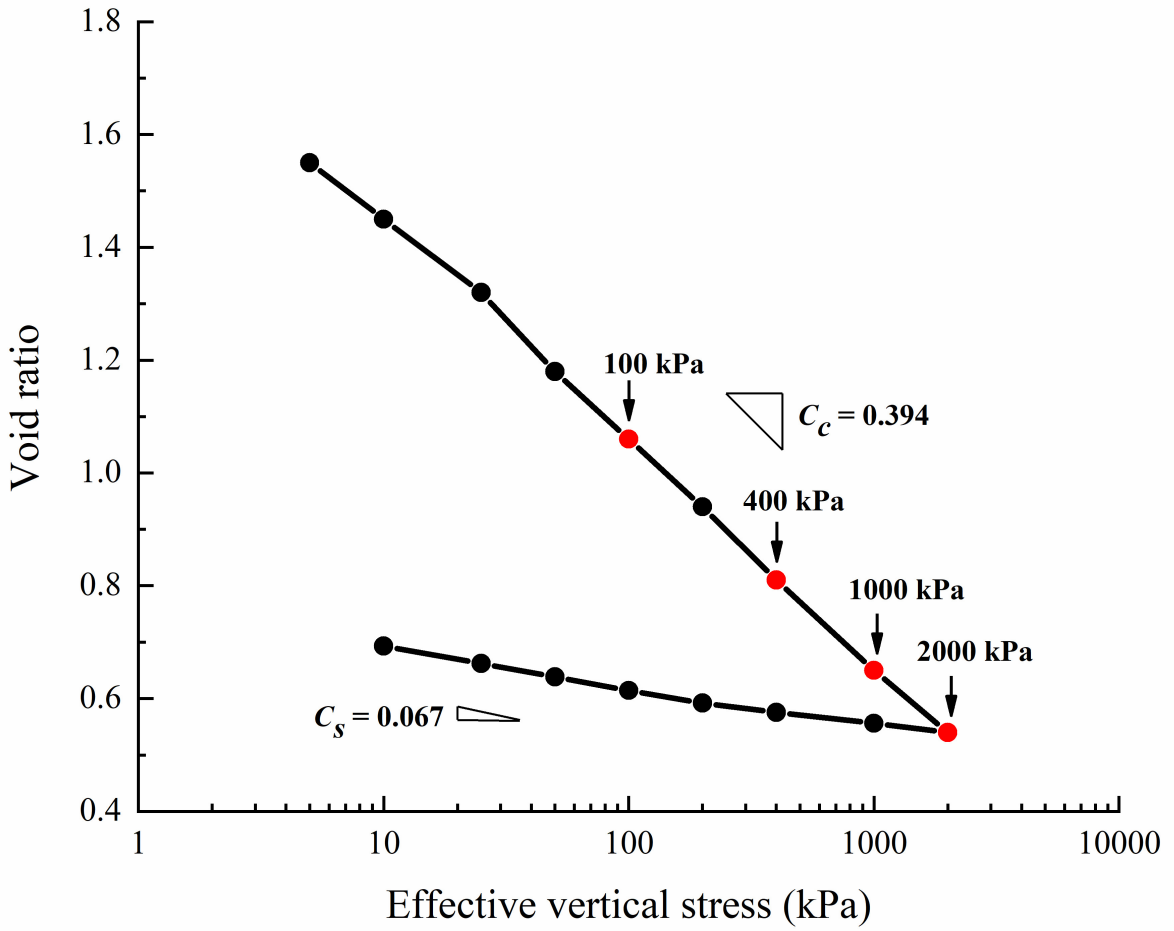
1.8
1.6
1.4
1.2
1.0
0.8
0.6
0.4
Void ratio
1
10
100
1000
10000
Effective vertical stress (kPa)
100 kPa
400 kPa
1000 kPa
2000 kPa
C_c = 0.394
C_s = 0.067

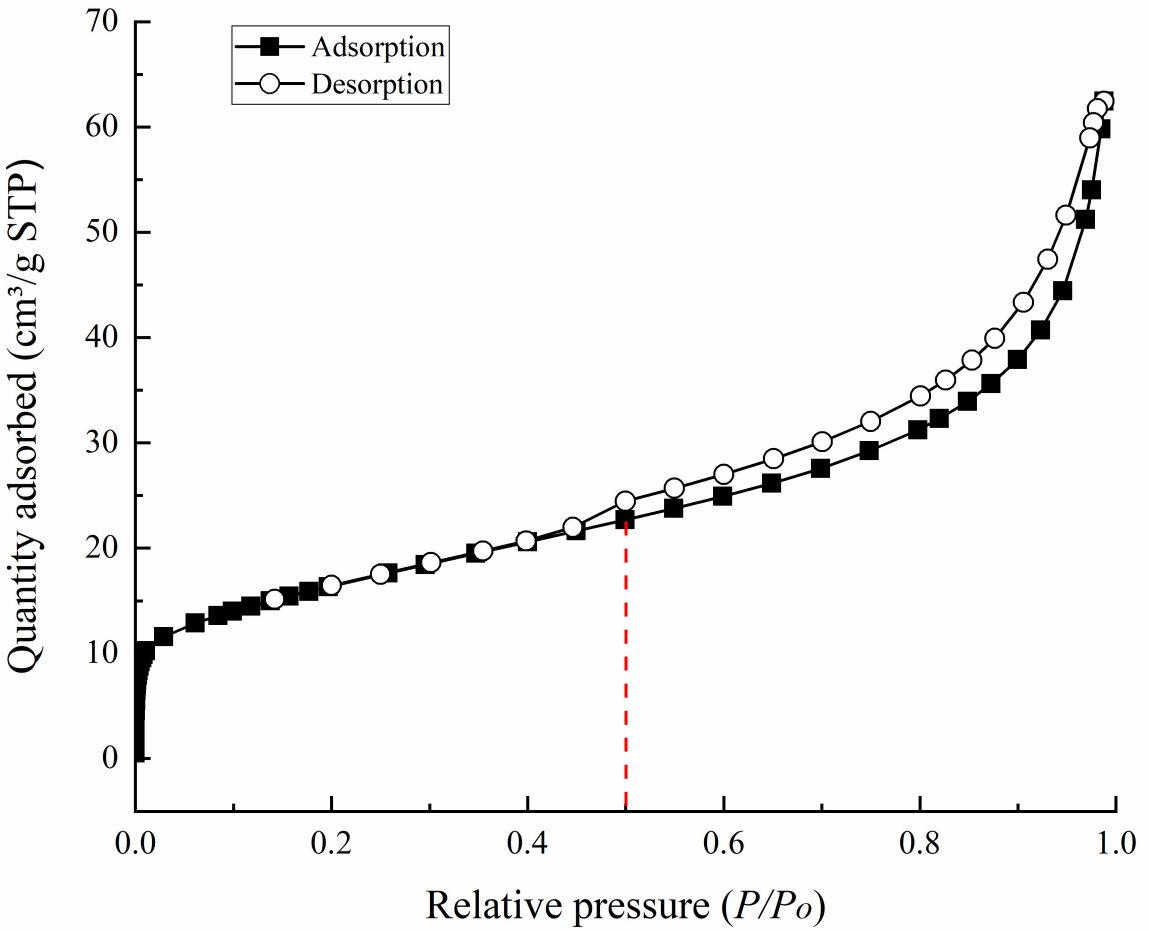
Adsorption
Desorption
Quantity adsorbed (cm³/g STP)
Relative pressure (P/Po)
0
10
20
30
40
50
60
70
0.0
0.2
0.4
0.6
0.8
1.0

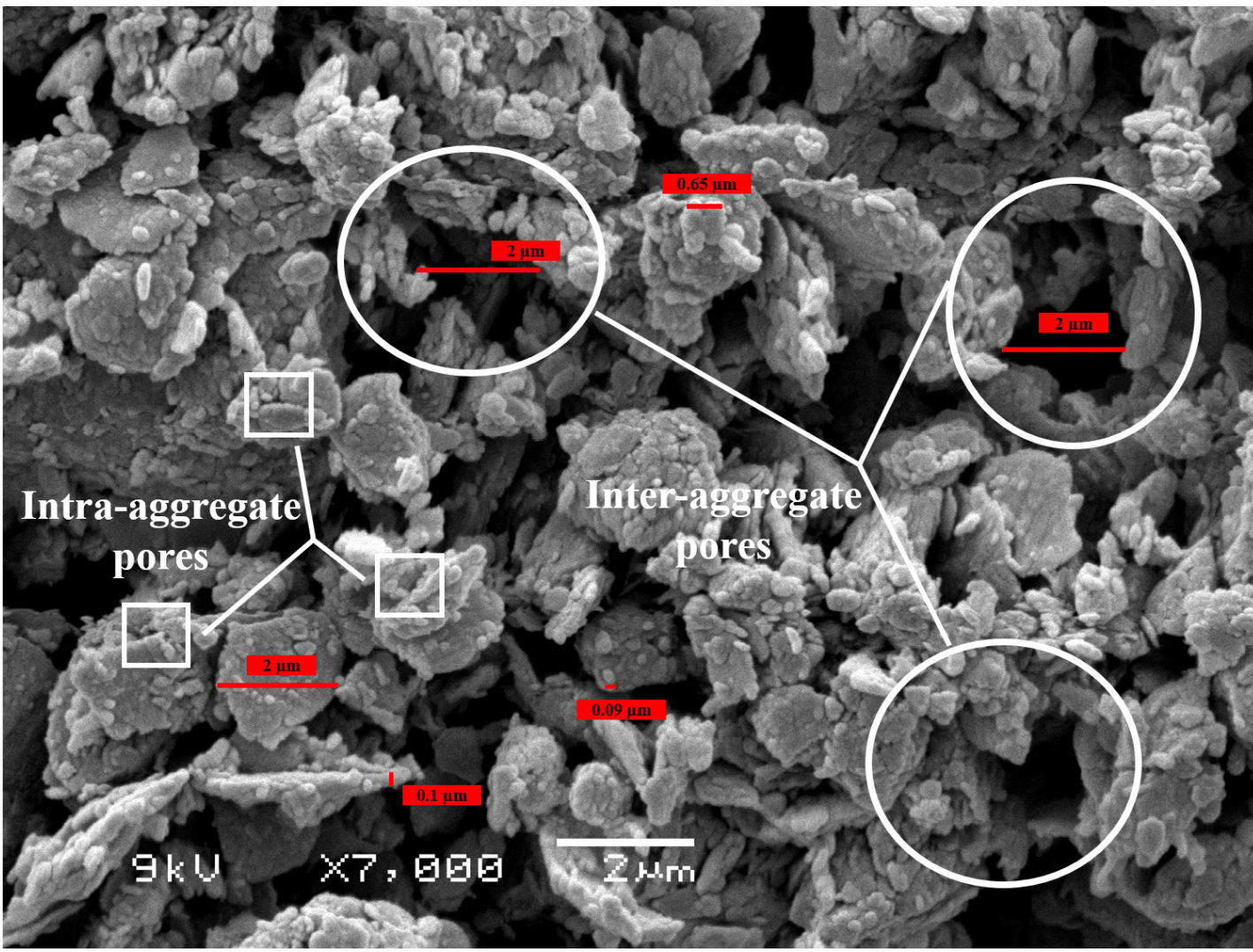
2 µm
0.65 µm
2 µm
Intra-aggregate pores
Inter-aggregate pores
2 µm
0.09 µm
0.1 µm
9kV X7,000 2µm

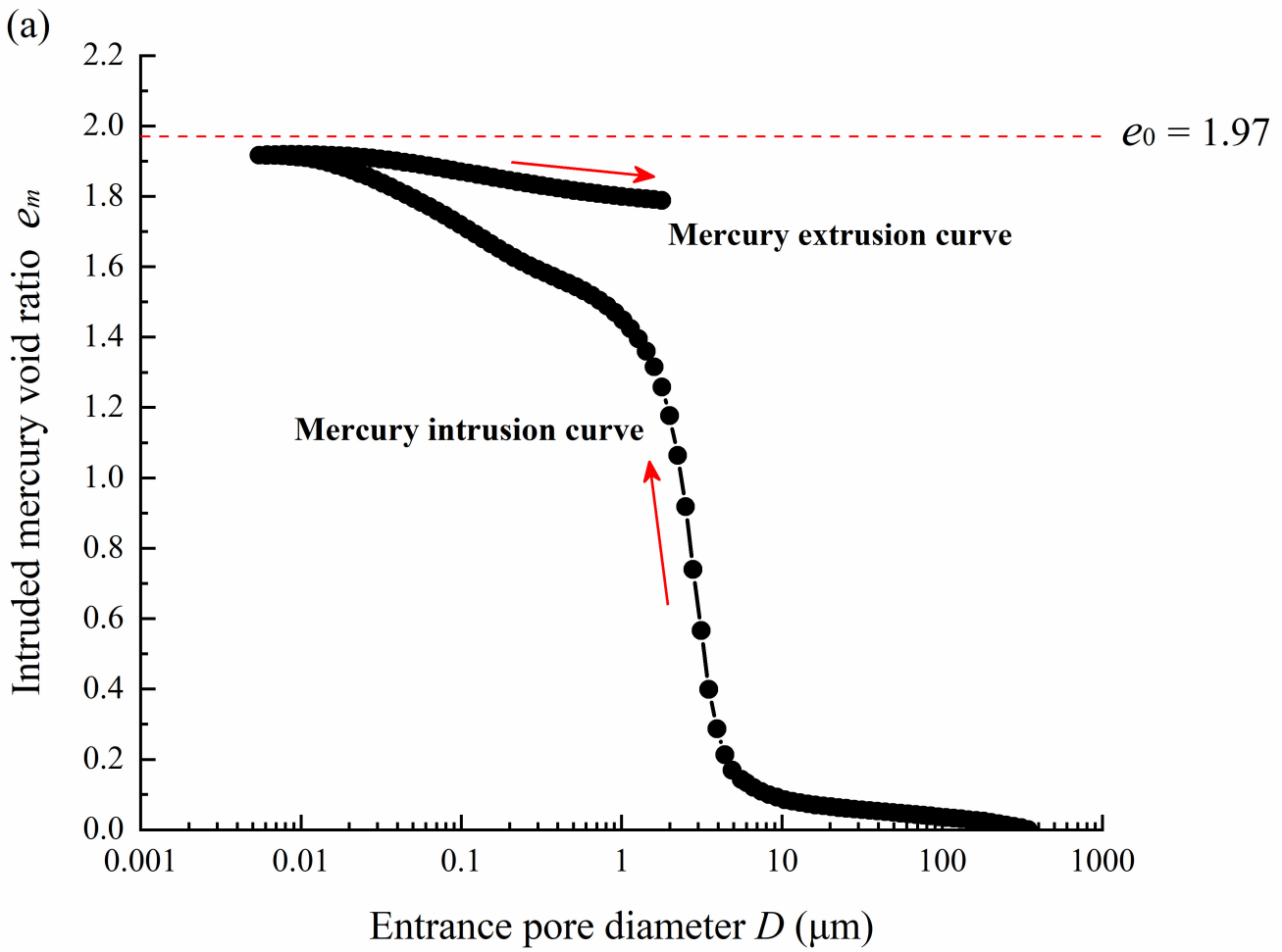
(a)
2.2
2.0
1.8
1.6
1.4
1.2
1.0
0.8
0.6
0.4
0.2
0.0
Intruded mercury void ratio e_m
e_0 = 1.97
Mercury extrusion curve
Mercury intrusion curve
0.001
0.01
0.1
1
10
100
1000
Entrance pore diameter D (μm)

(b)

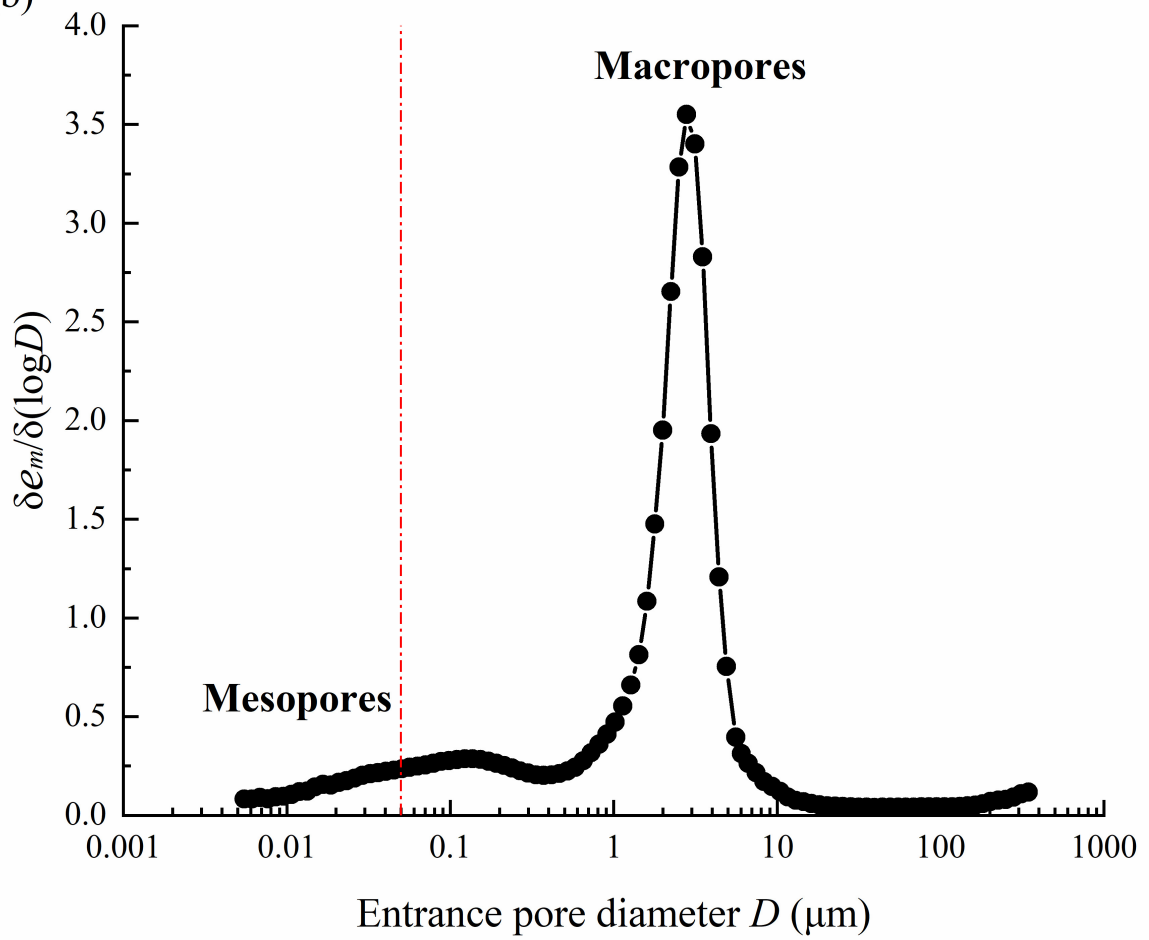
Macropores
Mesopores
4.0
3.5
3.0
2.5
2.0
1.5
1.0
0.5
0.0
δe_m/δ(logD)
0.001
0.01
0.1
1
10
100
1000
Entrance pore diameter D (μm)

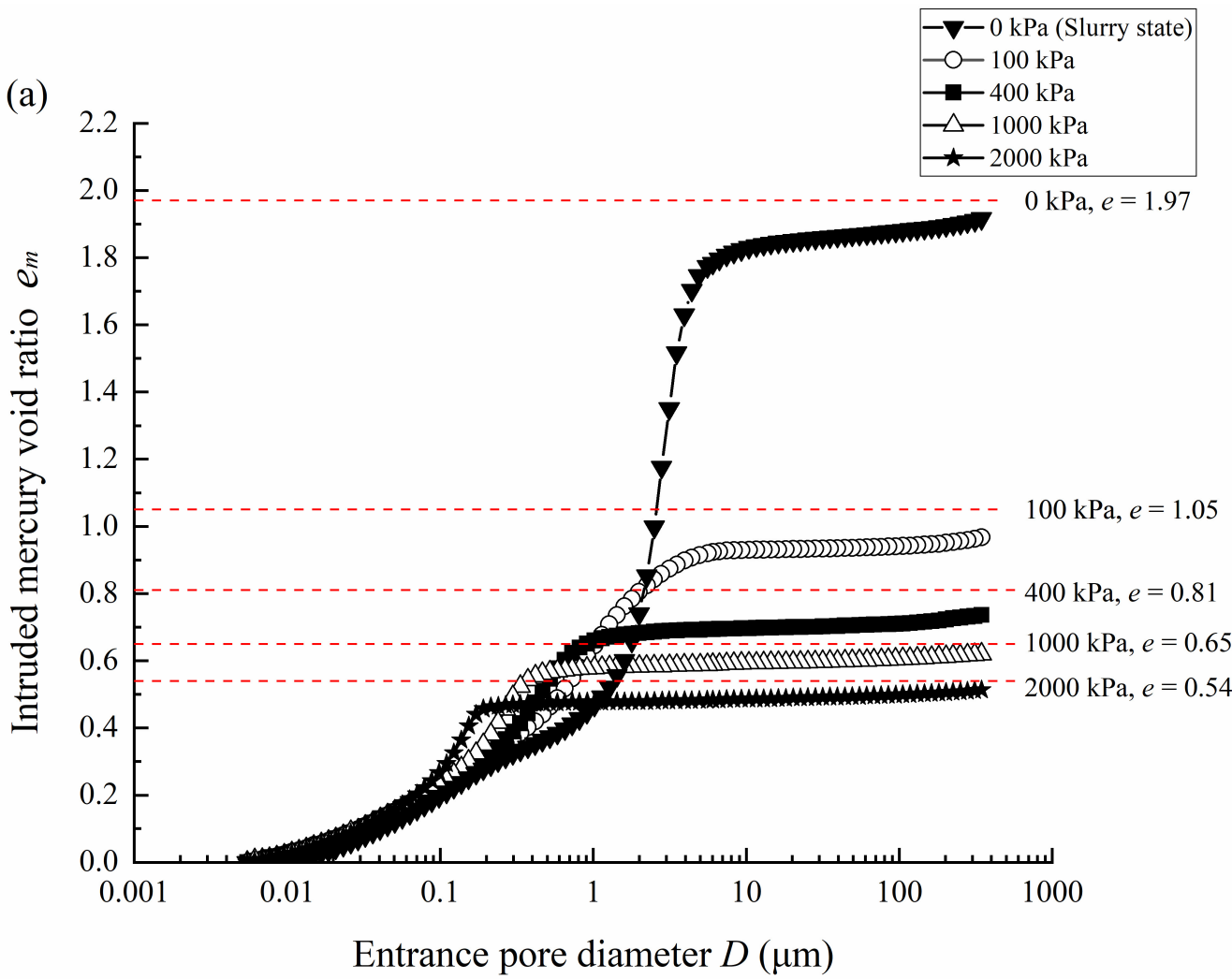
(a)
0 kPa (Slurry state)
100 kPa
400 kPa
1000 kPa
2000 kPa
0 kPa, e = 1.97
100 kPa, e = 1.05
400 kPa, e = 0.81
1000 kPa, e = 0.65
2000 kPa, e = 0.54
Intruded mercury void ratio e_m
Entrance pore diameter D (μm)
2.2
2.0
1.8
1.6
1.4
1.2
1.0
0.8
0.6
0.4
0.2
0.0
0.001
0.01
0.1
1
10
100
1000

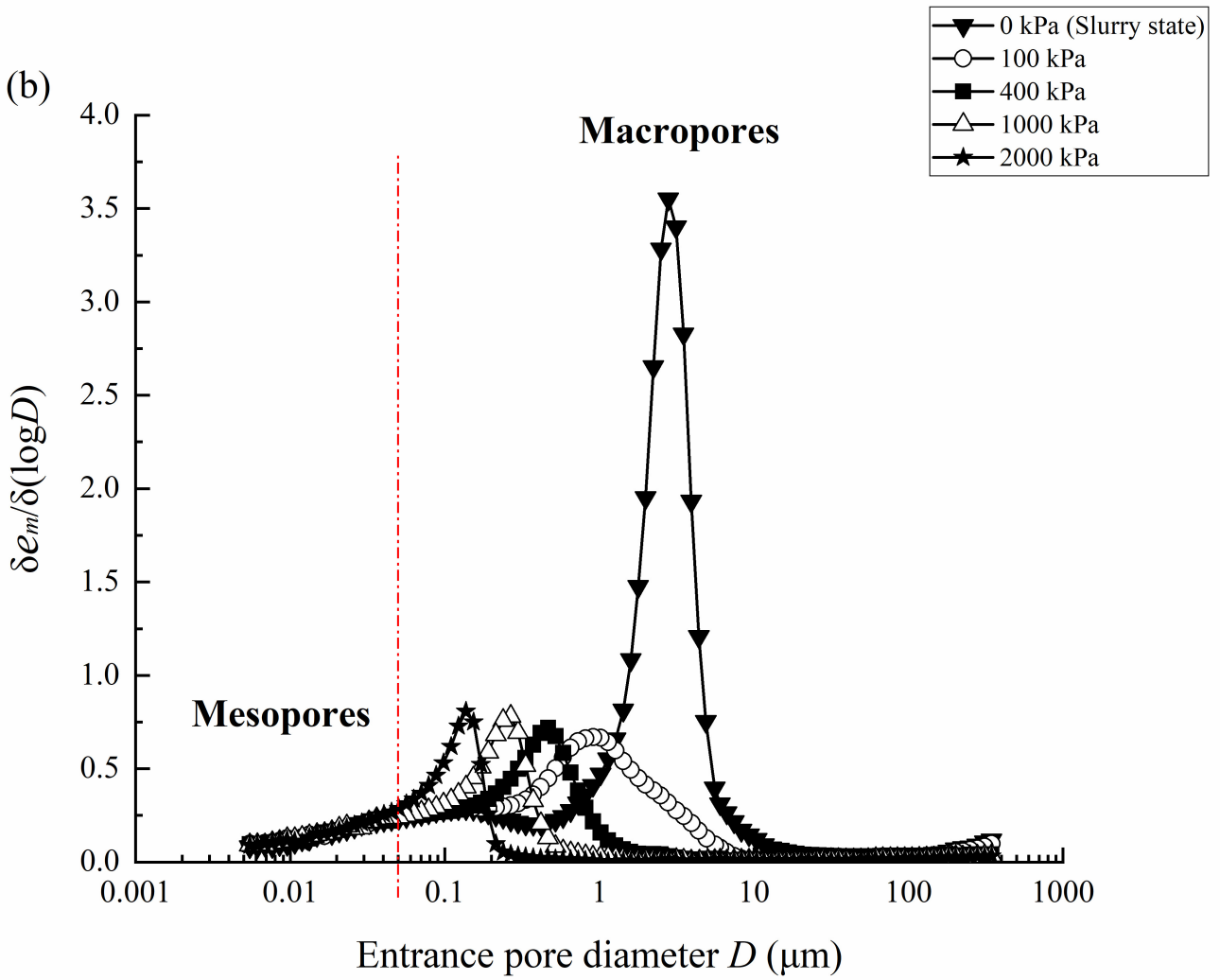
(b)
0 kPa (Slurry state)
100 kPa
400 kPa
1000 kPa
2000 kPa
Macropores
Mesopores
4.0
3.5
3.0
2.5
2.0
1.5
1.0
0.5
0.0
0.001
0.01
0.1
1
10
100
1000
δe_m/δ(logD)
Entrance pore diameter D (μm)

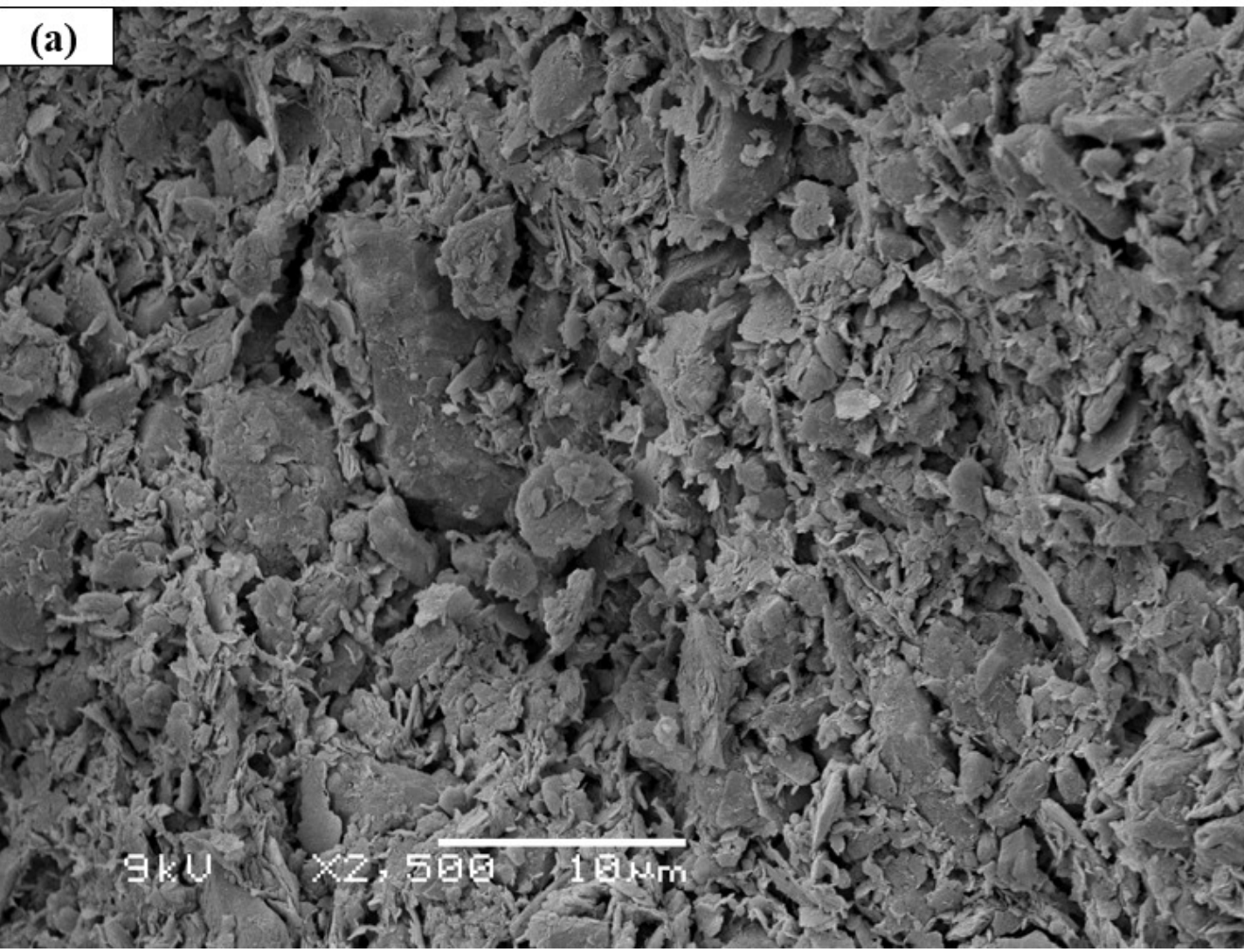
(a)
9kV X2,500 10μm

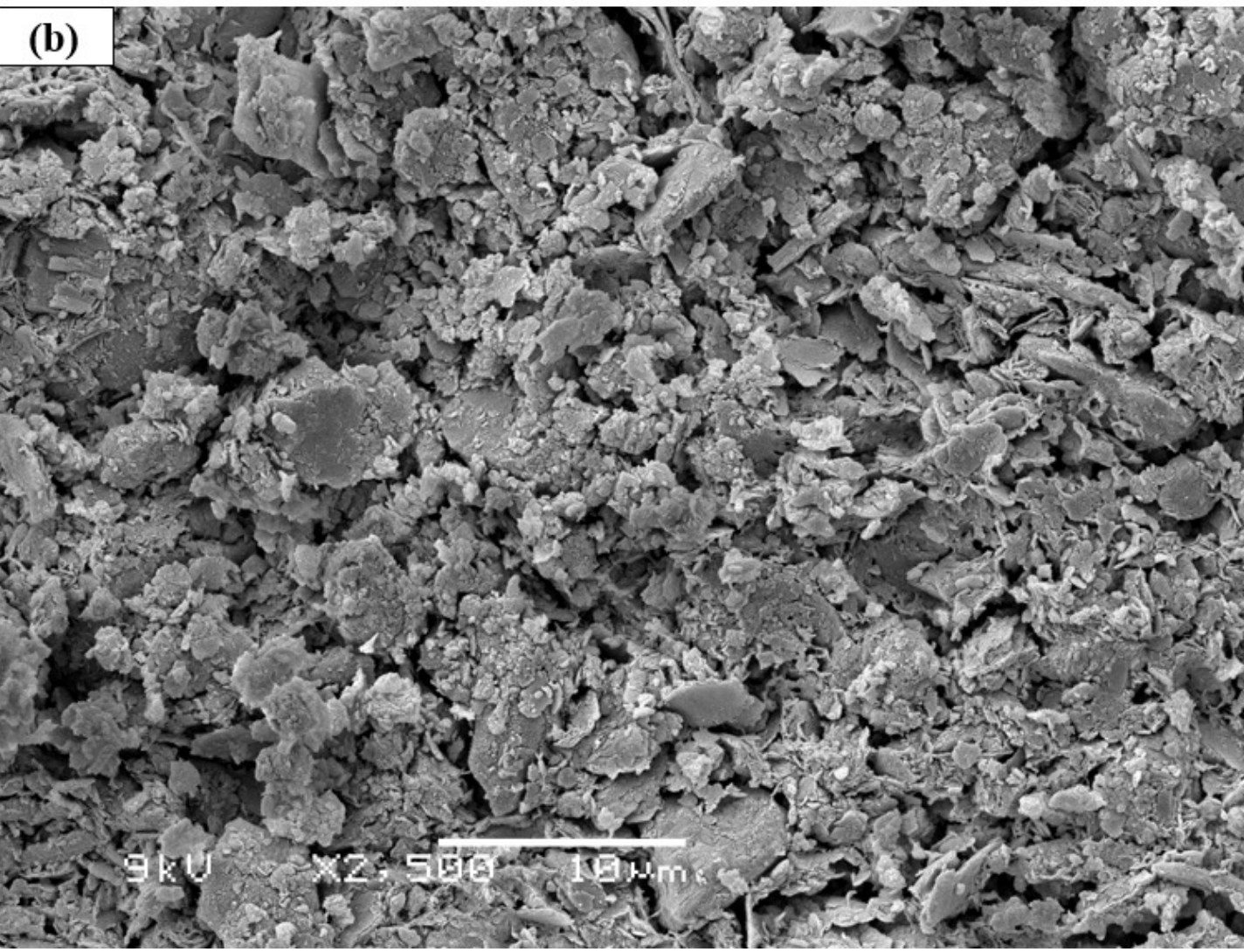
(b)
9kU X2,500 10μm

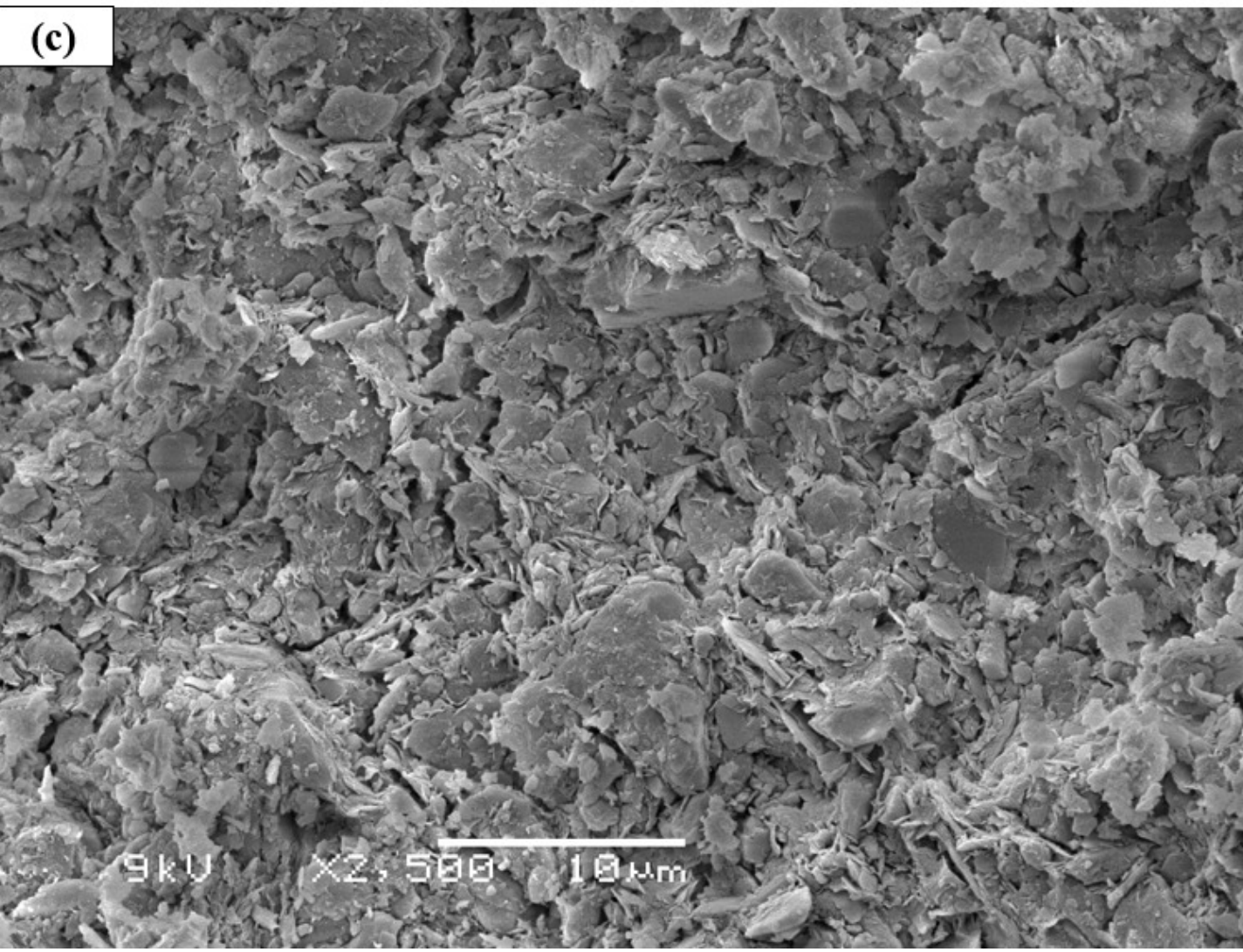
(c)
9kV X2,500 10μm

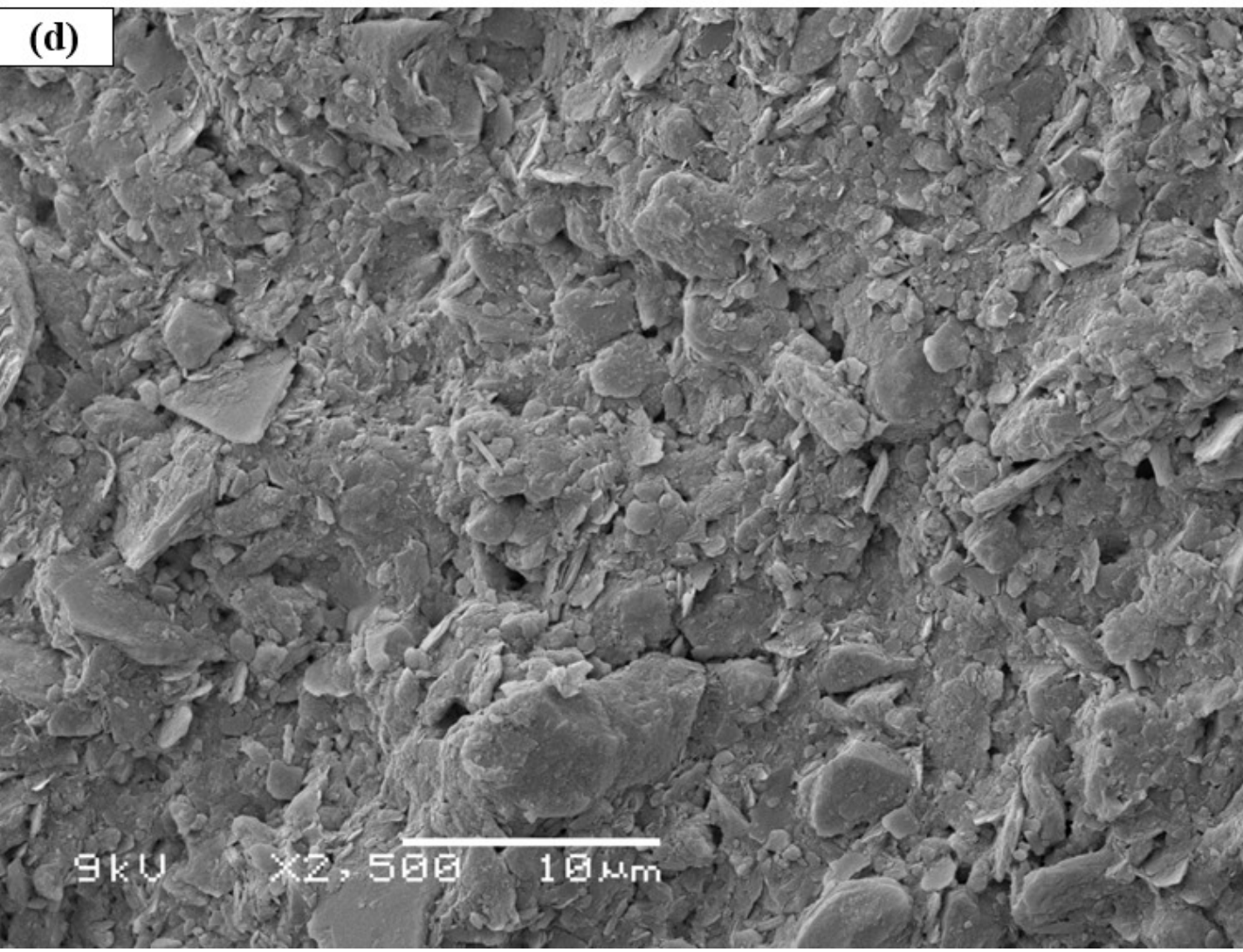
(d)
9kV X2,500 10µm

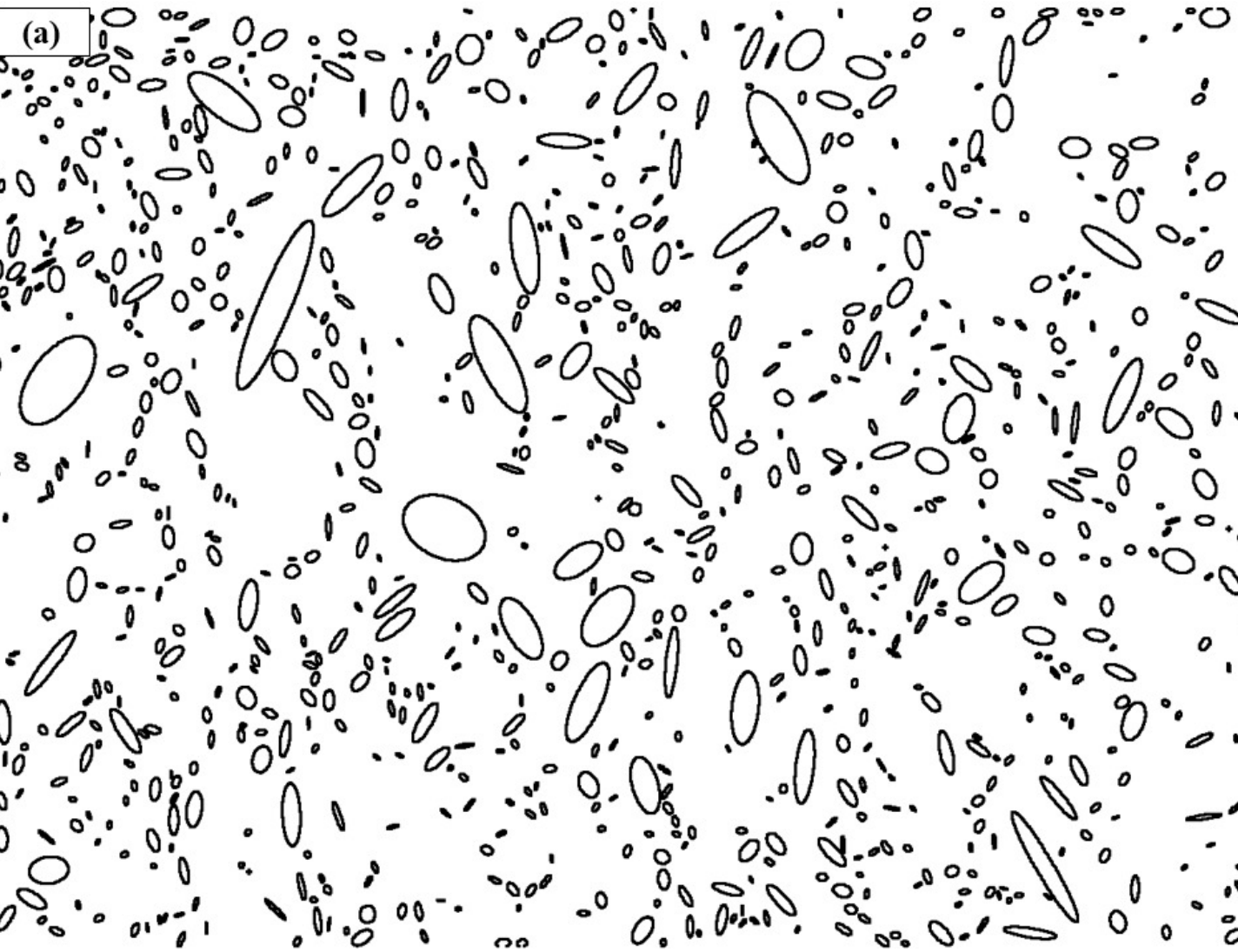
(a)

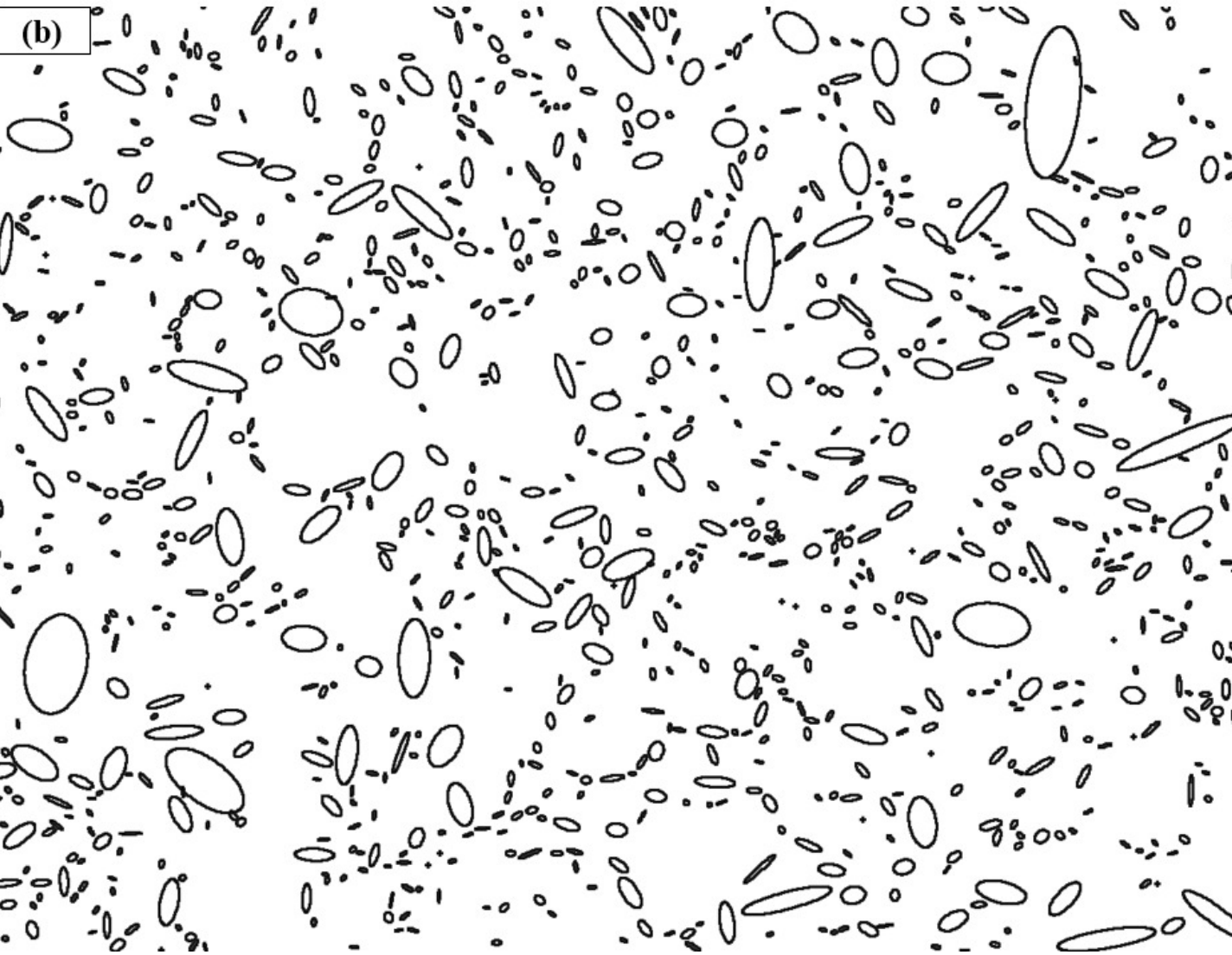
(b)


(c)

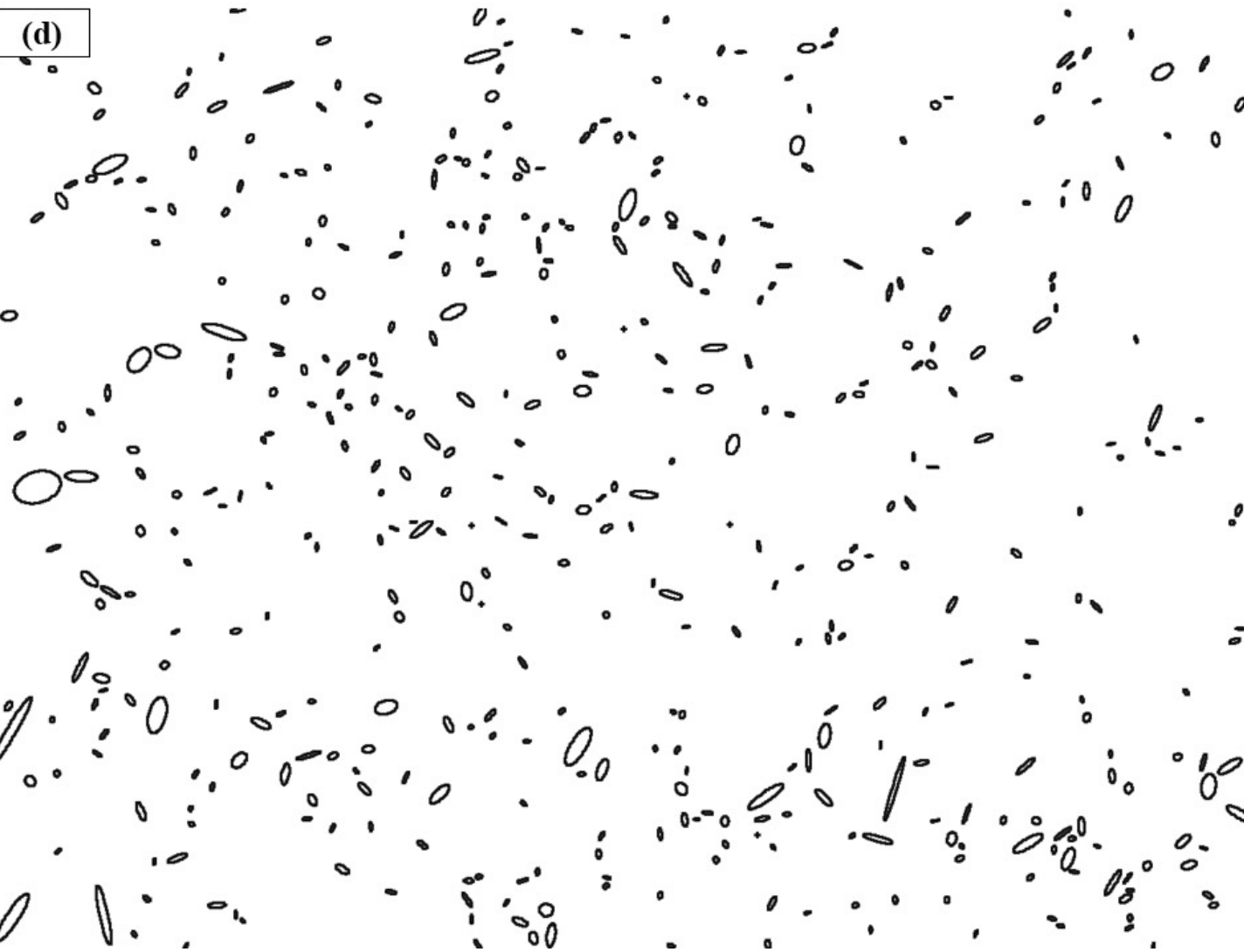
(d)

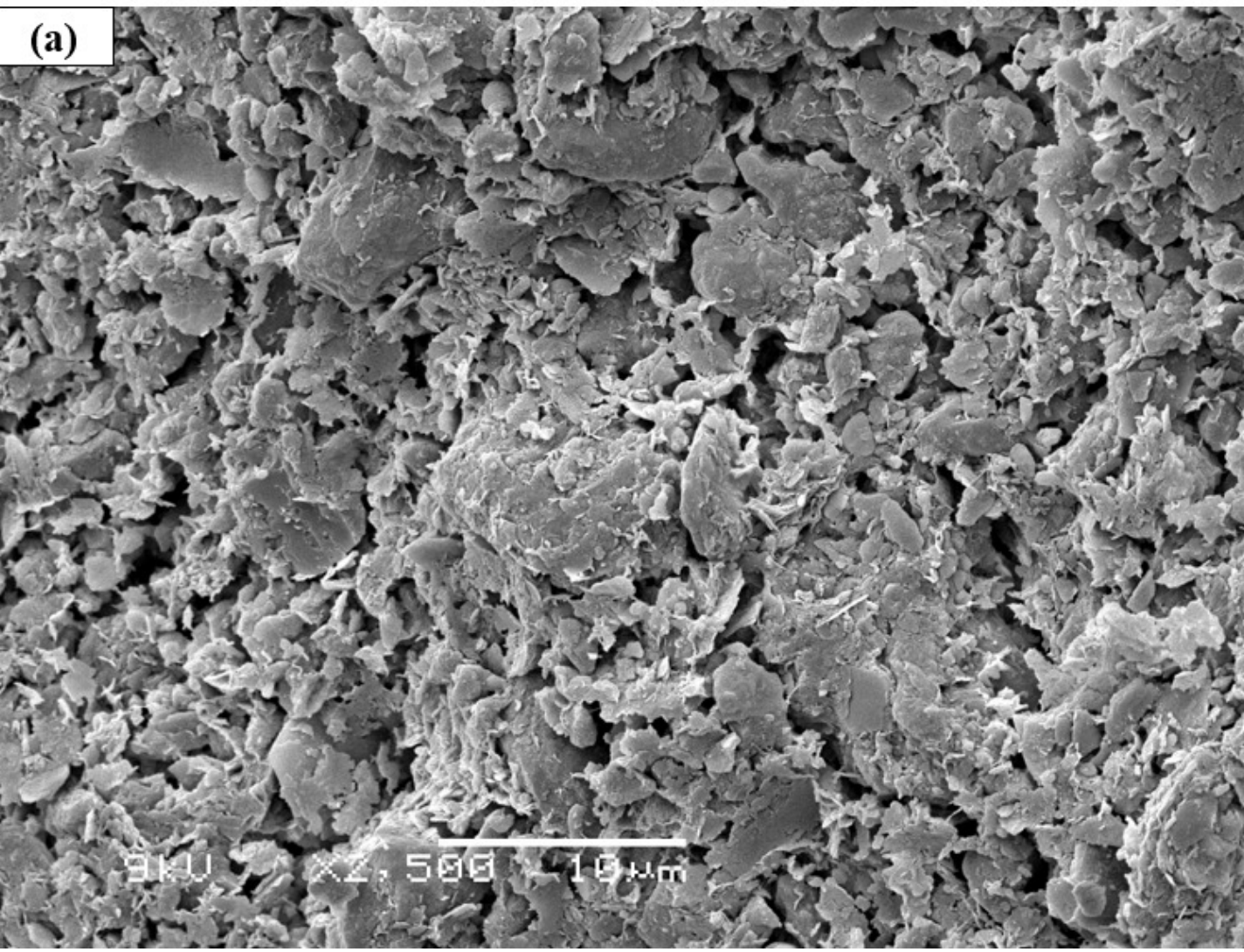
(a)
9kV X2,500 10μm

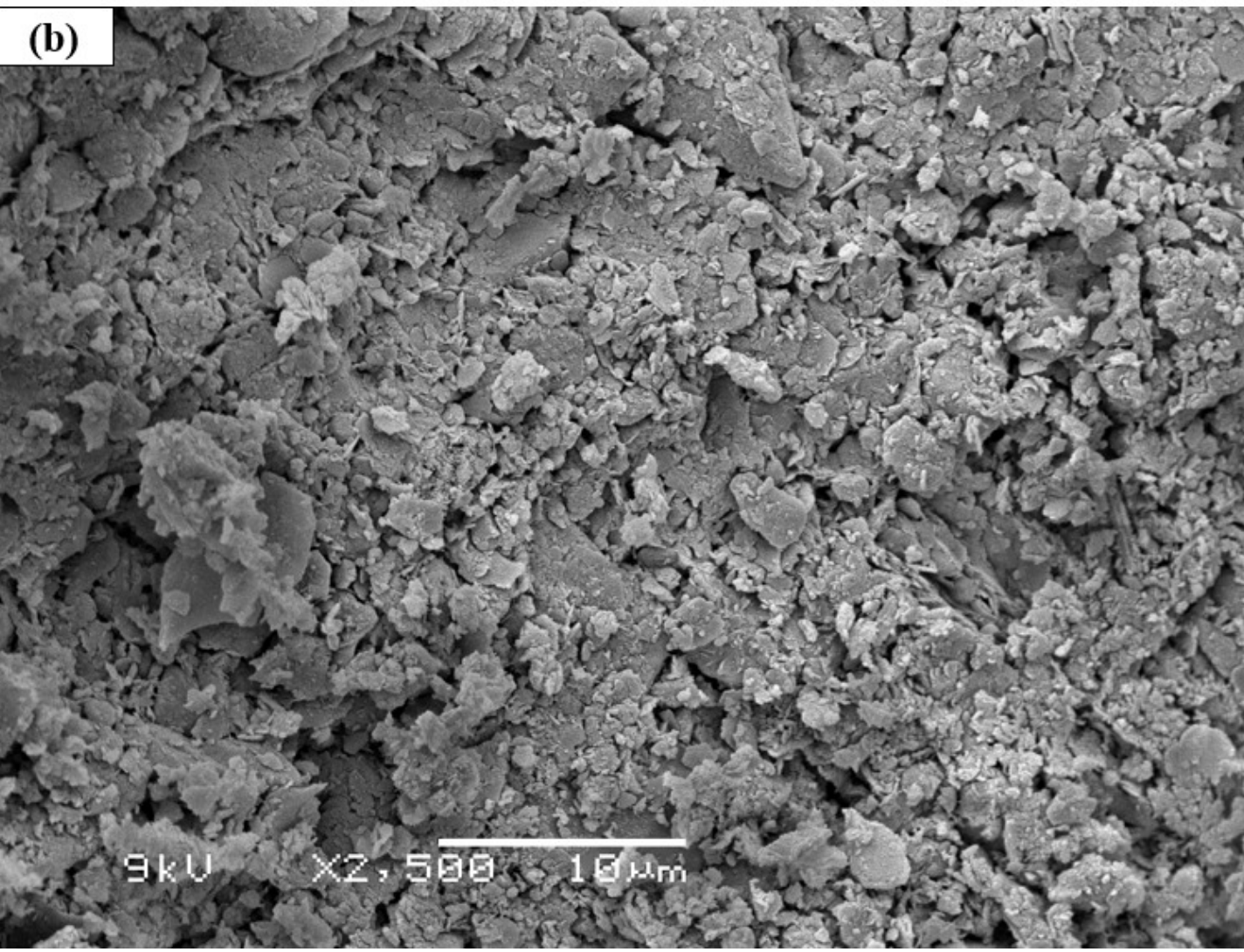
(b)
9kV X2,500 10µm

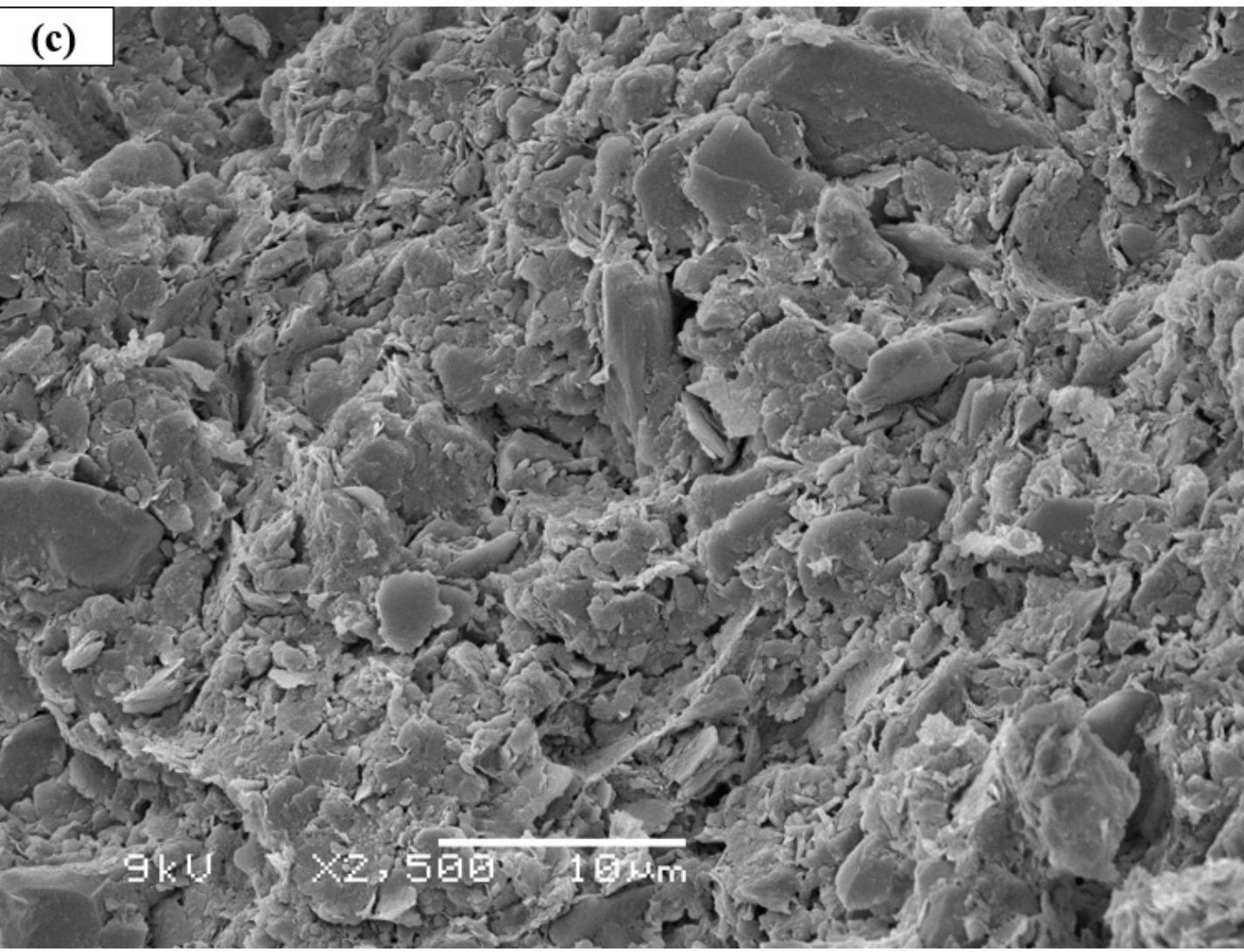
(c)
9kV X2,500 10µm

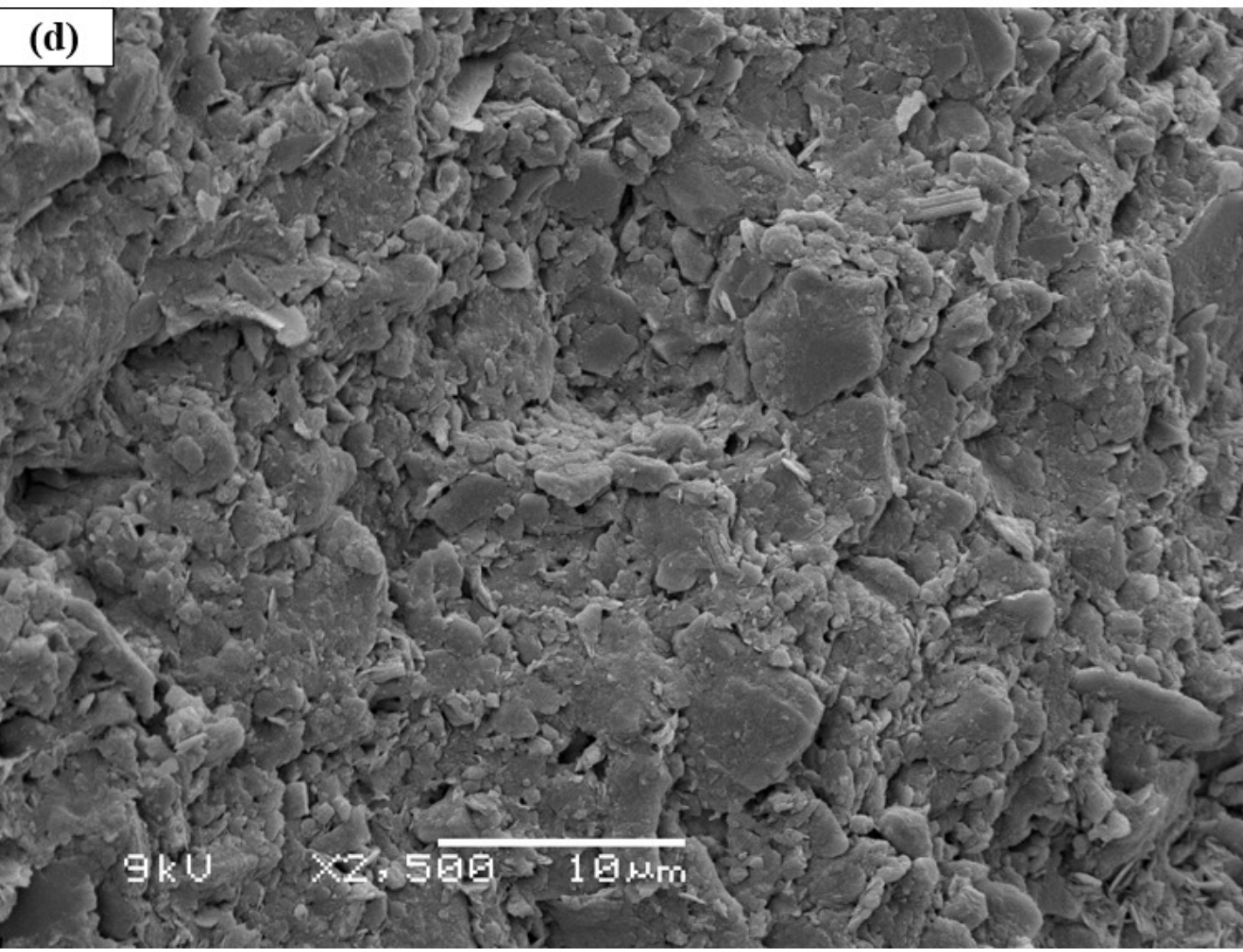
(d)
9kV X2,500 10µm

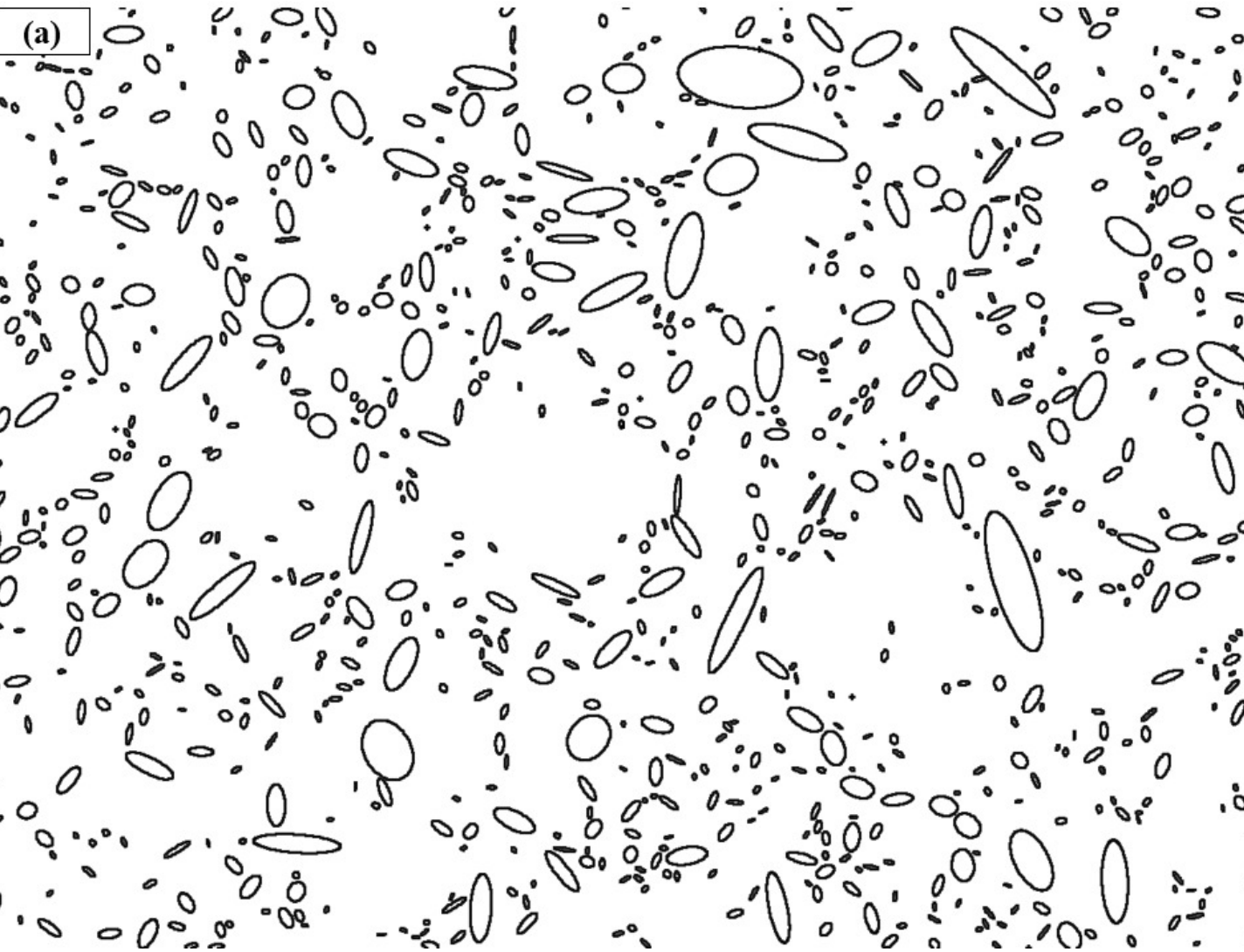
(a)

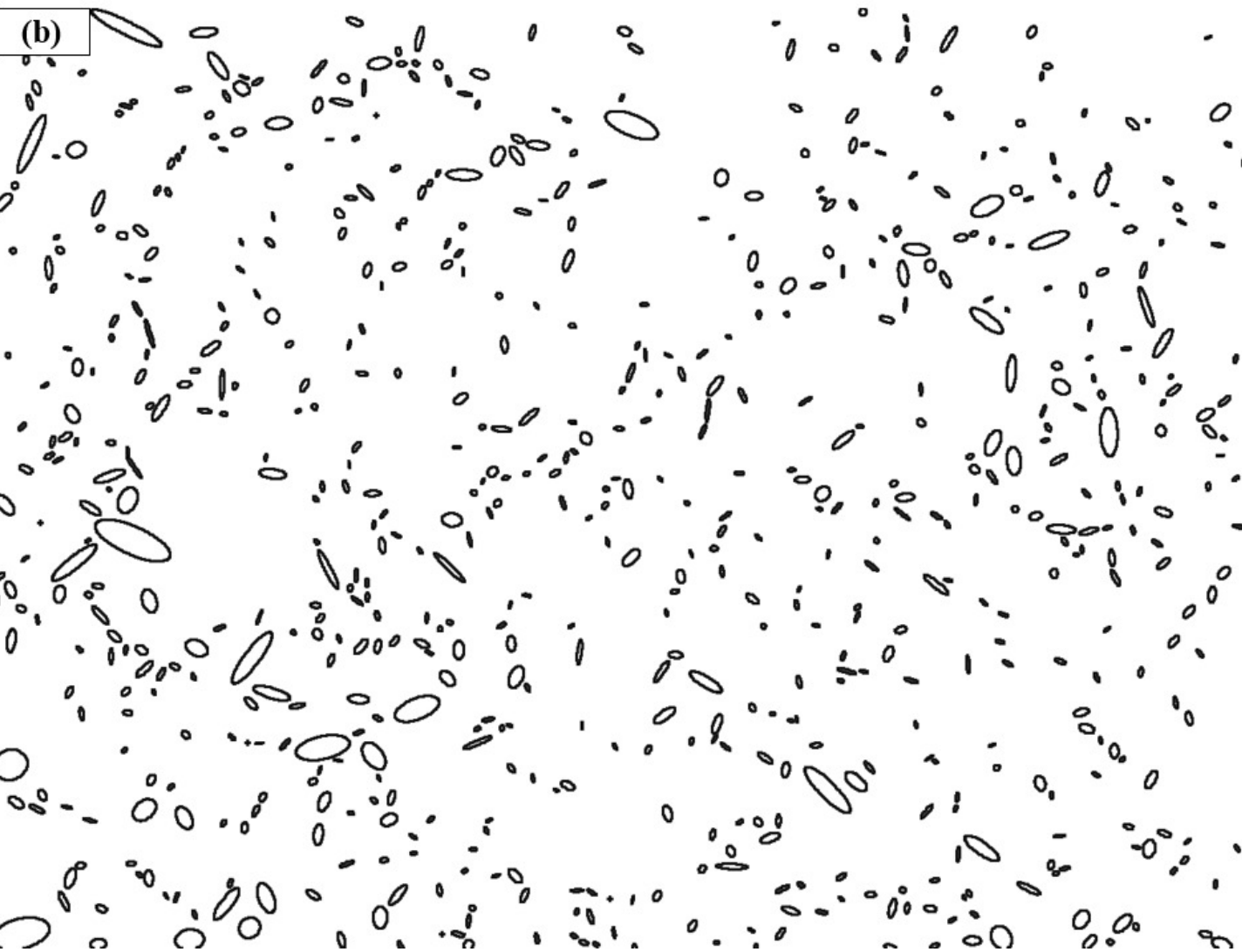
(b)


(c)


(d)

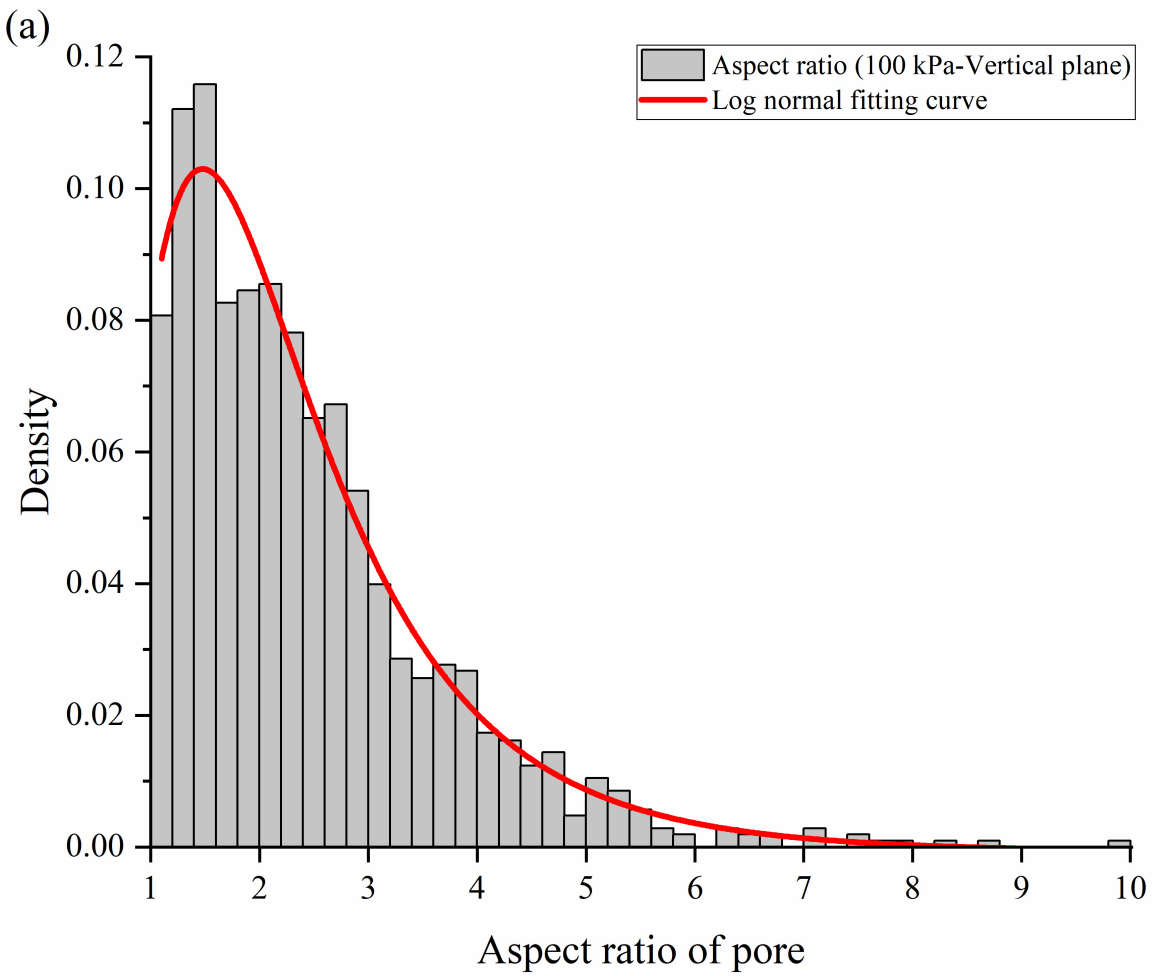
(a)
Aspect ratio (100 kPa-Vertical plane)
Log normal fitting curve
Density
0.12
0.10
0.08
0.06
0.04
0.02
0.00
1
2
3
4
5
6
7
8
9
10
Aspect ratio of pore

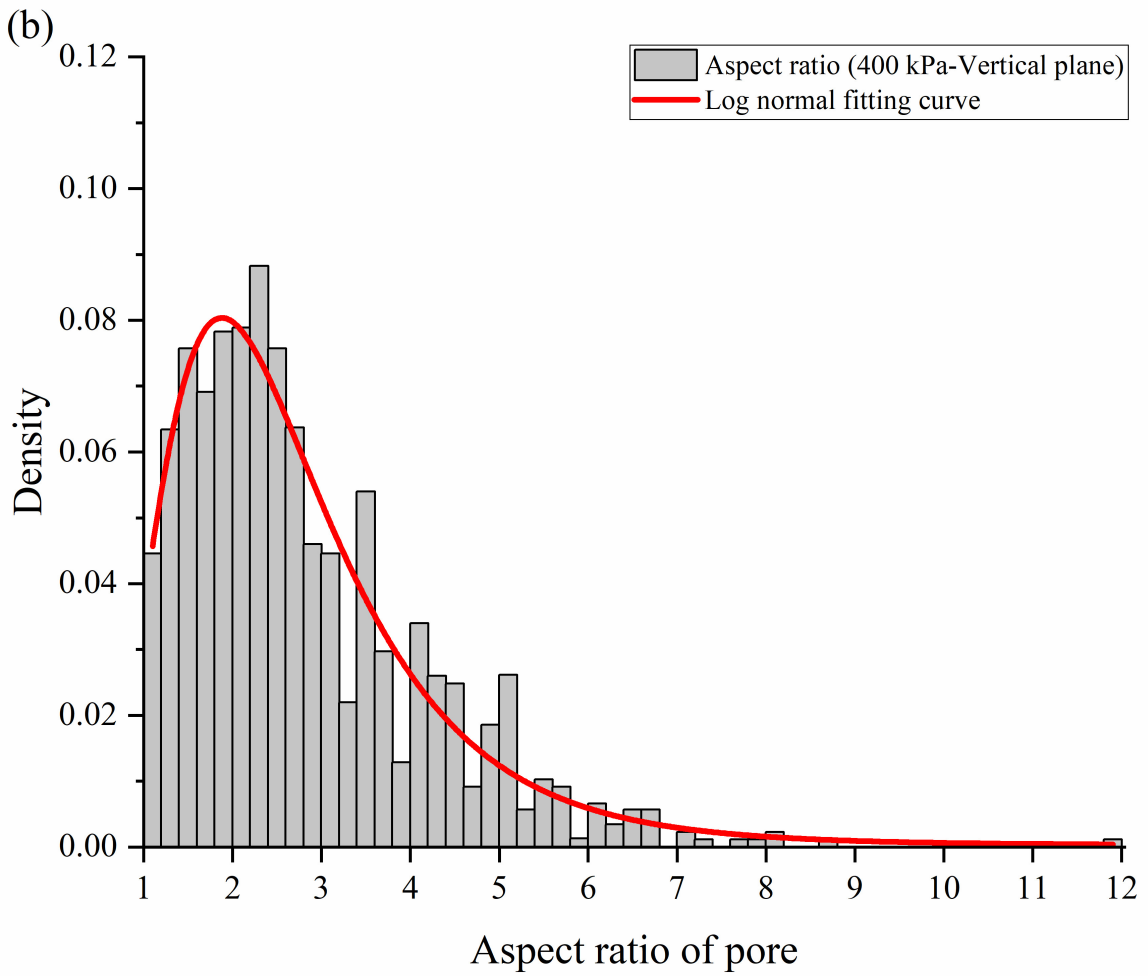
(b)
Aspect ratio (400 kPa-Vertical plane)
Log normal fitting curve
Density
0.12
0.10
0.08
0.06
0.04
0.02
0.00
1
2
3
4
5
6
7
8
9
10
11
12
Aspect ratio of pore

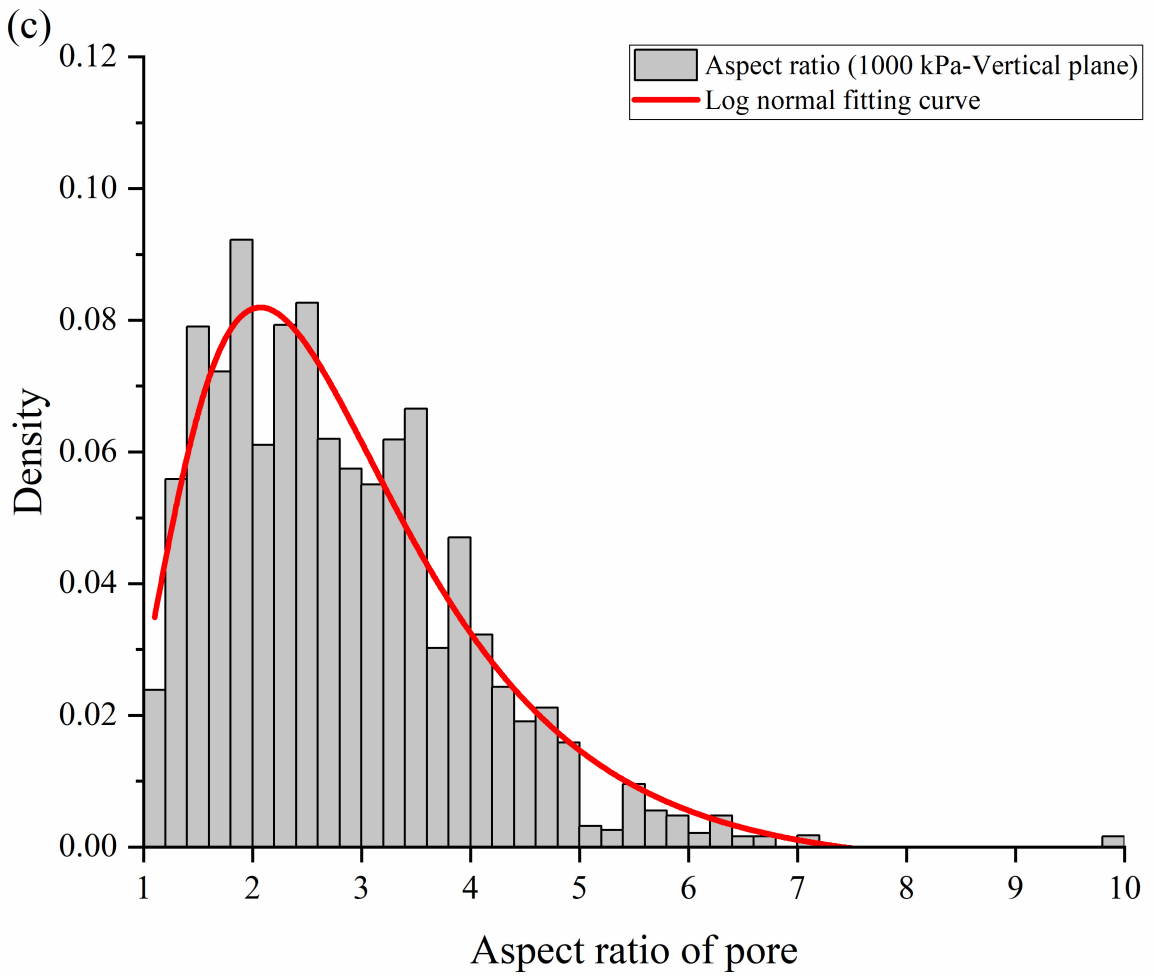
(c)
Aspect ratio (1000 kPa-Vertical plane)
Log normal fitting curve
Density
0.12
0.10
0.08
0.06
0.04
0.02
0.00
1
2
3
4
5
6
7
8
9
10
Aspect ratio of pore

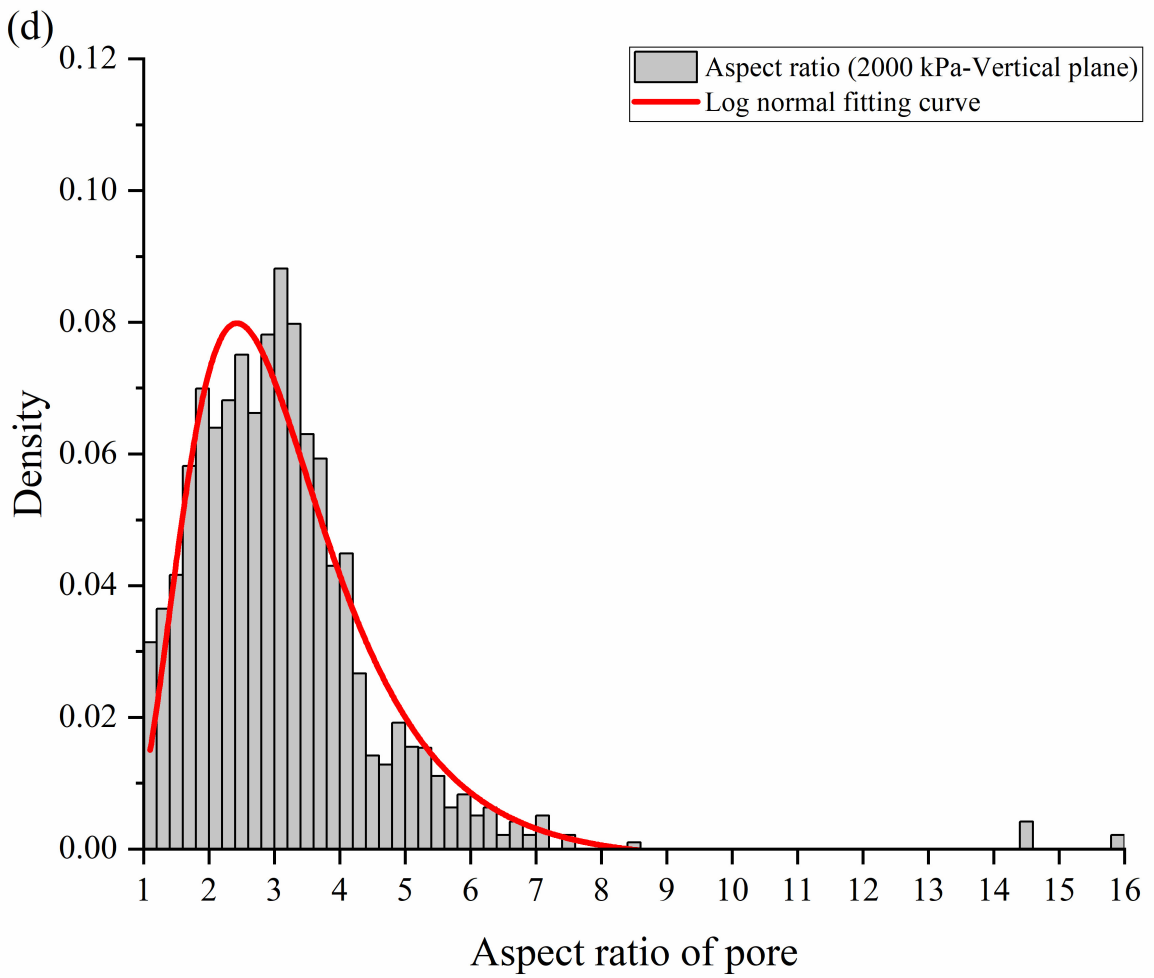
(d)
Aspect ratio (2000 kPa-Vertical plane)
Log normal fitting curve
Density
0.12
0.10
0.08
0.06
0.04
0.02
0.00
1
2
3
4
5
6
7
8
9
10
11
12
13
14
15
16
Aspect ratio of pore

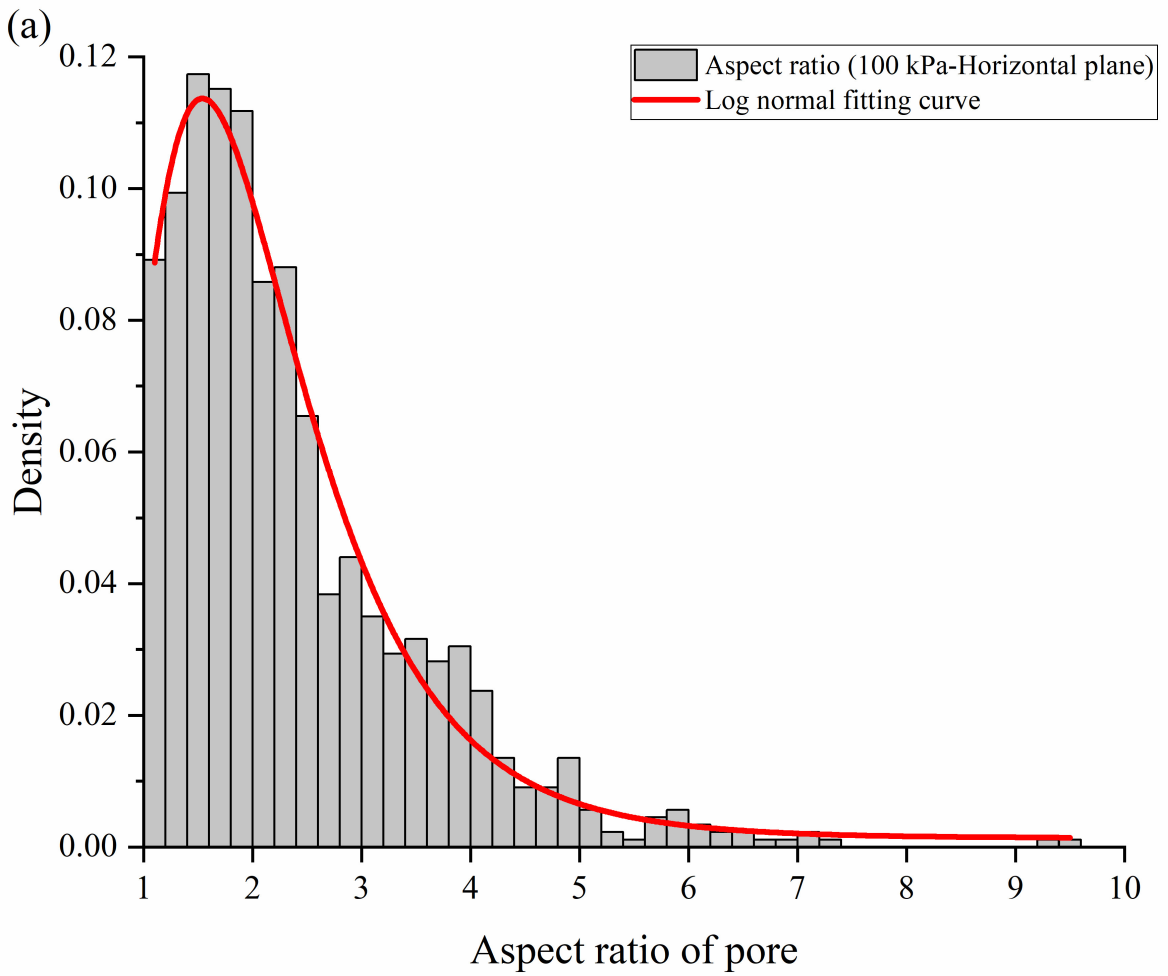
(a)
Aspect ratio (100 kPa-Horizontal plane)
Log normal fitting curve
Density
0.12
0.10
0.08
0.06
0.04
0.02
0.00
1
2
3
4
5
6
7
8
9
10
Aspect ratio of pore

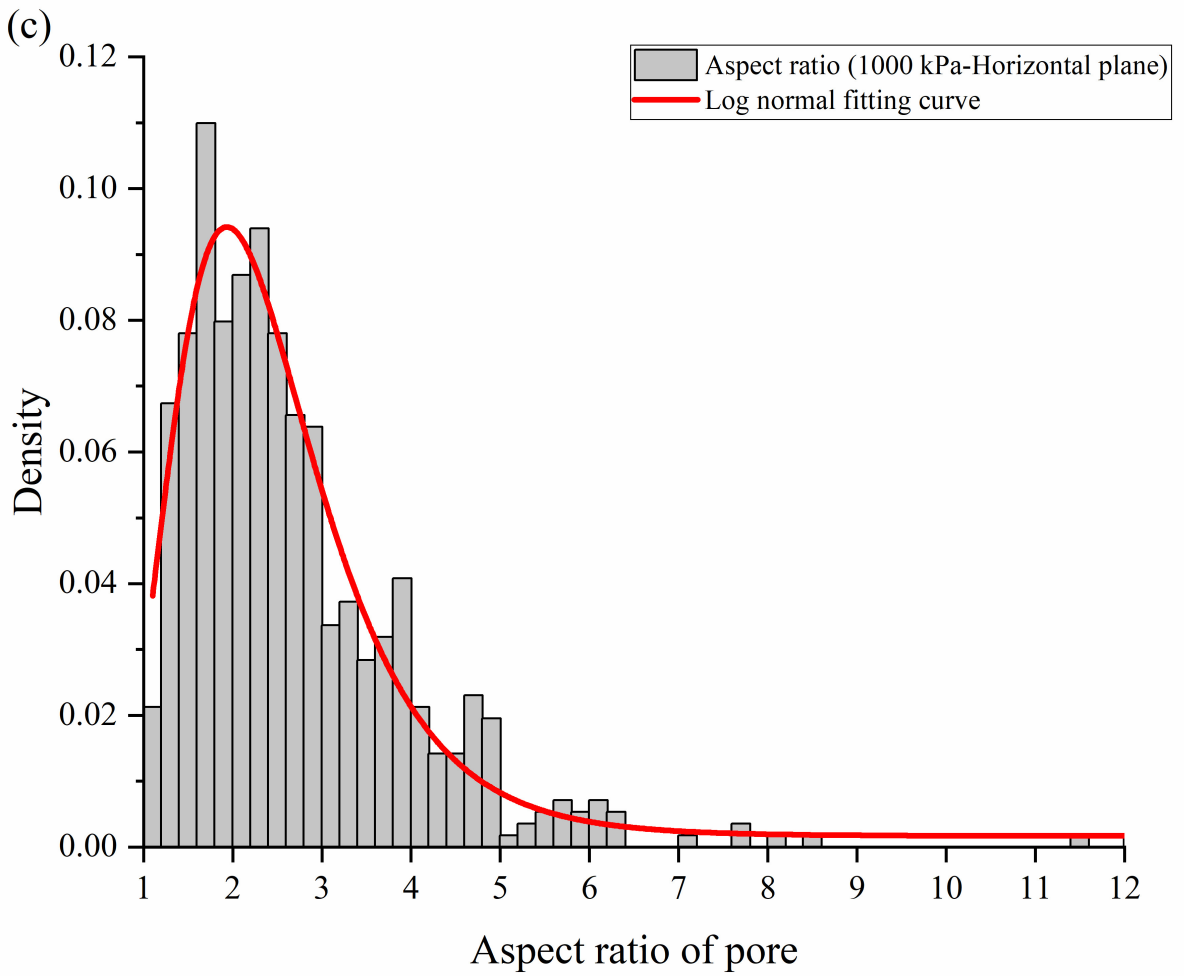
(c)
Aspect ratio (1000 kPa-Horizontal plane)
Log normal fitting curve
Density
0.12
0.10
0.08
0.06
0.04
0.02
0.00
1
2
3
4
5
6
7
8
9
10
11
12
Aspect ratio of pore

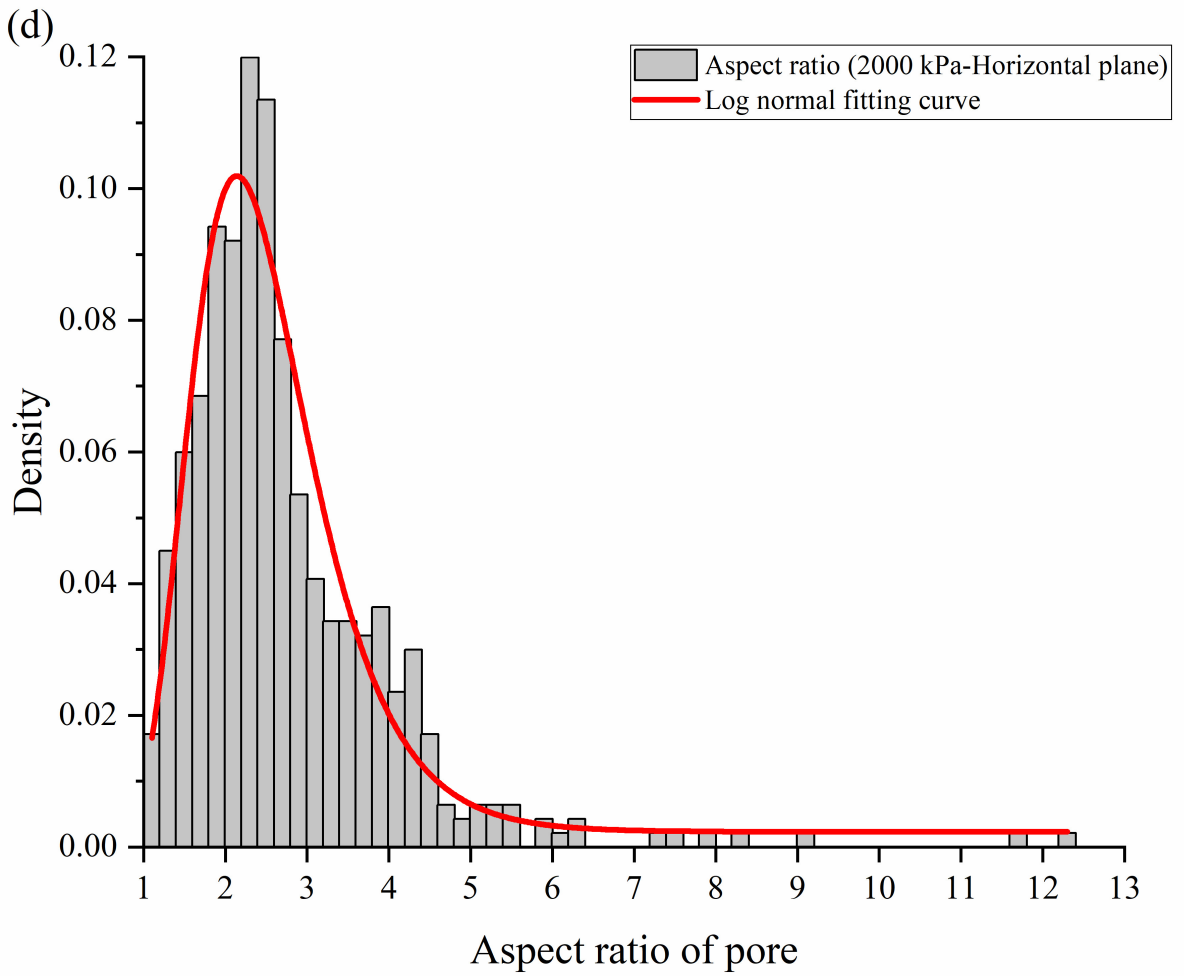
(d)
Aspect ratio (2000 kPa-Horizontal plane)
Log normal fitting curve
Density
0.12
0.10
0.08
0.06
0.04
0.02
0.00
1
2
3
4
5
6
7
8
9
10
11
12
13
Aspect ratio of pore

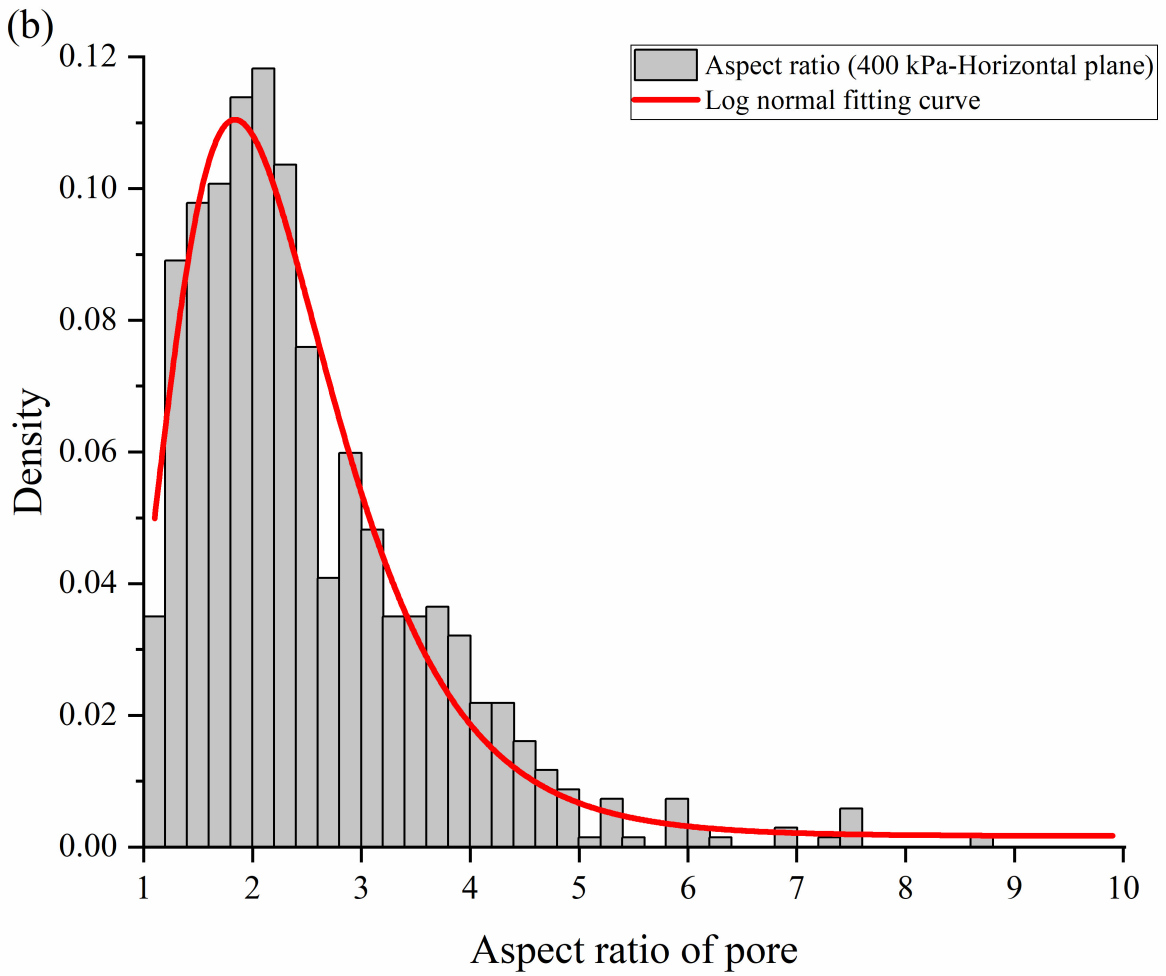
(b)
Aspect ratio (400 kPa-Horizontal plane)
Log normal fitting curve
Density
0.12
0.10
0.08
0.06
0.04
0.02
0.00
1
2
3
4
5
6
7
8
9
10
Aspect ratio of pore

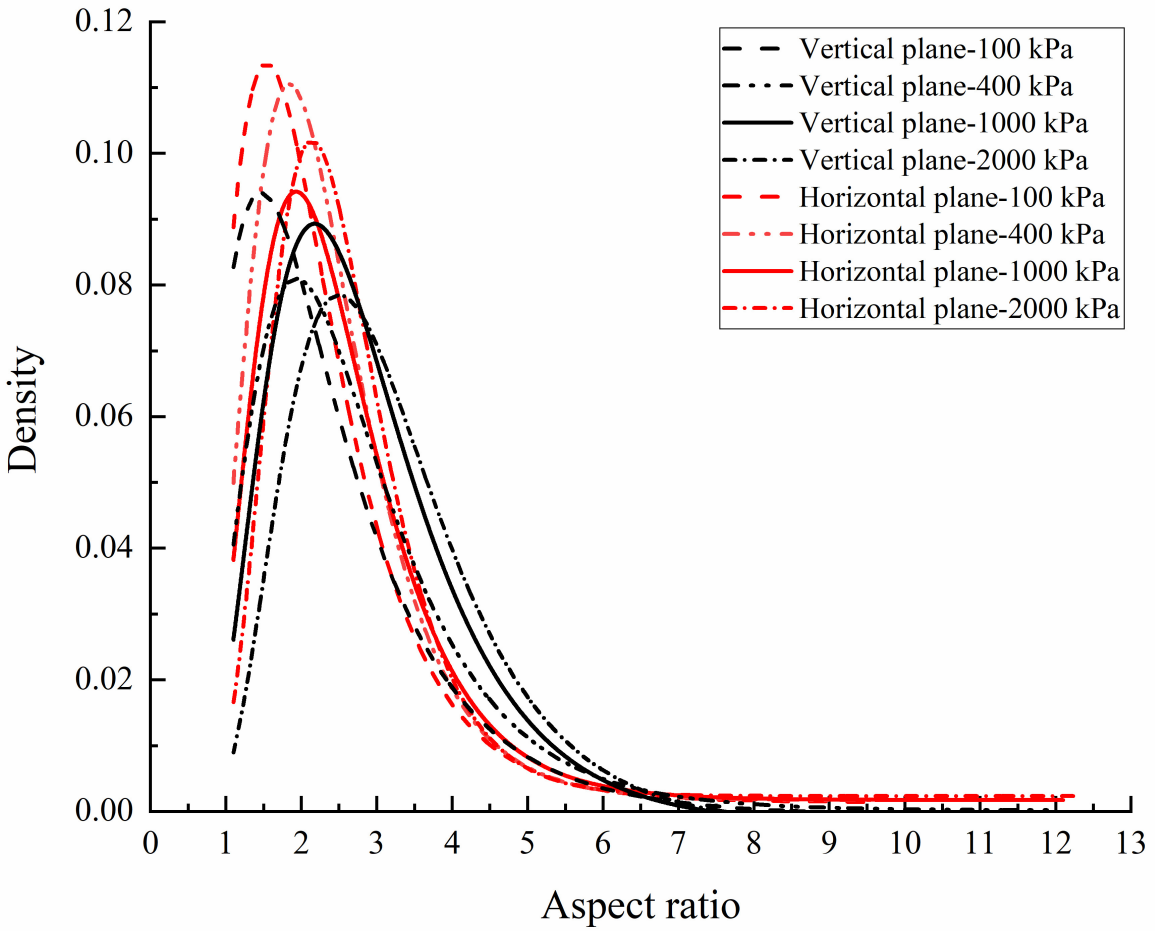
Vertical plane-100 kPa
Vertical plane-400 kPa
Vertical plane-1000 kPa
Vertical plane-2000 kPa
Horizontal plane-100 kPa
Horizontal plane-400 kPa
Horizontal plane-1000 kPa
Horizontal plane-2000 kPa
Density
0.12
0.10
0.08
0.06
0.04
0.02
0.00
0
1
2
3
4
5
6
7
8
9
10
11
12
13
Aspect ratio

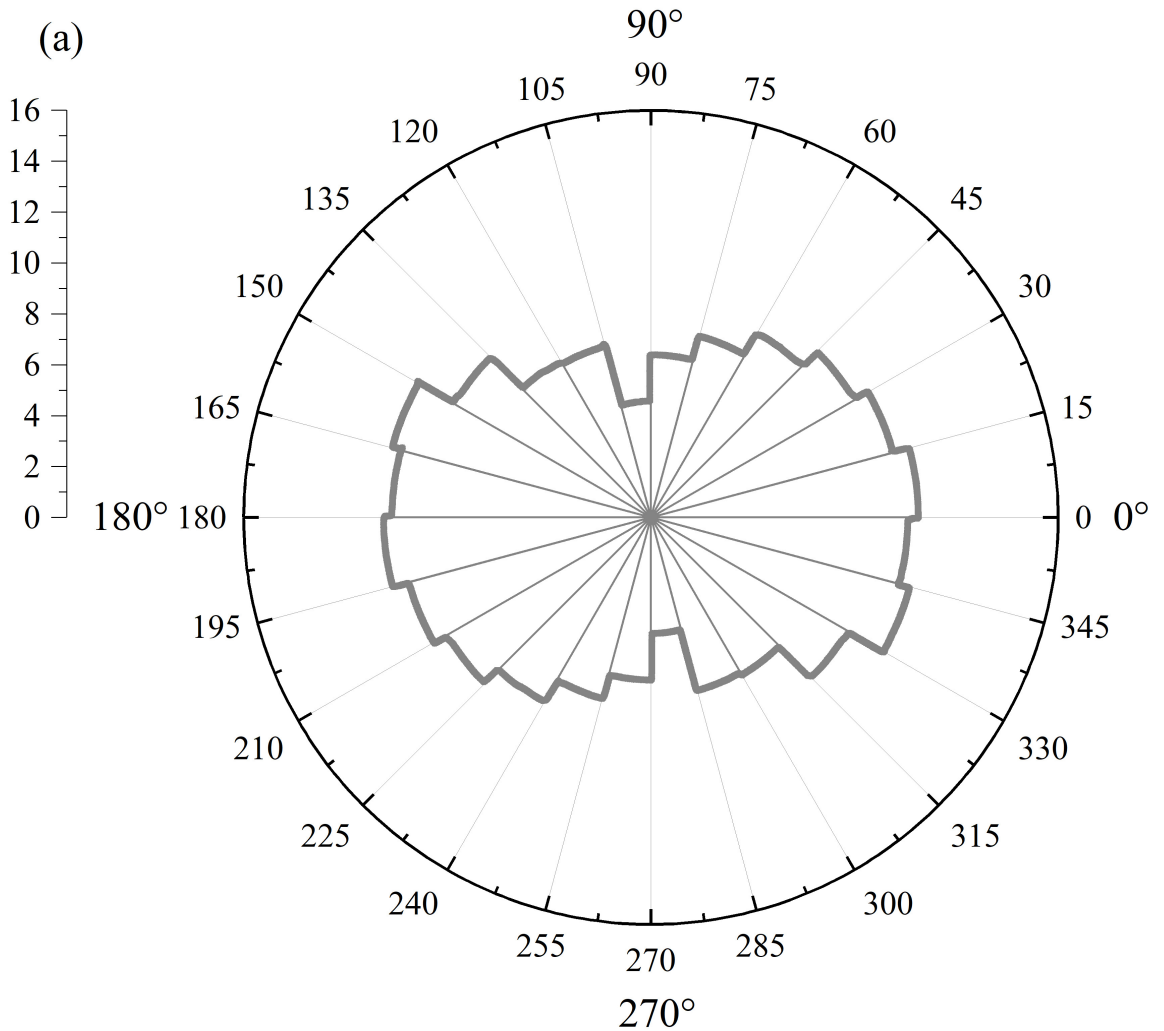
(a)
90°
90
105
75
120
60
135
45
150
30
165
15
180°
180
0
0°
195
345
210
330
225
315
240
300
255
285
270
270°
16
14
12
10
8
6
4
2
0

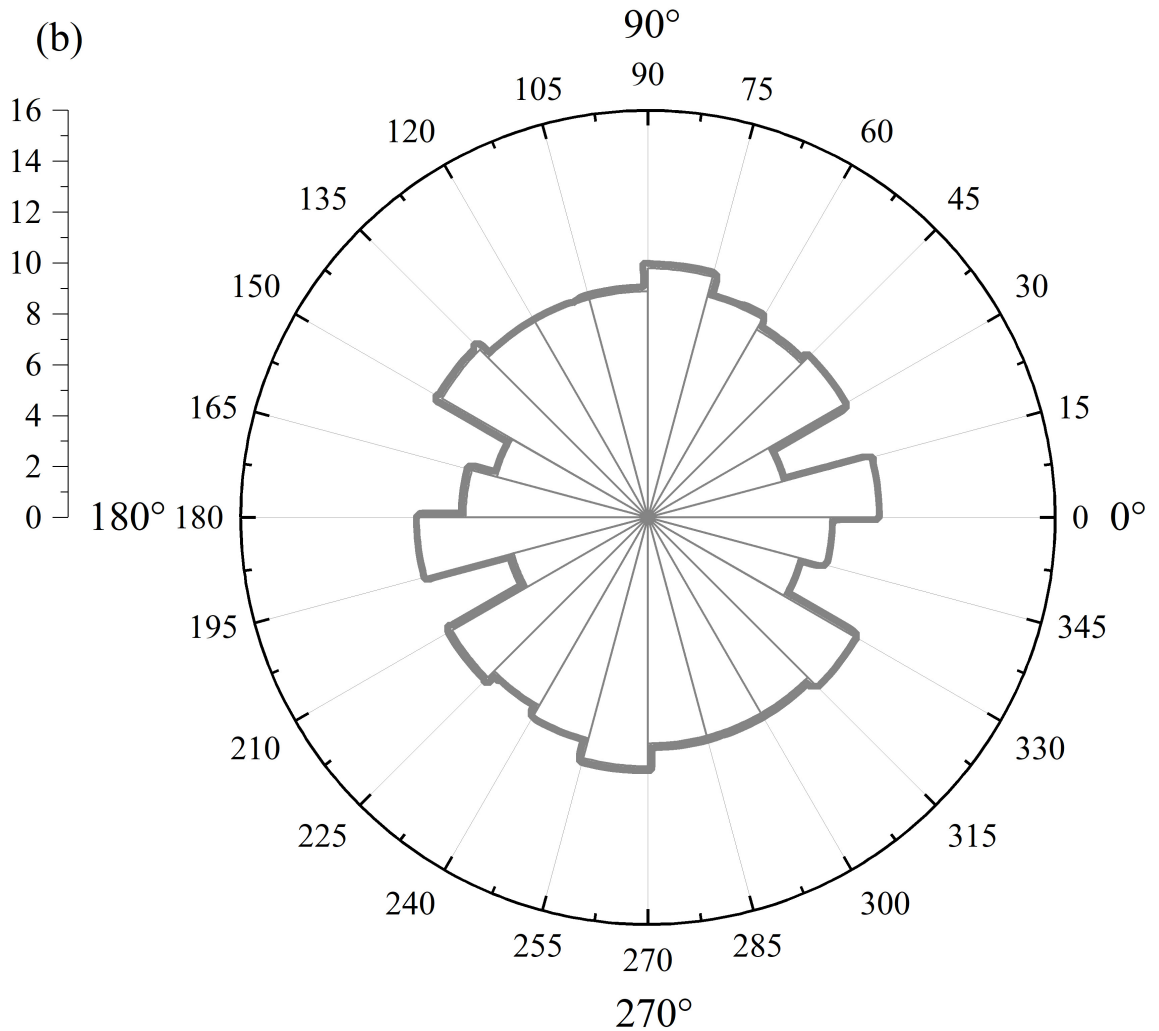
(b)
90°
90
75
60
45
30
15
0
0°
345
330
315
300
285
270
270°
255
240
225
210
195
180
180°
165
150
135
120
105
16
14
12
10
8
6
4
2
0

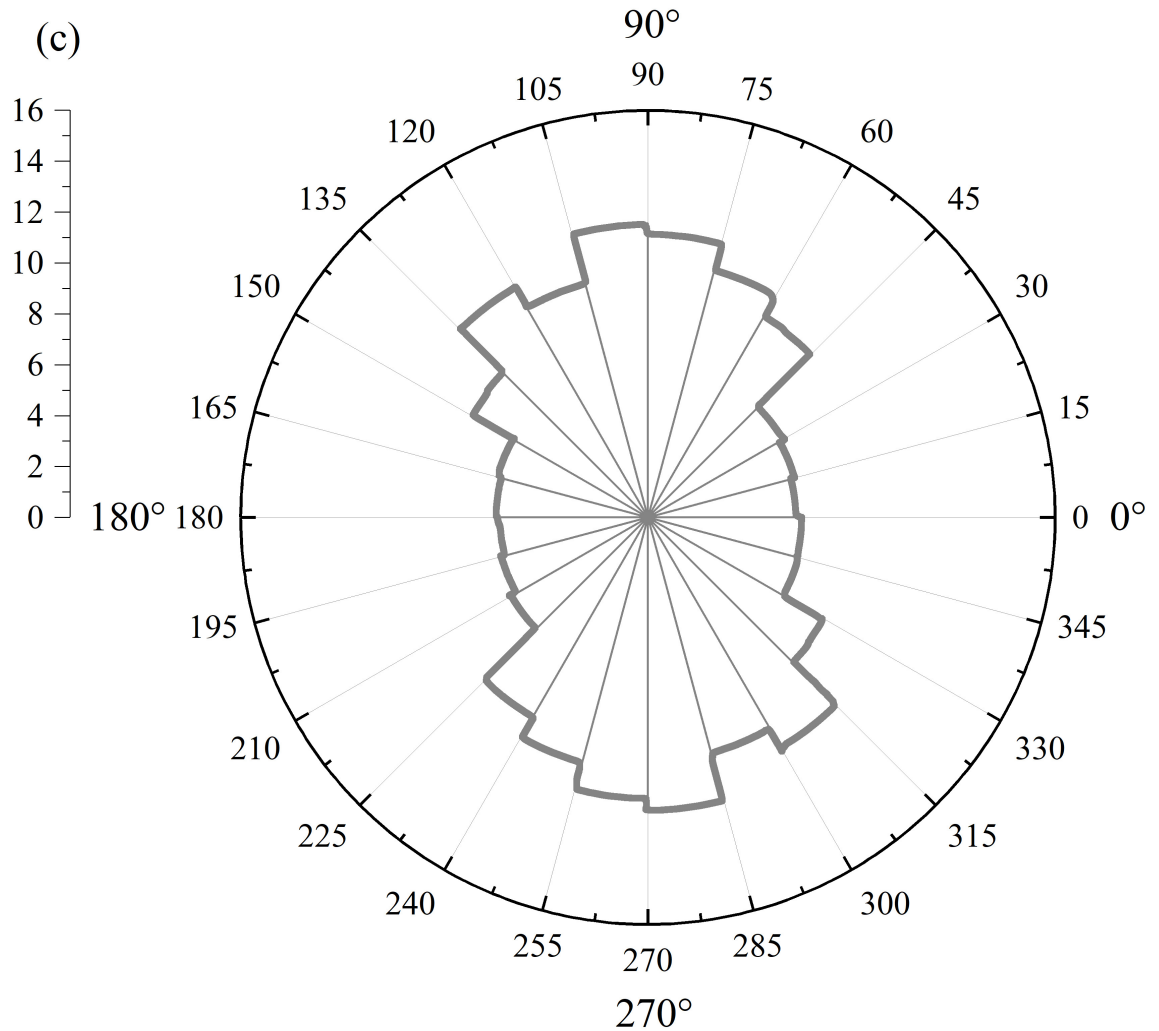
(c)
90°
90
105
75
120
60
135
45
150
30
165
15
180° 180
0
0°
195
345
210
330
225
315
240
300
255
285
270
270°
16
14
12
10
8
6
4
2
0

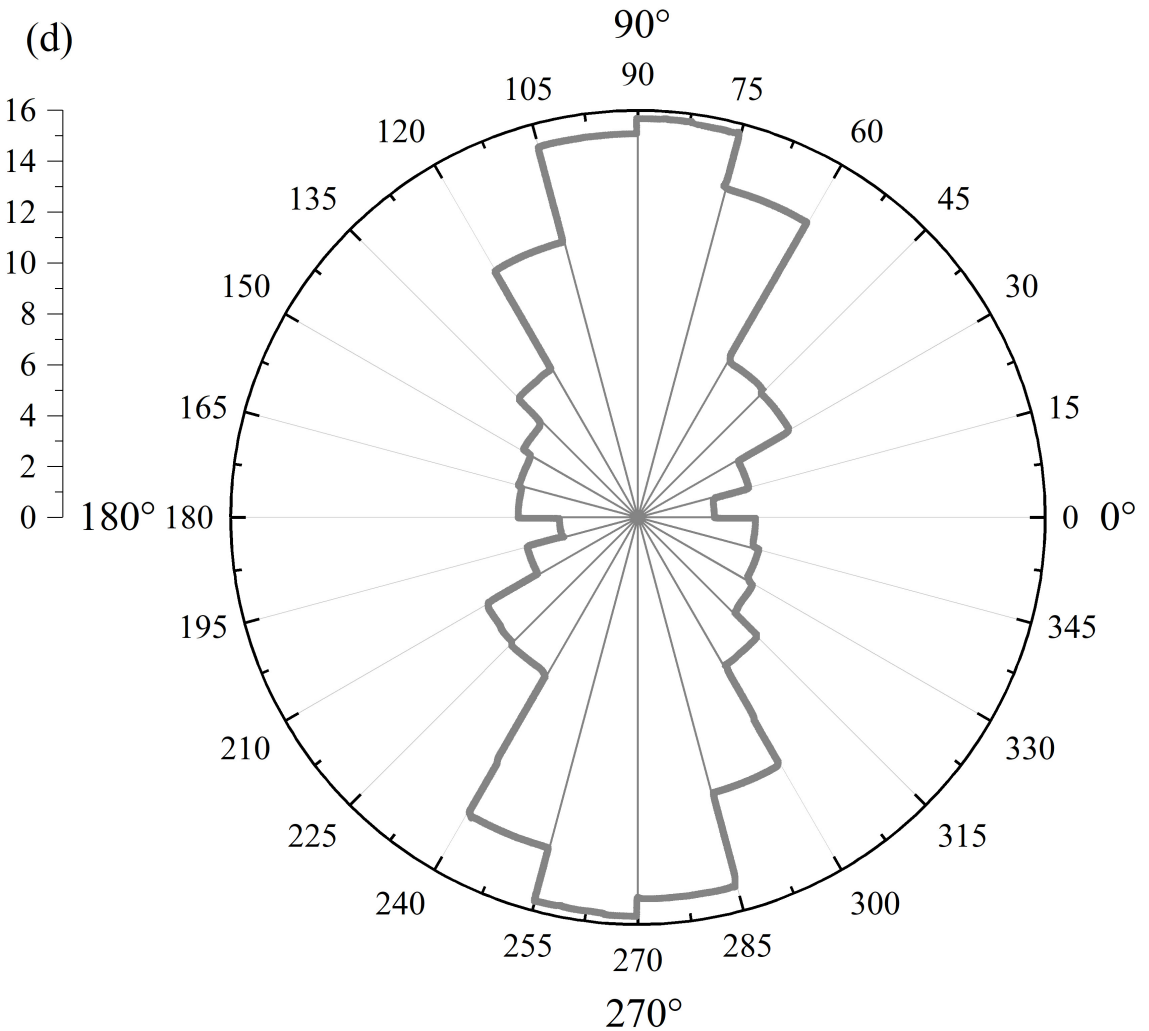
(d)
90°
90
105
75
120
60
135
45
150
30
165
15
180°
180
0
0°
195
345
210
330
225
315
240
300
255
285
270
270°
16
14
12
10
8
6
4
2
0

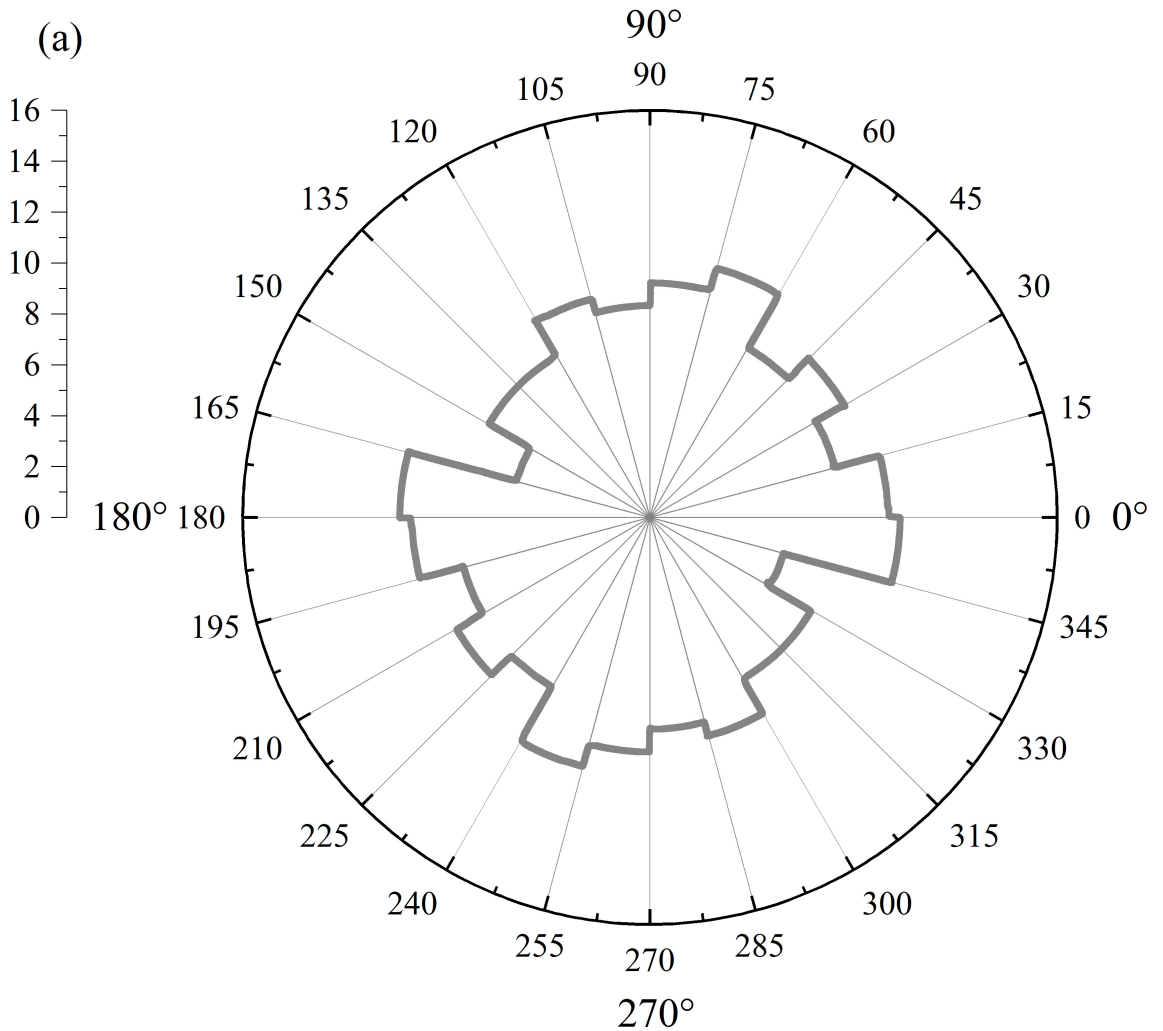
(a)
90°
90
105
75
120
60
135
45
150
30
165
15
180°
180
0
0°
195
345
210
330
225
315
240
300
255
285
270
270°
16
14
12
10
8
6
4
2
0

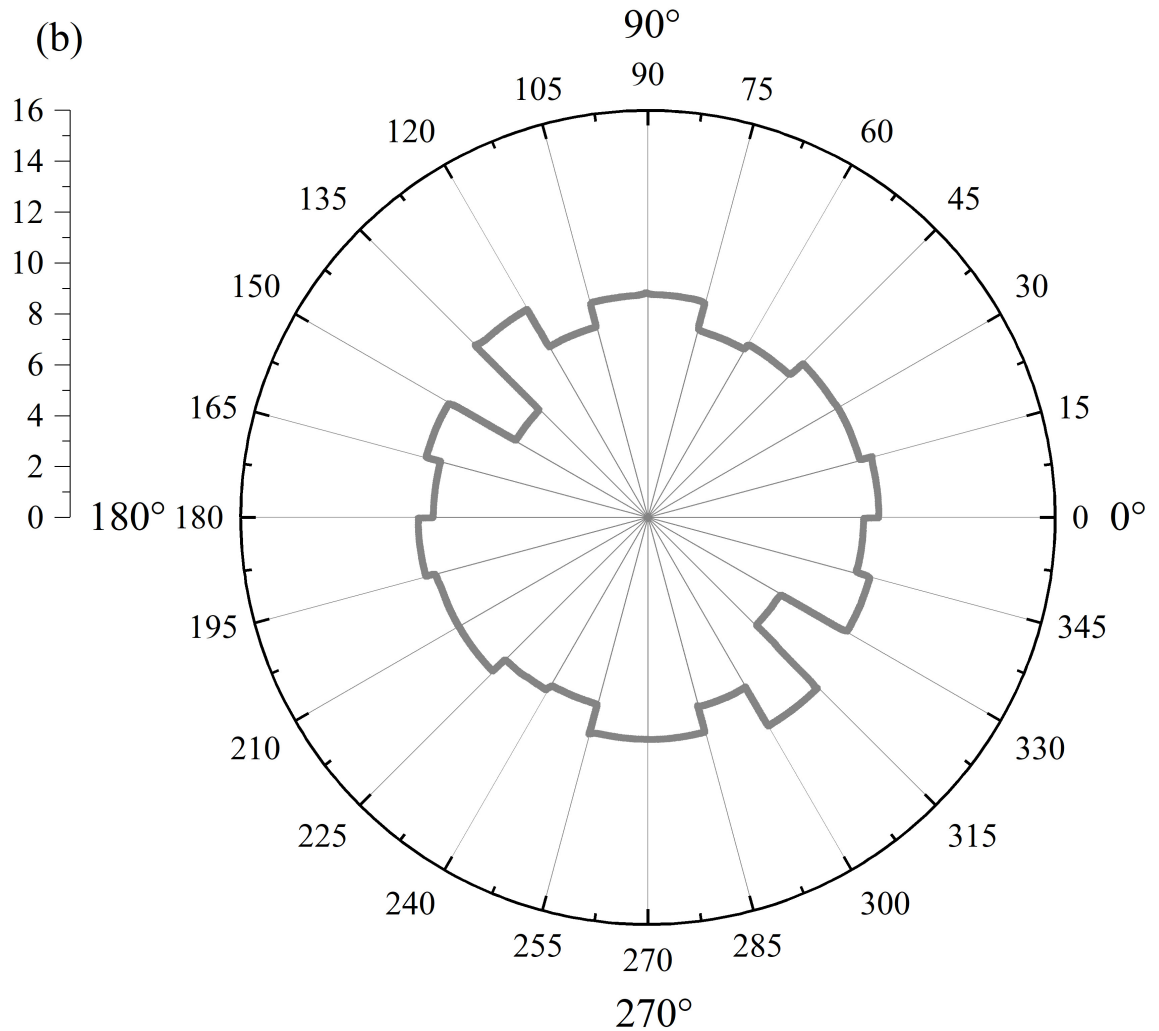
(b)
90°
90
105
75
120
60
135
45
150
30
165
15
180°
180
0
0°
195
345
210
330
225
315
240
300
255
285
270
270°
16
14
12
10
8
6
4
2
0

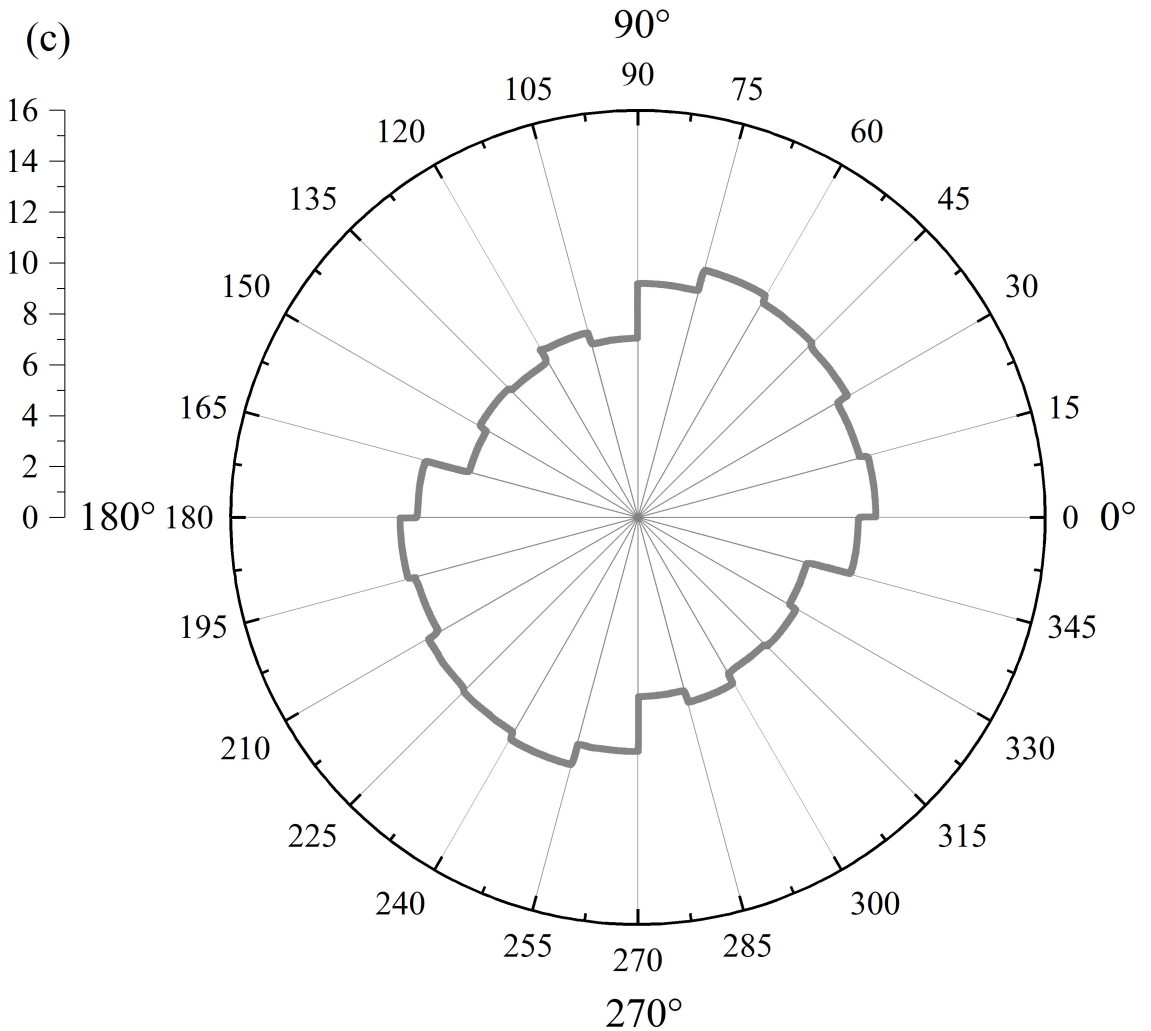
(c)
90°
90
75
60
45
30
15
0
0°
345
330
315
300
285
270
255
240
225
210
195
180
180°
165
150
135
120
105
16
14
12
10
8
6
4
2
0
270°

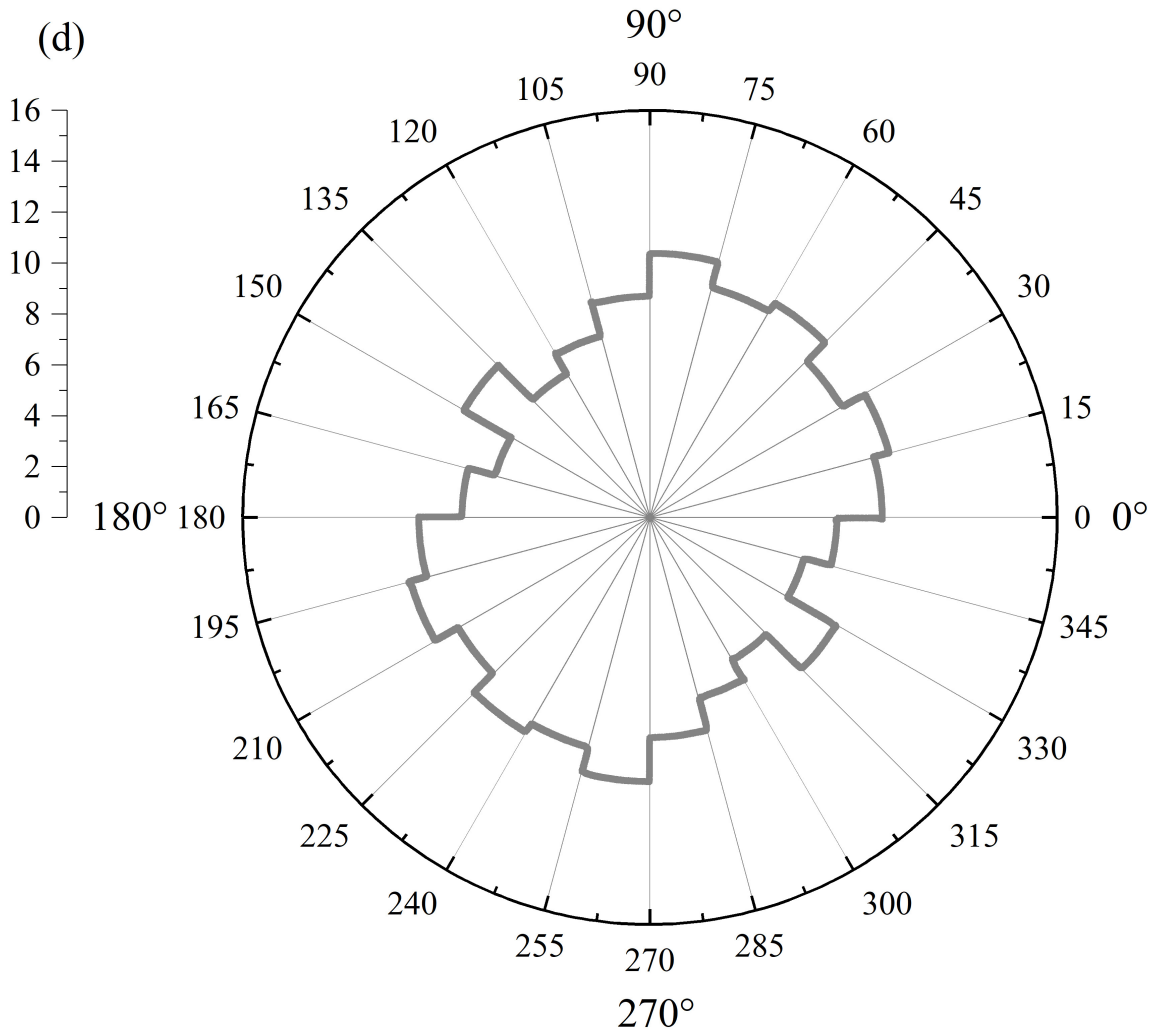
(d)
90°
90
105
75
120
60
135
45
150
30
165
15
180°
180
0
0°
195
345
210
330
225
315
240
300
255
285
270
270°
16
14
12
10
8
6
4
2
0